8-14-2020

# In-situ Cryogenic Mechanical Characterization of Materials at Micrometer Scales

Gyuho Song
*UCONN, School of Engineering, Material Science and Enigneering*, gyuho.song@uconn.edu

# In-situ Cryogenic Mechanical Characterization of Materials at Micrometer Scales

Gyuho Song, PhD

University of Connecticut, 2020

The mechanical properties of materials have been considered as one of the most important material properties for the development of mechanically reliable engineering products. Although some materials exhibit excellent material properties, such as electronic, magnetic, thermal, and optical properties, the materials cannot be usable in engineering applications if they are mechanically unstable in devices. Nowadays, nanotechnology allows us to make useful small-scale engineering devices, for instance, actuators of Micro-Electro-Mechanical-Systems and silicon-based electronic devices. These developments have continuously required the creation of mechanically reliable small materials that can survive during the long-term service. For the last two decades, micromechanical studies have revealed that mechanical properties could change significantly if a material dimension is reduced down to the micrometer-scale. At these small length scales, materials could be much stronger and tougher than their bulk counterpart. Therefore, it is critical to re-evaluate the mechanical properties of materials at the micrometer scale because small-scale mechanical properties are different from bulk-scale mechanical properties.

In this dissertation, we show our new development of state-of-the-art *in-situ* cryogenic micro-mechanical testing to investigate the mechanical properties of two different types of crystalline solids at low temperatures. First, we show how the sample dimension influences the ductile-to-brittle transition of body-centered-cubic metals. Second, we show a superelasticity of an intermetallic compound, $CaKFe_4As_4$ and its relation to superconductivity at low temperatures. We believe that these efforts provide an important insight into a fundamental understanding of the mechanical behavior of materials at the micrometer scale and at low temperatures.

# In-situ Cryogenic Mechanical Characterization of Materials at Micrometer Scales

Gyuho Song

B.S., SungKyunKwan University, **2013**

M.S., University of Connecticut, **2016**

A Dissertation

Submitted in Partial Fulfillment of the

Requirements for the Degree of

Doctor of Philosophy

at the

University of Connecticut

2020

APPROVAL PAGE

Doctor of Philosophy Dissertation

# In-situ Cryogenic Mechanical Characterization of Materials at Micrometer Scales

Presented by

Gyuho Song, B.S., M.S.

Major Advisor _____
Seok-Woo Lee, Ph.D.

Associate Advisor _____
Bryan D. Huey, Ph.D.

Associate Advisor _____
Avinash M. Dongare, Ph.D.

Associate Advisor _____
Pu-Xian Gao, Ph.D.

Associate Advisor _____
Barrett O. Wells, Ph.D.

University of Connecticut
2020

## ACKNOWLEDGEMENT

I would not be here if any one of people in this section was not there for me at the right place and at the right moment.

Prof. Seok-Woo Lee. You are the best advisor that a Ph.D. student can ask for. Your enthusiasm is contagious, the trust that I felt you gave me is mountainous, and your insightfulness is above and beyond. After Ph.D. degree, when I am on my own for the adventure of my life, your mentorship will be my compass as a scientist as well as a human.

Prof. Bryan D. Huey. In 2013, when I saw your photo and the work in a newspaper as an undergraduate in South Korea, I had no idea how everything would turn out. I found University of Connecticut thanks to you. When I was running out of money to stay in the US as a mater degree student, you were the one who kindly called me twice to offer a research position. You let me meet your inspiring student Dr. Yasemin Kutes. I will run out of a page if I list everything you have done for me. You saved my dream.

Prof. Avinash M. Dongare. In Fall 2015, I asked one of your students, Dr. Garvit Agarwal, if simulations can generate any new knowledge. I was a fool to think that simulations are of no use, thinking that it is just a trick. In Spring 2016, I was lucky enough to take your class and, with the great help of Garvit, I managed to finish the course. Then, the world that I knew became multiple-folds larger.

Prof. Pu-Xian Gao and Prof. Barrett O. Wells. If I had not had you at my Ph.D. committee members, I would have not known the details of phase diagrams of materials nor given thoughts to space groups of crystalline materials. Your helpful advice at the Ph.D. proposal and the defense was priceless.

Lorri Lafontaine. I am helpless without you. From the moment that I received an acceptance letter from UConn to this moment, I will not forget everything you have done for me and all the other students.

Dr. Roger Ristau and Dr. Lichun Zhang. I appreciate teaching how to use Focused-Ion Beam machine and helping me with Transmission Electron Microscopy at Center for Advanced Microscopy and Materials Analysis (CAMMA).

Tyler Flanagan. I have learned so much from your positive minds and unconventional way of thinking. Every question that you asked on my works got me to think again and see things differently. I was lucky to have you as a colleague. Jessica Maita. Your caring mind made me want to be a nice person. I am grateful that I have met you. Shuyang Xiao. Your brightness and hard work were so inspiring to me when I was being a lazy senior student. I have no doubt you will do great and I cannot wait to see your great work. Zhongyuan Li. I have spent only short time with you but I am glad that your polymer work will bring freshness to this lab.

UConn MSE colleagues. Dr. John Sypek. As a former lab member, I learned a lot from you. Dr. Keith Dusoe. Same thanks plus all the kind help when I was settling down in the US and understanding of my selfishness for many years. You are such a good person and I hope nothing but the best for your future. Dr. Rohit Batra and Dr. Garvit Agarwal. You are two bright stars that I found from dark sky when I was so lost in the study as well as life. I will not stop trying to be a person who deserves this companionship. Dr. Su Jeong Heo. Your thoughtfulness and caring mind are priceless and I'm in your debt. Sergey Galitskiy. I made terrible jokes and was rude to you sometimes but you were so kind all the time. I will not forget your kindness.

Lastly, my family in South Korea & the United States. My spouse, Amanda Song, I am heartless without you.

## Table of Contents

## List of Tables

## List of Figures

.

# Chapter 1. Introduction

## 1.1. Background in general

The mechanical properties of materials have been investigated to develop mechanically reliable tools. For a long time in human history, those who own stronger materials won battles and wars. In modern times, from gigantic buildings, ships, airplanes to swords, guns, small soda cans, it would have been impossible to use them if their constituent materials are not mechanically robust. Furthermore, it has been frequently seen that despite superior optical, electrical, chemical and magnetic properties, materials developed from new research cannot be usable in engineering applications due to the mechanical instability.

Nowadays, nanotechnology allows us to make useful small-scale mechanical devices, for instance, Micro-Electro-Mechanical-Systems (MEMS) sensors (**Figure 1.1(a)**) [1] and silicon-based electronic devices. In the medical field, MEMS devices are used for sensors to measure blood pressure, body temperature, glucose level, tissue tension, brain and heart electrical impulse, and oxygen/carbon dioxide level and for actuation devices for microfluidic pumping, drug delivery, filters, and separators [2]. As wearable technologies and healthcare are becoming one, it is not too distant future for the MEMS to be a part of our body [3]. In our daily lives, MEMS application is already the cores of a smartphone as well, for instance, accelerometers and gyroscopes to acoustic wave filters for an antenna, and optical image stabilizer for cameras, which are becoming one of the most important components. With the rapid advances in lithography technologies, the commercially produced silicon chips are 8 nm – 14 nm thick [4,5], which are nearly 5,000 - 8000 times thinner than a human hair (**Figure 1.1(b)**) [6].

As much as they are sophisticated, the nano-sized chips are devices can be vulnerable to damage. In other words, all these advanced technologies will stop working if those small components fail to stay on a substrate mechanically stable during manufacture and in service. Therefore, it is critical to have the capability to measure mechanical properties at a small scale and gain a fundamental understanding of them.

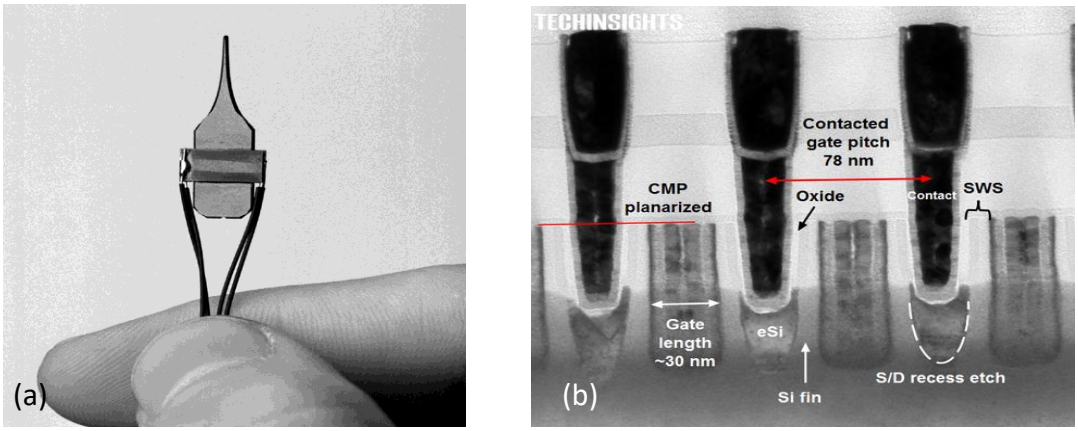


**Figure 1.1. (a) Ultrasonic phacoemulsifiaction tool** [1], **(b) TEM cross section of a typical NMOS transistor used by the Exynos 7420** [6]

## 1.2.Mechanical behavior of materials

When elastic deformation is imposed, a material can store the applied strain energy. However, when the stored energy exceeds the limiting value, the material begins to deform plastically to dissipate the excess energy as the shape change (work done) and the heat. In crystalline materials, plasticity can be carried primarily by the motion of one-dimensional crystalline defect, a dislocation. In amorphous and quasi-crystalline materials (non-crystalline, in general), a shear band carries plasticity [7,8]. Because plasticity carriers usually do not move back to their original location, their motion results in permanent translation and/or rotation of the deformed body. As

the deformation continues, a crack is eventually developed due to atomic decohesion, leading to fracture. The schematic diagram of mechanical behavior under uniaxial tension is available (**Figure 1.2.**).

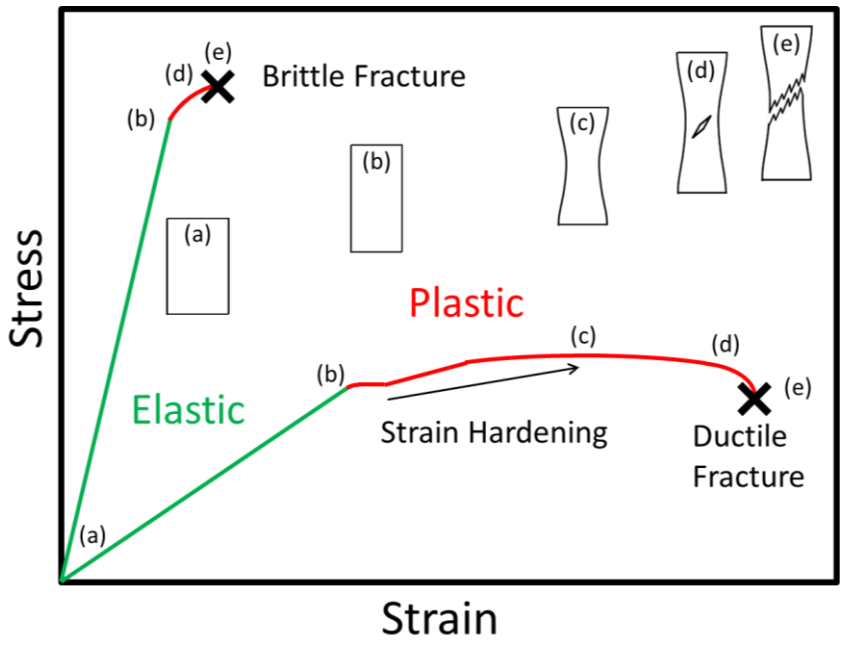


**Figure 1.2. A schematic of a general mechanical behavior of materials. (a) Stress-free state; Elastic deformation from Point (a) to (b); Plastic deformation from Point (b) to (e); Necking occurs at Point (c); Fracture occurs at Point (e).**

Firstly, the motion of a dislocation occurs via the propagation of a systematic change in atomic arrangement at a dislocation core, causing plastic flow within a crystal structure (**Figure 1.3.**) [9]. The stress-level at which a dislocation starts to move is termed a yield strength. If the atomic bonding is strong (e.g. ionic or covalent bonding) or the dislocation core structure is complex, the motion of dislocations is usually difficult because the atomic re-arrangement at a dislocation core becomes much more difficult. In this case, the mobility of dislocation is usually low, and a material is strong, but brittle. If the atomic bonding is easy to break (e.g. metallic

bonding) and a core structure can be modified easily, the mobility of dislocation is high. Dislocation mobility is temperature-dependent because thermal vibration affects the atomic rearrangement at a dislocation core [10,11]. Dislocation mobility usually becomes higher as the temperature increases, so a material becomes more malleable at a higher temperature.

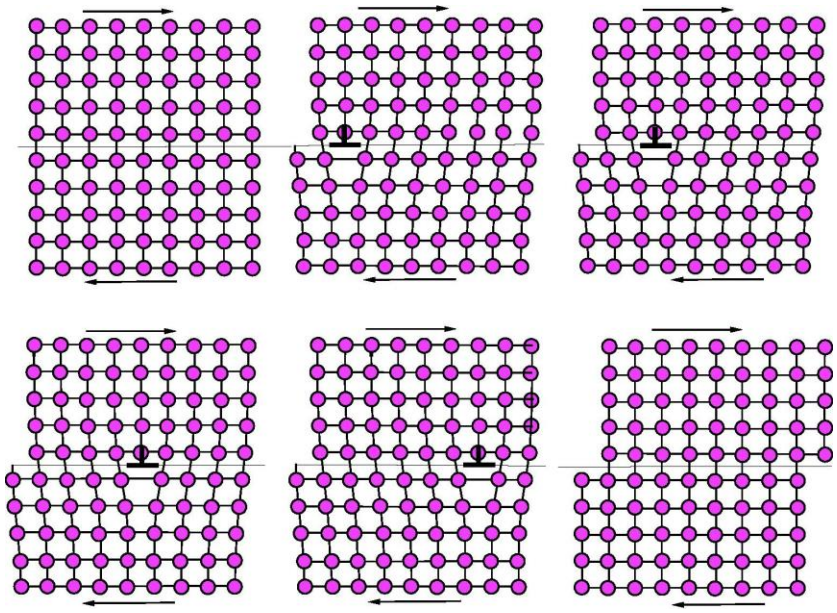

**Figure 1.3. Propagation of edge dislocation in simple cubic structure** [9]

For Face-Centered-Cubic (FCC) metals, the dislocation slip system consists of the closed-packed plane and the shortest translation direction, which correspond to {111}<110> slip systems. The perfect dislocation with ½ <110> Burgers vector tends to dissociate into two (Shockley) partial dislocations with 1/6<112> Burgers vector and spread out on {111} plane (**Figure 1.4(a)**). The area between two partial dislocations is called a stacking fault, and the width of stacking fault depends on its stacking fault energy. Due to its planar core structure and relatively weak metallic bonding, a dislocation in FCC can move easily regardless of edge/screw character. In Body-Centered-Cubic (BCC) metals, however, a dislocation has ½ <111> Burgers vector, and the core structure of a screw dislocation spreads out to multiple <111> planes

(**Figure 1.4(b)**) [12]. This complex non-planar core structure usually limits the mobility of screw dislocations. The low mobility of dislocations in BCC metals explain their high lattice resistance and the consequent brittleness, compared to FCC metals. Due to the high lattice resistance, a screw dislocation in BCC crystals moves by nucleating and migrating kink-pairs at non-zero temperature [13]. This kink-pair mechanism is thermally and/or stress- assisted and remains active until a certain temperature, at which lattice resistance become negligibly low. The difference between the edge and screw dislocation mobility in BCC metals has been investigated extensively [14]. For instance, an edge dislocation is reported to be 40 times faster than a screw dislocation in pure Molybdenum at room temperature [15]. This large mobility difference is temperature-dependent and disappears when a temperature reaches a critical temperatures, at the mobility of screw dislocation becomes the same with that of edge dislocation [14].

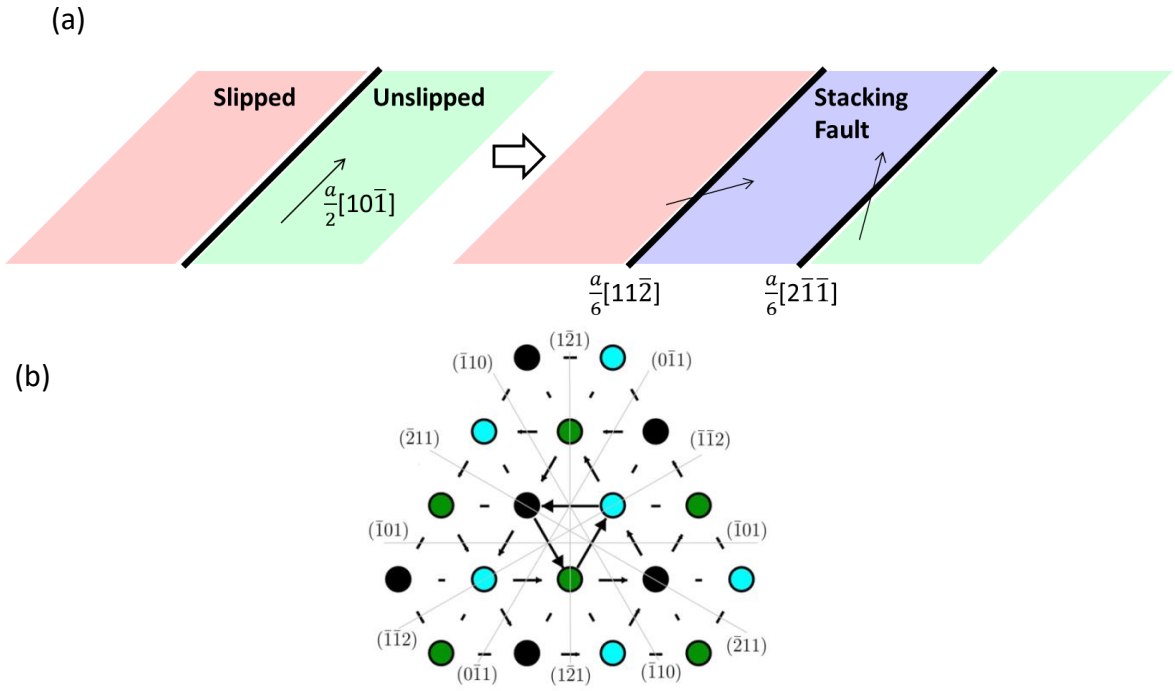


**Figure 1.4. (a) Partial dislocations bounded by stacking fault in FCC crystals, (b) Complex core structure of screw dislocation in BCC crystals** [12]

Secondly, at bulk scale, a dislocation is capably of self-multiplication from a dislocation source. Frank-Read source is the example of dislocation source. Frank-Read source is a double pinned mobile dislocation (**Figure 1.5.**) As the dislocation segment bows out under high enough stress, the circumference becomes larger until it becomes a closed loop. Once it is closed, a new dislocation forms at the center region, and a dislocation loop expands and move away. This Frank-Read source mechanism can generate many dislocations rapidly via the repeated operation, leading to strain hardening [16].

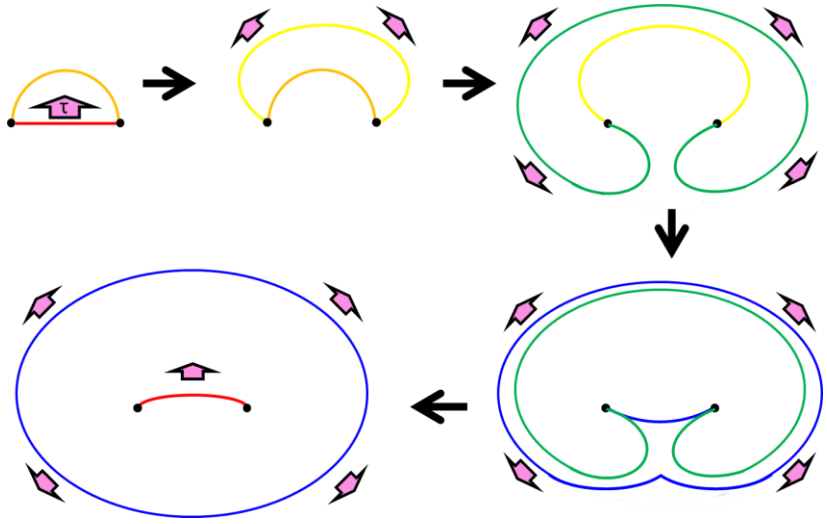

**Figure 1.5. Dislocation multiplication process of Frank-Read source.**

Third, dislocation nucleation occurs when a material is lack of dislocation. Homogeneous nucleation of a dislocation occurs when high applied stress can rupture a line of atomic bonds at the inside of crystalline materials, resulting in a shear displacement by one Burgers vector (**Figure 1.6(a)**) [17]. This process requires the simultaneous atomic displacement, so the required stress is closed to the theoretical strength of materials [16]. This extreme phenomenon usually occurs when a material was deformed by shock compression [18]. Also, spherical

nanoindentation can induce the homogeneous dislocation nucleation because the maximum shear stress is developed at the inside of material [19,20]. Heterogeneous dislocation nucleation can occur much more easily because it requires only about the half amount of energy compared to the homogeneous dislocation nucleation (**Figure 1.6(b)**) [17]. It occurs at the surface, grain boundaries, crack tips, etc., which can work as stress concentrators in the material. Dislocation nucleation at a crack tip is the critical factor to determine whether brittle fracture occurs or not. The sufficient amount of dislocation nucleation at a crack tip can suppress brittle fracture. Dislocation behaviors can be affected by other factors, such as temperature, stress, the distribution of interstitial/substitutional atoms and precipitates [21]. Thus, the control of dislocation behaviors is an important engineering problem.

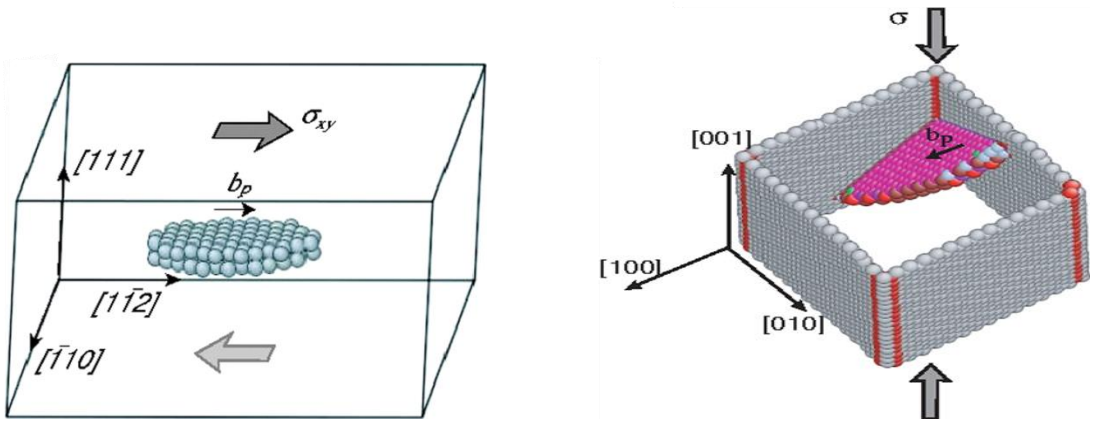


**Figure 1.6. (a) Homogeneous dislocation nucleation and (b) Heterogeneous dislocation nucleation in molecular dynamics simulation** [17]

## 1.3.Ductile-to-Brittle Transition

Liberty ship failure at World War II, which is one of the most famous incidents in materials research history, shows how dramatically the mechanical properties of materials can change at low temperature (**Figure 1.7(a)**) [22]. Subsequent investigations showed that this incident occurred by Ductile-to-Brittle Transition (DBT). Many ships were made of steel, which was thought to be a strong-and-ductile BCC metal. A screw dislocation in BCC crystals moves by nucleating and migrating kink-pairs at a finite temperature [13]. As the temperature decreases, the kink-pair mechanism is thermally-suppressed, leading to the decrease in mobility of screw dislocation. Once the temperature decreases below a certain critical temperature, screw dislocations cannot move and cannot generate the plasticity. In addition, a dislocation nucleation is the thermally-activated process and is suppressed at a low temperature. Therefore, a dislocation cannot be nucleated at any stress concentrated region such as a crack tip. The low mobility of dislocation and the suppression of dislocation nucleation at a crack tip lead to the catastrophic brittle failure of material. Materials that go through this transition show the rapid drop in impact energy as temperature decreases. (**Figure 1.7(b)**) This phenomenon was termed DBT. Combined with other factors such as a square corner of hatch working as a stress concentrator and largely welded steel sheets letting cracks propagate for large distances, those gigantic ships were catastrophically split into half.

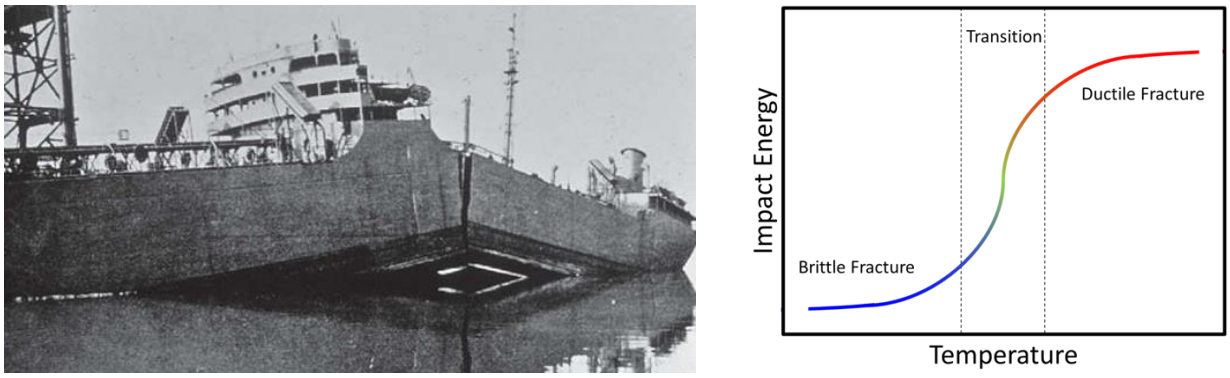


(a) (b)

**Figure 1.7. (a) Fractured Liberty ship failure at World War II due to DBT** [22], **(b) A change of impact energy of a material with DBT in terms of temperature**

Extensive studies have been done to understand what makes materials ductile or brittle and two major theories stood out. Rice and Thomson proposed a model that dislocation nucleation at a crack tip determines whether DBT occurs or not (**Figure 1.8(a)**) [23]. Due to the high stress concentration at the crack tip, it is possible to nucleate a dislocation embryo. If dislocation nucleation can occur at lower stress than that of crack propagation, the plastic deformation can effectively suppress a brittle fracture (catastrophic failure). Stroh proposed a different model which is related to the presence of impurities or precipitates (**Figure 1.8(b)**) [24]. Impurity atoms or precipitate can lock the operation of Frank-Read source, leading to brittle fracture. Thermal fluctuation at high temperature enables the Frank-Read source to overcome this resistance, leading to ductile deformation. Hirsch proposed that the dislocation mobility controls DBT (**Figure 1.8(c)**) [25]. By cross-slipping, existing dislocations can be attracted to the crack tip and work to shield the crack as well as generate dislocation loops (sources).

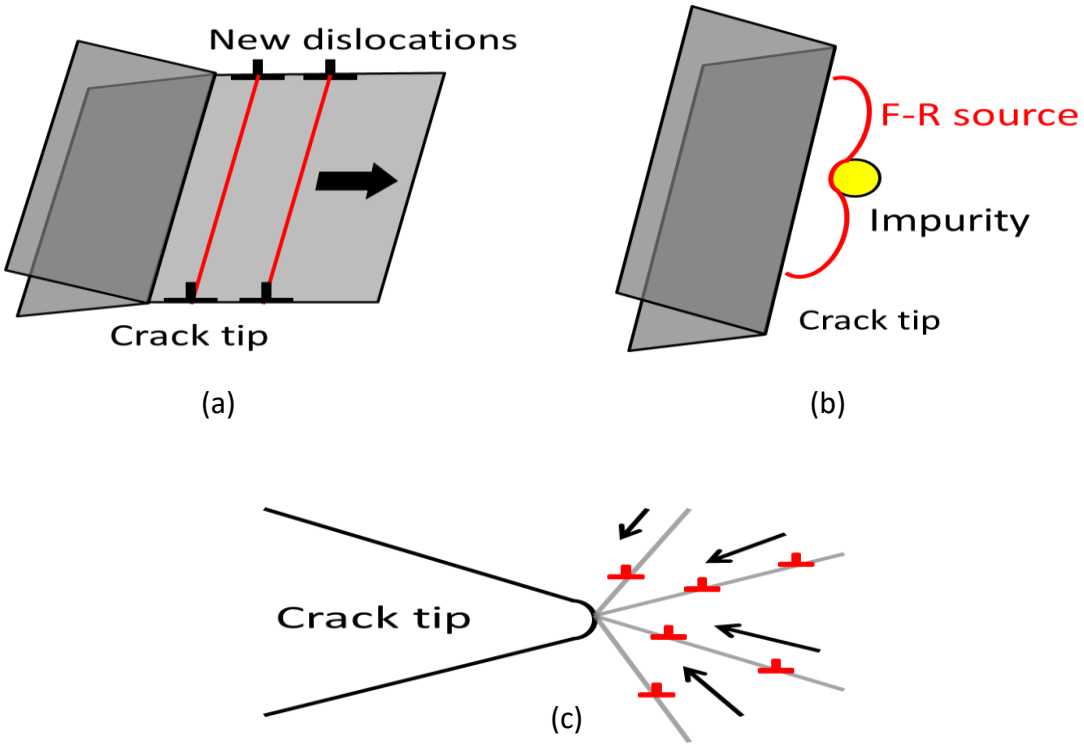


**Figure 1.8. (a) Rice-Thompson model – emission of dislocation at a crack tip, (b) Stroh model – the dislocation locking at impurities, (c) Hirsh model – interaction between a crack and pre-existing dislocations**

Both dislocation nucleation and mobility play key roles in DBT. Computational materials researches began to show atomistic point of views and propose different ideas, such as the change of slip system [26]. Thus, in terms of engineering and designing, it will be important to consider all the models and think which one will outweigh the others under the condition of interest.

## 1.4.Mechanical behavior of $ThCr_2Si_2$-type intermetallic compounds

It has been 35 years since Hoffmann and Zheng proposed the noble idea of bond making/breaking structural transition with a number of $ThCr_2Si_2$-type structured intermetallic

compounds (**Figure 1.9(a)**) [27]. Recently, this structure has received a lot of attention due to the property tenability and the possibility of its high-temperature superconductivity [28]. FeAs-based pnictides show the first-order phase transition under hydrostatic pressure by making As-As type bond as well as collapsing the magnetic moment of Fe atoms, leading to the significant change in magnetic and electronic properties as well as to the lattice collapse along c-axis, for instance, over 10% c-axis reduction in single crystalline $CaFe_2As_2$ [29]. This lattice collapse along c-axis can be recovered when an applied pressure is relaxed. Thus, the elastic deformation of $CaFe_2As_2$ was investigated under uni-axial compression.

Sypek, et al. performed uni-axial micropillar compression tests with a single crystalline $CaFe_2As_2$ along c-axis. They reported high strength, ~3.7 GPa and superelasticity, ~13.7% remarkable recoverable strain (**Figure 1.9(b)**) [29]. Density Functional Theory (DFT) calculation confirms the formation of As-As bonds under compression (**Figure 1.9(c)**). Due to its high strength and strain, the work absorption/release capacity is an order of magnitude higher than most of advanced engineering materials [30,31]. As a structural material, the giant c-axis lattice collapse without fracture is surprising especially for an intermetallic compound because it usually fails catastrophically within the limited strain range (less than 1%) due to their extreme brittleness [31]. Furthermore, this ultra-high recoverability through a structural transition would enable FeAs-based pnictides to be strain-engineerable. For example, it is possible that superconductivity of FeAs-based pnictides could be switched on and off by mechanical loading.

In addition, by using DFT calculation and neutron scattering measurement with in-situ cryogenic hydrostatic pressure, Sypek, et al. investigated the metastability of a single crystalline $CaFe_2As_2$ in the form of collapsed tetragonal at 50 K [29]. The structure was deformed and unloaded at 50 K. The structure remained deformed. Then, the structure was heated above 100 K

and restored the shape back to the original structure. This result showed a new shape memory effect and made $CaFe_2As_2$ a possibility to develop an actuator that can work in cryogenic condition such as deep space exploration.

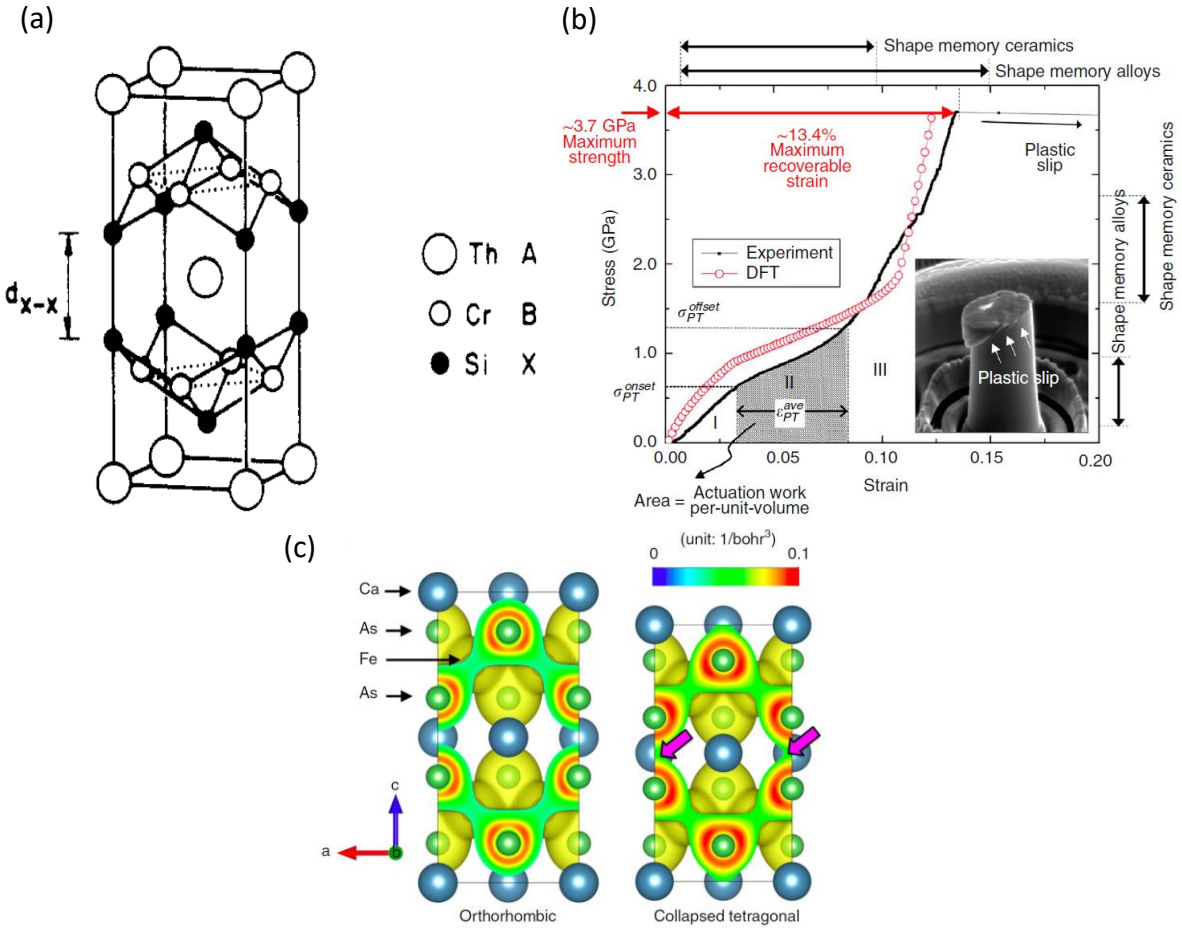


**Figure 1.9. (a) ThCr2Si2-type structure** [27]**, (b) The stress-strain curve of CaFe2As2, (c) Density Functional Theory calculation showing As-As bond formation under a-axis loading** [29]

## 1.5.Mechanical behavior of materials at the micrometer scale

Making systems smaller requires more than just shrinking the size. For the last two decades, micromechanical studies have revealed that mechanical properties could change significantly if a

material dimension is reduced down to the micrometer-scale. At small length scales, materials can be much stronger and tougher than their bulk counterpart. Therefore, it is critical to re-evaluate mechanical properties of materials at the micrometer scale because they are different from bulk properties.

*Smaller is Stronger*

In most metals, pre-existing dislocations move and interact to each other when a stress becomes higher than their yield strengths. When they are pinned by other dislocations, dislocations often multiply. In bulk metals, mobile dislocations almost always exist, and their collective motion causes plastic yielding. With the similar dislocation density, however, when the material dimension decreases down to the micrometer-scale, only a few dislocation sources remain, and plasticity is controlled by the operation of individual dislocation sources. This plasticity mechanism at the micrometer scale is called source-controlled plasticity [32]. The plasticity process can be explained by the weakest link concept [33]. Simply speaking, when the sample dimension decreases, the chance of having a weak dislocation source decreases. Therefore, smaller materials can be stronger because the plastic deformation occurs by the operation of stronger dislocation source.

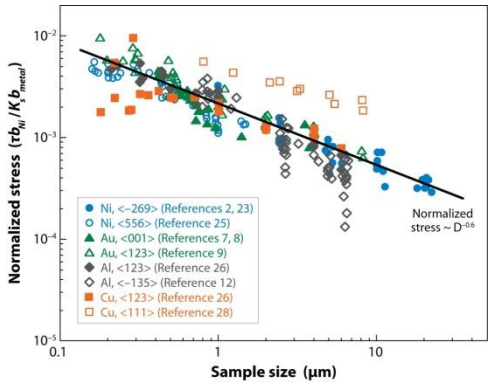


(a)

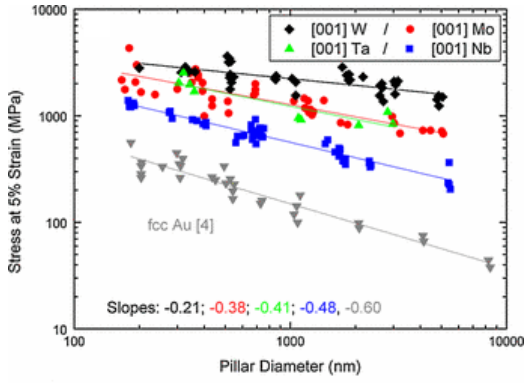


(b)

**Figure 1.10. The size dependence of (a) FCC metals** [34]**, (b) BCC metals** [14]

Single crystalline metals showed that the size effect on the flow stress obeys a power-law relation. The power-law can be described by $\sigma = Ad^{-n}$, where A is the proportional constant, d is a sample diameter, and n is the power-law exponent. The power-law exponent of single crystalline metals was reported to be 0.6–1.0 for FCC crystals and 0.22–0.45 for BCC crystals (**Figure 1.10(a) and (b)**) [14,34]**.** The difference of the size dependence between FCC and BCC crystals is attributed to the intrinsic lattice resistance of dislocation. The intrinsic lattice resistance is the critical shear stress required to move an infinitely long straight dislocation. If we adopt a single arm source model, the size effect can be understood as follows.

$$\tau_{CRSS} = \tau_0 + 0.5\, K_s\, b \sqrt{\rho_{tot}} + \frac{K_s\, b}{\bar{\lambda}_{max}(D, \rho_{tot}, \beta\ )} \qquad \text{(Equation 1.1)}$$

$\tau_{CRSS}$: the CRSS for the activation of the weakest single arm dislocation source
$\tau_0$: the intrinsic lattice resistance
$K_s$: the anisotropic shear modulus
b: the magnitude of Burgers vector
$\bar{\lambda}_{max}$: the statistical average length of the weakest single arm dislocation source
D: a micropillar diameter
$\rho_{tot}$: the total dislocation density
$\beta$ : slip plane orientation

In Equation 1, the critical resolved shear stress (CRSS) of single arm source model is constituted of intrinsic lattice resistance, dislocation interaction, and source truncation, in order [35]. For the simplicity, two steps can be taken. First, by assuming the similar dislocation density ($\rho_{tot} = \rho^*_{tot}$) and slip plane orientation ( $\beta = \beta^*$) for FCC and BCC, the $\bar{\lambda}_{max}$ can be only a function of a micropillar diameter ($\bar{\lambda}_{max}(D, \rho^*_{tot}, \beta^*) = \bar{\lambda}_{max}(D)$). Secondly, by fixing the dislocation density to be the same typical moderate number for FCC and BCC, the intrinsic

lattice resistance and dislocation interaction can be represented by $\tau_{bulk}$. Then the Equation 1 can be simplified as follows.

$$\tau_{CRSS} = \tau_{bulk} + \frac{Ks\ b}{\bar{\lambda}_{max}(D)} \approx B\ D^{-n} \quad \text{(Equation 1.2)}$$

$\tau_{bulk}$: the shear stress at a bulk scale
B: proportional constant

Because the intrinsic lattice resistance ($\tau_0$) of BCC metals is usually an order of magnitude higher than that of FCC metals and the dislocation interaction term is not significant for both BCC and FCC when the dislocation density is moderate, BCC metals will have a much larger $\tau_{bulk}$ than FCC. Thus, the influence of the source truncation term on the critical resolved shear stress ($\tau_{CRSS}$) is smaller in BCC metals and will have smaller power-law exponent, n.

The size effect at the micrometer scale also exists outside the crystalline materials with dislocations. For instance, $YCd_6$ quasi-crystal (QC) and its approximant also showed 'smaller is stronger' without translational symmetry [36]**.** The power-law exponent of QC approximant was found to be 0.4. Wang, et al. calculated the theoretical a power-law relation of materials with shear band deformation to be 0.5 [37]. The model is the balance between the elastic energy stored in the micropillar and the energy increase by creating shear bands. The calculation gives the power-law exponent, 0.5, and the small deviation can be understood by the heat dissipation or elastic recovery. In Bulk Metallic Glass (BMG), Zr-based BMG nanopillars of 100 nm in diameter, which has an amorphous atomic arrangement, exhibits even higher strength from 1.7 GPa in bulk to 2.25 GPa [38].

*Smaller is Weaker*

It can also mean being weaker. At deep sub-micrometer regime (less than 100 nm), the large surface to volume ratio begins to influence the plasticity mechanisms, such as surface dislocation nucleation and diffusion through free surface.

Firstly, when the sample size is small, dislocations can easily escape to the free surface, leading to dislocation starvation. To accommodate the strain further, dislocations needs to be nucleated and the free surface works as a heterogeneous nucleation site. Thus, larger surface to volume ratio makes surface nucleation easier and decrease the nucleation stress (**Figure 1.11(a)**) [39,40].

Secondly, diffusive plasticity can be considered. The grain boundary diffusivity is usually orders of magnitude larger than that of bulk diffusivity [41,42]. For free surfaces, it is even larger due to less constraint. Thus, at the extremely small scales, surface diffusion can take a significant portion in the entire plasticity. For example, a single crystalline Ag can show diffusive plasticity at 10 nm or smaller at room temperature (RT). Because the diffusivity is temperature dependent, the size can be much larger at higher temperature (closer to its melting temperature 1234K) [43]**.** Likewise, a single crystalline Sn was reported to diffusively deform at RT with the sample size, 130 nm, because its homologous temperature at RT is already 0.6 (**Figure 1.11(b)**) [44].

'Smaller is weaker' is also found in polycrystalline nanopillars. In polycrystalline materials, the hardness is dependent on the grain size. As the grain size decreases, the hardness goes up because grain boundaries impede dislocation motion. It is called Hall-Petch (H-P) relation. However, when the grain size is extremely small, the hardness starts to decrease together with grain size because the nano-sized grain boundary sliding can slide against each other [45]. It is

called inverse H-P relations and the grain size is around 10 nm [44]. When the size of nanocrystalline nanopillars is less than 100 nm, the fraction of grains at the surface becomes high enough to control the pillar strength. With 12 nm grain-sized Pt nanopillars, surface grains start to slide rather than nucleating dislocations when the pillar diameter is lower than 60 nm and it becomes weaker as the pillar size decreases [46].

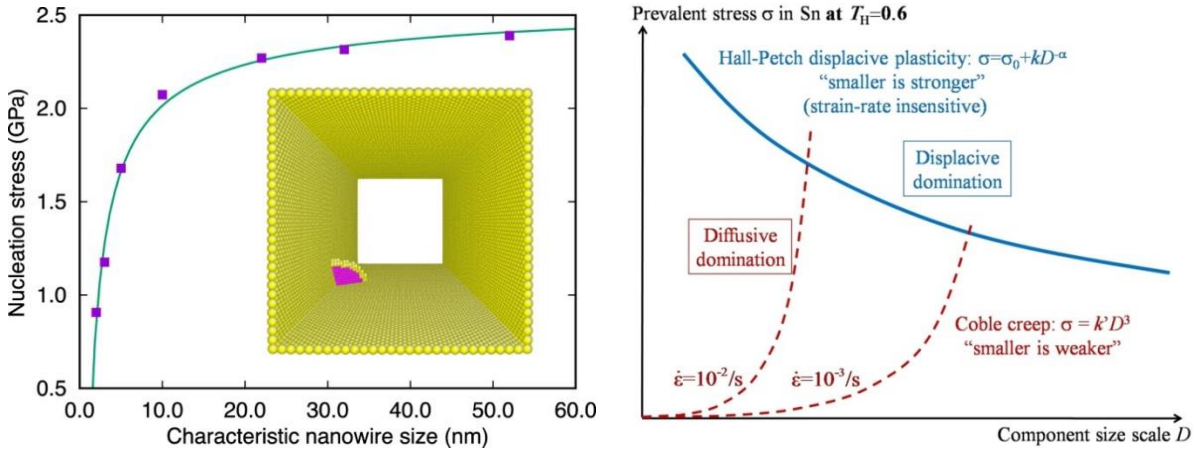


(a) (b)

**Figure 1.11. (a) 'Smaller is weaker' for surface dislocation nucleation stress in [100]-oriented square copper nanowire under compression at 300 K. Data points are calculated values and the solid curve is non-linear fitting. The inset shows a typical saddle configuration of a dislocation loop nucleating from the lower-left corner of the square nanowire.** [39]**, (b) Change of deformation mechanism in Sn according to the size (displacive plasticity and diffusive plasticity)** [44]

*Smaller is Tougher*

Fracture is sensitive to the geometry and distribution of defects, such as surface flaws or micro-cracks. Plastic deformation in brittle materials is often observed by stress concentration followed by catastrophic fracture. If the dimension of materials becomes close, especially, to the nano-meter length scale, the defects can be effectively removed, and they would possess nearly no defect. Then, it is possible to observe the ductility of these otherwise brittle materials. For example, Gallium Arsenide (GaAs) micropillars with 1 μm in diameter display significant dislocation-based plasticity [47]. Silicon nanopillars with diameters less than 300 nm exhibit extensive plastic slip events instead of brittle fracture under uni-axial compression [48]**.** The fracture toughness of silicon spheres and pillars was reported to increase with an inverse square-root size dependence (**Figure 1.12**) [49]**.** For metallic glasses, it is reported that large-sized BMG samples fail catastrophically by unstoppable shear band propagation while, at small scales, shear bands can propagate stably, allowing extensive plasticity and the fracture surfaces are smooth [50]**.** Zr-based bulk metallic glass (BMG) nanopillars with 100 nm in diameter exhibit large ductility up to 25 % true strain [38]. It is notable because being ductile is generally inversely coupled with being stronger but this study showed they can increase together. Even, icosahedral Al-Pd-Mn QC nanopillars also exhibit the brittle-to-ductile transition at the diameter between 350 and 510 nm despite the absence of translational symmetry in its quasi-crystalline structure [51]. All these results confirm that size reduction is indeed able to prevent catastrophic failure and can promote plastic deformation.

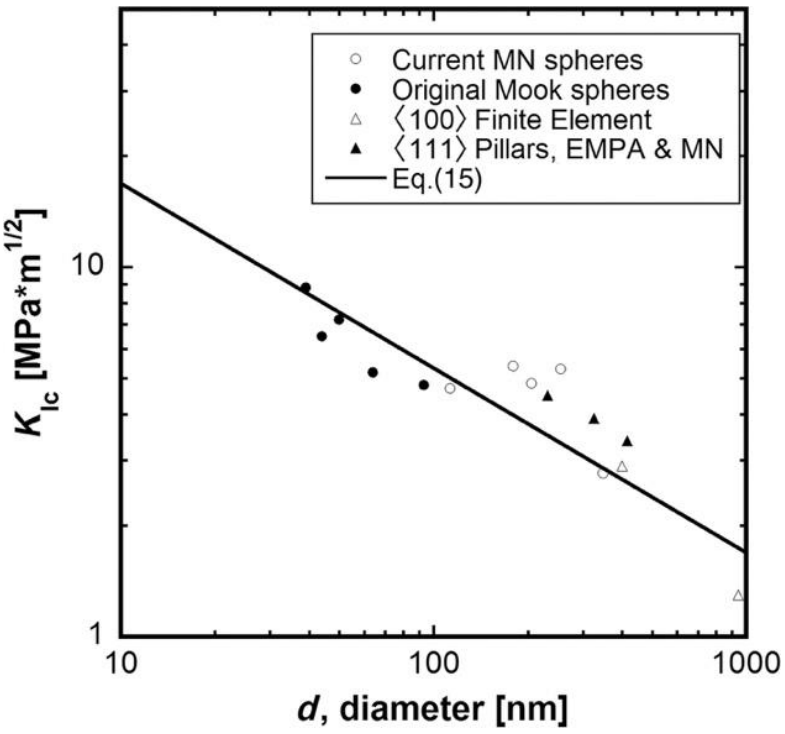


**Figure 1.12. 'Smaller is tougher' for fracture toughness of silicon spheres and pillars** [49]

*Necessity of cryogenic nanomechanical testing*

To sum up, the human civilization is advancing its quality with the help of nanotechnologies and nano-sized materials show different behaviors (e.g. stronger, weaker, and tougher) from when it is bulk-sized. Furthermore, the exploration to the outer space is being more accelerated recently and the material also behaves differently at those conditions. Thus, the importance of understanding small materials in extreme conditions will only keep growing and it will be useful to study the effect of cryogenic temperature on various materials at small scale. Thanks to advanced electron microscopy and focused-ion beam (FIB) technique, micron-sized samples can be fabricated for research with high precision. Plus, powerful computation such as Density Functional Theory (DFT) and Molecular/Dislocation Dynamics (MD/DD) has been developed to provide theoretical insight. Therefore, I conducted both experimental and theoretical studies that

uncover new mechanisms that govern the elasticity and plasticity of crystalline materials at low temperature at the micron-scale.

## 1.6. Experiments

Focused-ion beam milling

Micro-pilllars/-dog bone samples were fabricated using focused-ion beam (FIB) milling (**Figure 1.13(a) and (b)**). Three FIB equipment (Thermo Fisher, USA) were used in this study: Helios PFIB Dual Beam for high volume milling (Xe ion) and Helios Nanolab 460F1, Strata 400S Dual Beam for high precision milling (Ga ion). Xe ion beam milling was used to make the first rough cuts quickly. Later, the samples were moved to Ga ion beam milling to make precise cuts. Gallium ion beam currents from 300 to 10 pA under an operating voltage of 30 kV were used from the initial to final thinning with concentric circle patterns. Because the typical thickness of FIB damage layer is about 20 nm, which is much thinner than our pillar diameter (~2 μm), we expect negligible effects of FIB damage on the mechanical data. The tapering was controlled below $2^{o}$. To avoid unnecessary trench around the pillar and measure the precise strain, several square pillars were also made by using side-milling. The ideal height to diameter ratio for micropillars is 3:1 to avoid buckling issue under compression. The micron-sized samples were made on the (001) surface of the single crystalline specimens, unless it is mentioned otherwise.

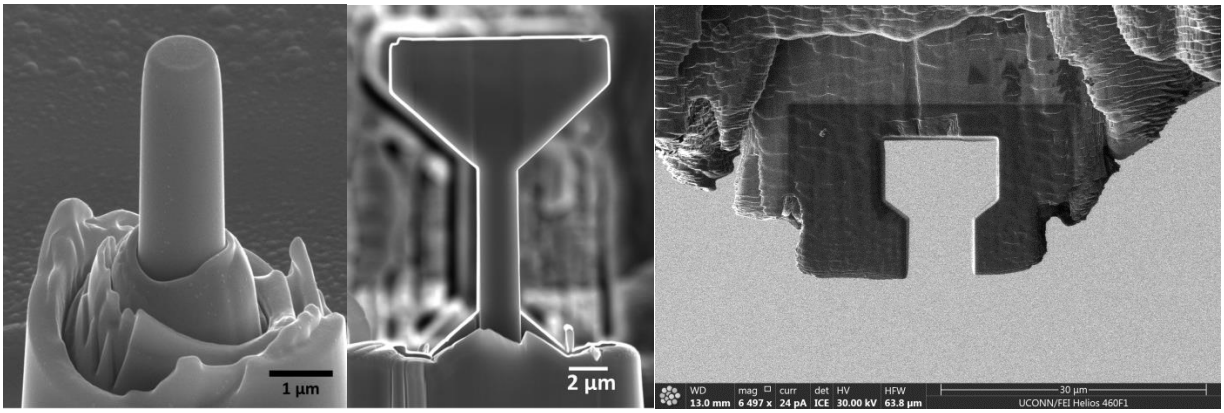


(a) (b) (c)

**Figure 1.13. (a) Micro-pillar for compression tests, (b) micro-dog bone sample for tension tests, (c) micro-tensile test grip made from diamond flat punch tip**

Of course, there are concerns about preparing sample at small scales. Focused ion-beam milling, in particular, has been under debate. Depending on materials` atomic weight, bonding characteristics, beam energy and etc, the depth of ion damage on the surface varies**.** Groups studied the strengthening on the surface by ion beams (Ga or He) with nanoindentation hardness testing and reported significantly increased hardness with various indentor sizes ranging from 1 to 100 micrometer [52,53]. On the other hand, other group made submicron-sized samples in various ways including annealing, second milling with low-energy $Ar^+$ and growing via electrodeposition followed by annealing. It was concluded that they all showed strong size effect despite the difference in fabrication methods and the damage was negligible [54]**.**

Uni-axial compression and tension micro-mechanical testing

*In-situ* micro-mechanical test was performed at room temperature and under an high vacuum condition ($<10^{-4}$ Pa) using a NanoFlip$^{TM}$ (KLA-Tencor, USA), which is installed in a field-emission gun JEOL 6335F scanning electron microscope (JEOL, Japan). A nominal

displacement rate of 10 nm/s, which corresponds to the engineering strain rate of ~0.002 $s^{-1}$, was used for all *in-situ* compression/tension tests. Strain calculations for compression experiments were done with the Sneddon punch correction using the effective Elastic modulus that was measured by nanoindenter, iNano™ (KLA-Tencor, USA). The recorded video was often used to visually confirm that our strain measurements were accurate. The tip used for compression was a conductive diamond Pyramid flat punch (Micro Star Technologies Inc, USA) and the same tip was cut by FIB to make dog bone sample grip for tension (**Figure 1.13(c)**).

Nanoindentation

Nanoindentation is a depth and load sensing testing at nano-/micron-scale. The tests were performed *ex-situ* by iNano™ (KLA-Tencor, USA). Unlike uni-axial testing, the stress applied to the material is 3-dimentional and more complex and it was under ambient atmosphere. The choice of tip is wider, from a sharp Berkovich tip to spherical tip with various diameters. It is mainly used to roughly measure hardness as well as Elastic modulus of materials at small-scale.

Cryogenic temperature set-up

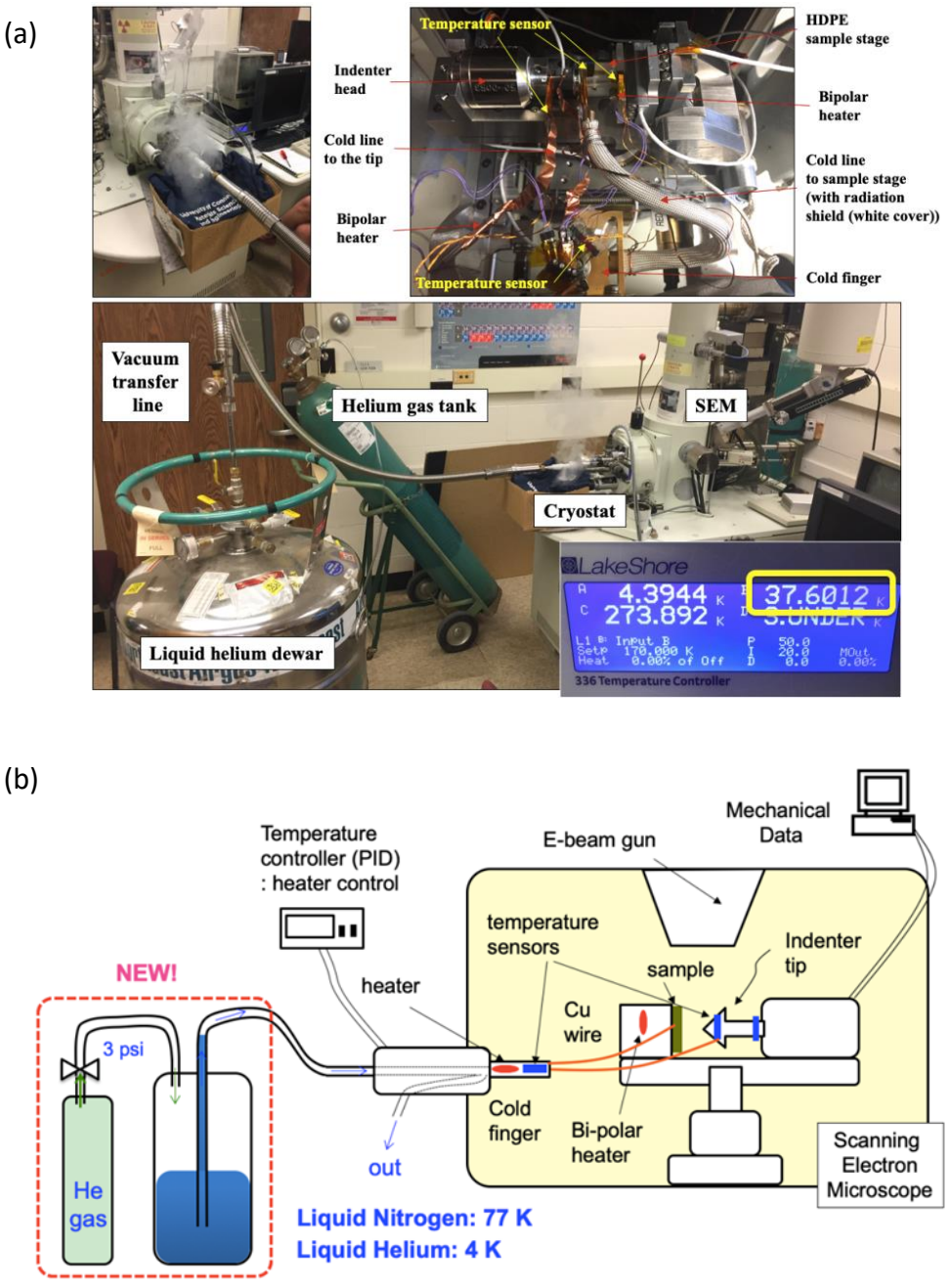


**Figure 1.14. (a) The photo of custom-built cryogenic system, (b) the cartoon schematic of the system** [55]

A liquid nitrogen (LN) and helium (LHe) cryostat, ST-100, (Janis Research Company, USA) was used to perform *in-situ* micro-mechanical testing at low temperatures to investigate the temperature effects (**Figure 1.14(a)**) [55]. The system is composed of three subsystems.

(1) A cold finger, a sample stage, and wires connecting the temperature sensors

(2) A cryostat, a transfer line, and a cryogenic liquid tank

(3) A temperature controller

The subsystem (1) is inside the SEM chamber. The sample stage and wires should be installed only when the cryogenic temperature tests are needed. Because the space is limited, the wires should be arranged well in order to avoid touching each other and hindering the motion of sample stage. It is important to check whether or not all the wires are connected properly before closing the chamber. The cold finger is in direct contact with liquid coolant and removes heat from the sample via a cold line with radiation shield. Even though the temperature of the cold finger reaches near 4 K, the lowest temperature achieved at the sample stage so far is 37.6 K with LHe. It is because of inevitable cold loss due to heat transfer from the sample stage as well as radiation from the SEM chamber.

To minimize this cold loss and cool down the sample stage as much as possible, the sample stage and connections were carefully designed [56,57]. Most importantly, the sample stage needed to be effectively heat-shielded in order for maintaining the coldness. Thus, the material was chosen based on the low thermal conductivity and sufficient stiffness, a high-density polyethylene (HDPE). HDPE has a low thermal conductivity (~0.49 $Wm^{-1}K^{-1}$), which is only ~2% of that of alumina (~30 $Wm^{-1}K^{-1}$) and titanium (~20 $Wm^{-1}K^{-1}$). In the test with alumina and titanium stages, it took more than 10 hours to achieve 130 K. However, HDPE sample stage was

cooled down to 40 K only within one hour (**Figure 1.15(a)**). Therefore, the HDPE sample stage has been used for all the *in-situ* cryogenic micro-mechanical testing.

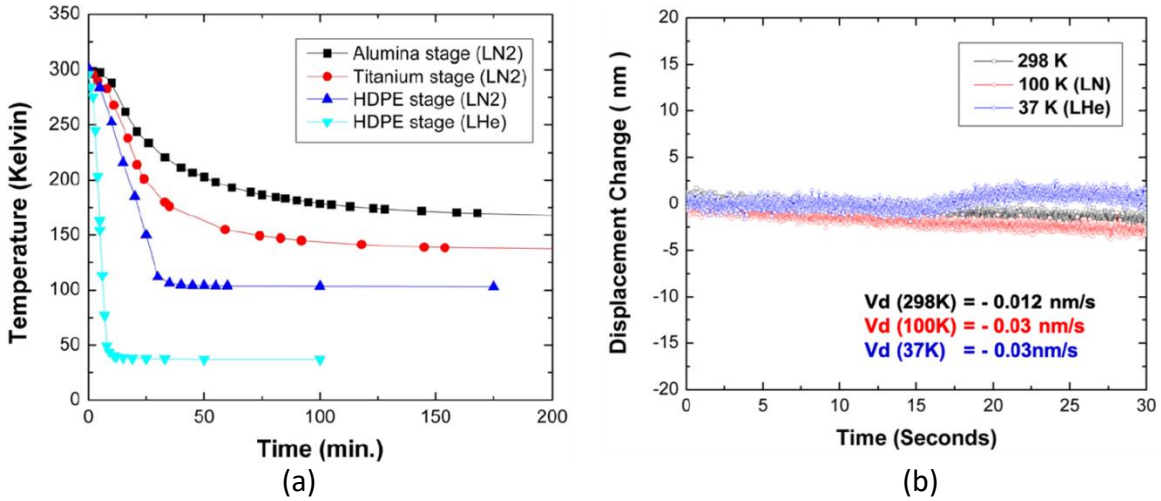


**Figure 1.15. (a) The temperature profile of sample stage with High-Density-Poly-Ethylene (HDPE), alumina, and titanium, (b) The thermal drift data after cryogenic micromechanical tests. The small thermal drift guarantees the minimal error in displacement** [58,59]**.**

After the sample stage, temperature sensors, and wires are assembled precisely, the subsystem (2) can be installed. The following steps are to insert the transfer line into a cryogenic tank and to plug the cryostat to the cold finger that is attached to the SEM chamber. Before proceeding, the transfer line must be vacuumed in order to avoid clogging of condensed frozen water. It is recommended to vacuum the line before starting a test if it was exposed to cryogenic condition in the previous test. Once it is vacuumed, the transfer line should be inserted into a cryogenic tank. Depending on the situation, the tank can be an as-received-cylinder or a Dewar[55]. Because the liquid inside the tank is extremely cold, it is easy that any moisture gets frozen and stops the liquid flow. Thus, it is important to insert the line slowly and make the liquid flow through the line as soon as the line is inserted to the tank. This can be done by

slightly building up pressure inside the tank. For LN, it builds pressure easily by itself if one controls the valve properly. However, for LHe, it is not easy to build enough pressure to make the liquid flow by itself. Therefore, it requires an additional Helium gas tank to be attached to the liquid tank (**Figure 1.14(b)**). When the insertion is successful, one must be able to feel coldness coming out of the cryostat. It may take a couple of minutes to see the flow. However, if nothing comes out of the cryostat, it means that the line is clogged by ice formed inside. Then, the entire line must be taken out of the tank and be dried out until the ice melts and clogging is resolved. It usually takes ~ 40 minutes. Once the line is dried for certain, one needs to vacuum the transfer line again before trying to insert it to the tank.

The subsystem (3) is connected to the outside part of the subsystem (1) through a cable. The cable should be plugged in only when the cryogenic tests are needed. Otherwise, the cable must be plugged out and the controller must remain turned off. The three numbers (temperatures) are read from the subsystem (1). They are the temperatures of the cold finger, the sample, and the bottom of the sample stage. As discussed above at subsystem (1), the difference between the cold finger and the sample shows the collective cold loss and the difference between the sample and the sample stage bottom shows how effective the sample stage shields the heat transfer from the machine.

To note, the diamond tip was not connected to the cold finger to avoid any influence on the force measurement. However, the temperature of the diamond tip was maintained to be similar with that of the sample by using thermal equilibration. This method has been used for high temperature nanoindentation and compression tests for shape memory materials [55]. The literature demonstrated that, at the target temperature (up to 500 $^{o}$C), the diamond tip was brought to the sample surface and remained in contact for at least 30 minutes. In this work, the

cryogenic tests were done at 40 K, which is smaller temperature change than the high temperature tests. Therefore, the method should work as well. In addition to waiting for 30 minutes at least, the thermal contraction of the tip (displacement without loading) was checked until the change becomes negligible. Then, the tip was moved to the sample and the tests were initiated immediately. In this way, most thermal drift measured during the tests to be below 1 nm/sec (**Figure 1.15(b)**) [60].

## 1.7. Computations

Depending on the materials, Density Functional Theory (DFT), Dislocation Dynamics (DD) and Molecular Dynamics (MD) simulations were carried out by ourselves or through close collaborations. For single crystalline BCC metals (Niobium and Molybdenum), we performed uni-axial compression/tension MD at 10-28 um diameter pillars at various temperatures.For single crystalline Niobium, Dr. Ill Ryu`s group in The University of Texas at Dallas (United States) performed uni-axial tension DD at 1 micrometer diameter pillar at low and high temperature by changing the mobility of dislocations and surface nucleation process. For single crystalline $CaKFe_4As_4$, Dr. Roser Valenti`s group in Goethe University (Germany) performed uni-axial compression DFT at 0 K. Here, we only cover MD works, which were done by ourselves.

### Molecular Dynamics

Molecular Dynamics (MD) is a computer simulation to investigate the evolution of a system that consists of particles (atoms and molecules) (**Figure 1.16(a)**) [60]. When the number of

particles is vast, it is not possible to analytically calculate all of their complex interactions and motions. Instead, they can be determined by numerically solving Newton`s equations of motion and averaging them out with a chosen time step. It is useful to see how individual particles behave and the system evolves at the atomistic level for nanoseconds because it is not possible to observe them experimentally. Thus, the combination of experiments and MD simulations is a powerful tool in scientific researches.

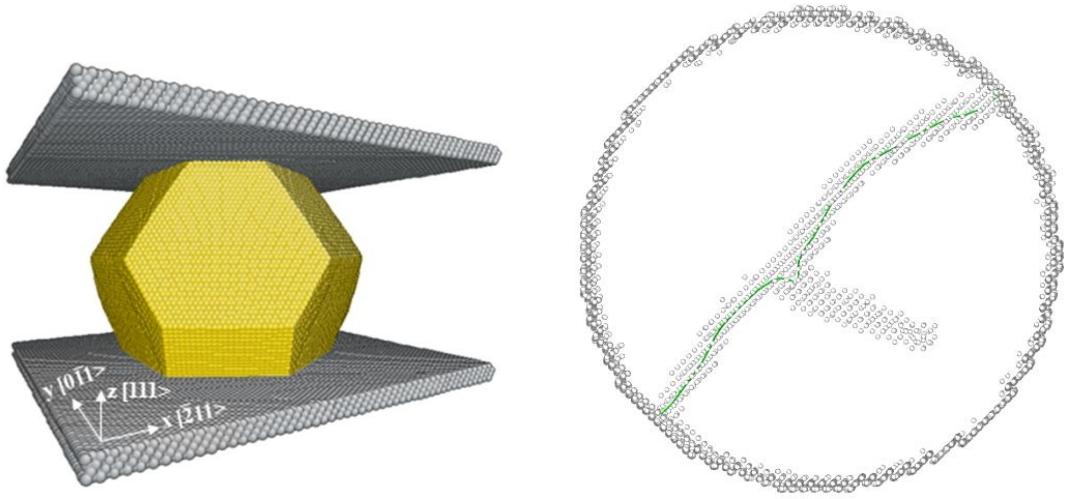


(a) (b)

**Figure 1.16. An image of MD simulation of (a) a gold nanoparticle under compression** [61]**, (b) a niobium nanopillar with a dislocation under tension**

The force between the particles and their potential energies are determined by a potential function, which must be chosen carefully. It is possible that the potential is not properly chosen for the material or condition of interest. Because a calculation will be carried out based on an improper function in the first place, the result will not make sense. Likewise, the selection of constraints requires caution in order to reflect the experimental set-up. There are a number of different potential styles (e.g. Lennard-Jones potential (pair) [62,63], Stillinger-Weber potential and embedded atom model potential (many-body) [64], AGNI potential (machine learning) [65],

etc) and constraints (Microcanonical ensemble (NVE) [66], Canonical ensemble (NVT) [67], Isothermal-isobaric ensemble (NPT) [68], etc)

In order for the computational cost to be realistic and feasible, the length and time scale of the simulation is limited to sub-micrometers and sub-microsecond. The gap between micro-scale and macro-scale is called 'meso-scale' [69,70] and there are on-going works to accomplish filling the gap, called 'coarse-grained model' [71]. It is a model to enable scaling up the size and time by using a peuso-atom that represents a group of N atoms in the system. With that, the number of particles to be calculated is one N-th of the original system. The representation of defects in this coarse-grained model is intensely being studied [72].

In this study, the MD simulations were performed by Large-scale Atomic/Molecular Massively Parallel Simulator (LAMMPS), which is developed in Sandia National Laboratories [73]. The simulations were run on the Storrs HPC cluster at UConn with mostly 12 CPU cores up to 12 hours (general partition). Depending on the number of atoms and the size of the pillars, the running time ranged from 2 hours to 12 hours. The input files (input.lammps) were generated in our personal computer by a program, MD++, developed by Dr. Wei Cai [73]. The program allows one to choose the lattice structure, material, the sample size, the characteristic of a dislocation, etc. Among many deformation methods in LAMMPS, we mostly used NσT ensemble time integration via Nose/Hoover method in order for a dislocation to remain the same initial structure before evolving at specific temperature and stress condition (**Figure 1.16(b)**). The potentials for simulations were chosen after checking their reliability in the temperature and loading conditions of our interest.

## 1.8. Current challenges or issues

### DBT of BCC metals at the micrometer scale

BCC metals are important because they are used a lot in a wide range of industries because they are strong and can also handle extremely high temperatures. With highly advanced technologies, human is exploring more harsh environments, especially space, and will be building industries there. However, sending things to the space is very expensive. Because every kilogram counts, it will be critical to perform more elaborated and sophisticated work with smaller and lighter machines, which are MEMS devices. However, as discussed above, BCC metals are temperature-and-size dependent due to the major role of dislocations in plasticity. Therefore, their Ductile-to-Brittle Transition at small scale must be different from that at bulk scale. However, due to water condensation, temperature control and thermal drift issues, it is difficult to set up a cryogenic micro-mechanical testing, resulting that this topic has been rarely studied.

### Mechanical properties of $CaKFe_4As_4$

Despite a lot of studies on Fe-based pnictides to show high temperature superconductivity and property-tuning, their mechanical properties are rarely studied. Intriguingly, one of the candidates, $CaKFe_4As_4$ exhibited that its high temperature superconductivity at 33K can be turned off and on again under hydrostatic pressure. This temperature can be achieved in space so the material has a huge potential. Most of superconductor materials fracture less than 2 %, which makes them difficult to be used. That makes the superelasticity of $CaKFe_4As_4$ via bond making and breaking very promising. However, because hydrostatic pressure does not cause shear force,

the deformation without breaking is easy. Plus, it is not easy to make an engineering system with hydrostatic pressure. Thus, it needs to be tested under uni-axial stress tests in order to prove true superelasticity and the potential usage of superconductivity switching.

## 1.9. Outline of the dissertation

Chapter 1 provided the general background to introduce why the low temperature effect on mechanical properties at small scale is important to study. The experiments and computation parts followed to explain the methods that were used in this study.

Chapter 2 is to study the effect of low temperature and pre-straining on DBT in [0 0 1] Nb micron-sized samples. The dog bone samples on single crystalline [0 0 1] Nb were made by focused ion beam milling and tested in uni-axial tension at cryogenic temperatures. It was observed that the cross-slip probability of dislocations affects DBT, which can be caused by two completely opposite reasons. The result was discussed in terms of temperature-dependent dislocation evolution using transmission electron microscopy as well as DD simulation.

Chapter 3 is to study the effect of temperature on Surface-controlled dislocation multiplication in bcc metals nanopillars. MD++ was used to make the initial simulation samples, which are single crystalline metal nanopillars with one screw dislocation. LAMMPS was used to perform constant uni-axial compression tests at various temperatures. The simulation showed that the dependence of surface-controlled dislocation multiplication on temperature dramatically changes at three different temperature regimes.

Chapter 4 is to study superelasticity of an intermetallic compound, $CaKFe_4As_4$ and its temperature dependence. The micropillars were made on single crystalline [0 0 1] $CaKFe_4As_4$ by

focused ion beam milling and tested in uni-axial compression at cryogenic temperature. The elastic limit of the material exhibited 17 %, which can be explained by lattice collapse along c-axis and manifested by DFT calculation. It was notable that the temperature dependence of $CaKFe_4As_4$ was negligible down to 40 K, which differs from $CaFe_2As_2$.

Chapter 5 summarizes this dissertation and discusses the future work that can further deepen the understanding of materials at small scale at low temperature. Because some materials can show superconductivity near 0 K, the mechanical properties of materials can potentially be coupled with it and change unexpectedly. Thus, a few ideas as the next steps of this study and the methods to execute them are proposed.

## 1.10. References


[1] K.J. Rebello, Proceedings of the IEEE 92 (2004) 43–55.

[2] K. Gilleo, L.L.C. ET-Trends, R.I. Warwick, Circuits Assembly 16 (2005) 32.

[3] C.M.N. Brigante, N. Abbate, A. Basile, A.C. Faulisi, S. Sessa, IEEE Transactions on Industrial Electronics 58 (2011) 3234–3241.

[4] S. Lee, I. Kim, S. Ha, C. Yu, J. Noh, S. Pae, J. Park, in: 2015 IEEE International Reliability Physics Symposium, 2015, pp. 4B–1.

[5] D.-W. Kim, M. Li, K.H. Yeo, Y.Y. Yeoh, S.D. Suk, K.H. Cho, K. Oh, W.-S. Lee, in: 2008 IEEE International SOI Conference, 2008, pp. 117–118.

[6] K. Gibbs, TechInsight, January (2016).

[7] C.C. Hays, C.P. Kim, W.L. Johnson, Physical Review Letters 84 (2000) 2901.

[8] H.J. Chang, D.H. Kim, Y.M. Kim, Y.J. Kim, K. Chattopadhyay, Scripta Materialia 55 (2006) 509–512.

[9] W. Cai, W.D. Nix, Imperfections in Crystalline Solids, Cambridge University Press, 2016.

[10] W. Cai, V. v Bulatov, J. Chang, J. Li, S. Yip, Dislocations in Solids 12 (2004) 1–80.

[11] M.R. Gilbert, S. Queyreau, J. Marian, Physical Review B 84 (2011) 174103.

[12] R.C. Ehemann, J.W. Nicklas, H. Park, J.W. Wilkins, Physical Review B 95 (2017) 184101.

[13] J. Chaussidon, M. Fivel, D. Rodney, Acta Materialia 54 (2006) 3407–3416.

[14] A.S. Schneider, D. Kaufmann, B.G. Clark, C.P. Frick, P.A. Gruber, R. Mönig, O. Kraft, E. Arzt, Physical Review Letters 103 (2009) 105501.

[15] A. Lawley, H.L. Gaigher, Philosophical Magazine 10 (1964) 15–33.

[16] H. Bei, Y.F. Gao, S. Shim, E.P. George, G.M. Pharr, Physical Review B 77 (2008) 60103.

[17] S. Ryu, K. Kang, W. Cai, Proceedings of the National Academy of Sciences 108 (2011) 5174–5178.

[18] M.J. Cawkwell, K.J. Ramos, D.E. Hooks, T.D. Sewell, Journal of Applied Physics 107 (2010) 63512.

[19] T. Zhu, J. Li, K.J. van Vliet, S. Ogata, S. Yip, S. Suresh, Journal of the Mechanics and Physics of Solids 52 (2004) 691–724.

[20] D. Lorenz, A. Zeckzer, U. Hilpert, P. Grau, H. Johansen, H.S. Leipner, Physical Review B 67 (2003) 172101.

[21] Z.M. Wang, G.J. Shiflet, Metallurgical and Materials Transactions A 27 (1996) 1599–1609.

[22] A.O. Bergholm, (1957).

[23] J.R. Rice, Journal of the Mechanics and Physics of Solids 40 (1992) 239–271.

[24] A.N. Stroh, The London, Edinburgh, and Dublin Philosophical Magazine and Journal of Science 46 (1955) 968–972.

[25] P.B. Hirsch, S.G. Roberts, J. Samuels, Revue de Physique Appliquée 23 (1988) 409–418.

[26] C. Marichal, H. van Swygenhoven, S. van Petegem, C. Borca, Scientific Reports 3 (2013) 2547.

[27] R. Hoffman, C. Zheng, The Journal of Physical Chemistry 89 (1985) 4175–4181.

[28] P.C. Canfield, S.L. Bud'ko, N. Ni, A. Kreyssig, A.I. Goldman, R.J. McQueeney, M.S. Torikachvili, D.N. Argyriou, G. Luke, W. Yu, Physica C: Superconductivity 469 (2009) 404–412.

[29] J.T. Sypek, H. Yu, K.J. Dusoe, G. Drachuck, H. Patel, A.M. Giroux, A.I. Goldman, A. Kreyssig, P.C. Canfield, S.L. Bud'ko, others, Nature Communications 8 (2017) 1–9.

[30] A. Lai, Z. Du, C.L. Gan, C.A. Schuh, Science 341 (2013) 1505–1508.

[31] W.D. Callister, D.G. Rethwisch, Materials Science and Engineering: An Introduction, Wiley New York, 2018.

[32] Y.N. Cui, P. Lin, Z.L. Liu, Z. Zhuang, International Journal of Plasticity 55 (2014) 279–292.

[33] J.A. El-Awady, M. Wen, N.M. Ghoniem, Journal of the Mechanics and Physics of Solids 57 (2009) 32–50.

[34] M.D. Uchic, P.A. Shade, D.M. Dimiduk, Annual Review of Materials Research 39 (2009) 361–386.

[35] S.-W. Lee, W.D. Nix, Philosophical Magazine 92 (2012) 1238–1260.

[36] G. Song, T. Kong, K.J. Dusoe, P.C. Canfield, S.-W. Lee, Journal of Materials Science 53 (2018).

[37] C.-C. Wang, J. Ding, Y.-Q. Cheng, J.-C. Wan, L. Tian, J. Sun, Z.-W. Shan, J. Li, E. Ma, Acta Materialia 60 (2012) 5370–5379.

[38] D. Jang, C.T. Gross, J.R. Greer, International Journal of Plasticity 27 (2011) 858–867.

[39] Q.-J. Li, E. Ma, Materials Research Letters 6 (2018) 283–292.

[40] Q.-J. Li, B. Xu, S. Hara, J. Li, E. Ma, Acta Materialia 145 (2018) 19–29.

[41] P. Singh, M. Ohring, Journal of Applied Physics 56 (1984) 899–907.

[42] P.H. Sun, M. Ohring, Journal of Applied Physics 47 (1976) 478–485.

[43] J. Sun, L. He, Y.-C. Lo, T. Xu, H. Bi, L. Sun, Z. Zhang, S.X. Mao, J. Li, Nature Materials 13 (2014) 1007–1012.

[44] L. Tian, J. Li, J. Sun, E. Ma, Z.-W. Shan, Scientific Reports 3 (2013) 2113.

[45] R. Raj, M.F. Ashby, Metallurgical Transactions 2 (1971) 1113–1127.

[46] X.W. Gu, C.N. Loynachan, Z. Wu, Y.-W. Zhang, D.J. Srolovitz, J.R. Greer, Nano Letters 12 (2012) 6385–6392.

[47] J. Michler, K. Wasmer, S. Meier, F. Östlund, K. Leifer, Applied Physics Letters 90 (2007) 43123.

[48] F. Östlund, K. Rzepiejewska-Malyska, K. Leifer, L.M. Hale, Y. Tang, R. Ballarini, W.W. Gerberich, J. Michler, Advanced Functional Materials 19 (2009) 2439–2444.

[49] A.R. Beaber, J.D. Nowak, O. Ugurlu, W.M. Mook, S.L. Girshick, R. Ballarini, W.W. Gerberich, Philosophical Magazine 91 (2011) 1179–1189.

[50] R. Liontas, J.R. Greer, Acta Materialia 133 (2017) 393–407.

[51] Y. Zou, P. Kuczera, A. Sologubenko, T. Sumigawa, T. Kitamura, W. Steurer, R. Spolenak, Nature Communications 7 (2016) 1–7.

[52] D. Kiener, C. Motz, M. Rester, M. Jenko, G. Dehm, Materials Science and Engineering: A 459 (2007) 262–272.

[53] S. Pathak, S.R. Kalidindi, J.S. Weaver, Y. Wang, R.P. Doerner, N.A. Mara, Scientific Reports 7 (2017) 1–12.

[54] J.R. Greer, W.C. Oliver, W.D. Nix, Acta Materialia 53 (2005) 1821–1830.

[55] G. Song, V. Borisov, W.R. Meier, M. Xu, K.J. Dusoe, J.T. Sypek, R. Valent\'\i, P.C. Canfield, S.-W. Lee, APL Materials 7 (2019) 61104.

[56] S.-W. Lee, M. Jafary-Zadeh, D.Z. Chen, Y.-W. Zhang, J.R. Greer, Nano Letters 15 (2015) 5673–5681.

[57] S.-W. Lee, L. Meza, J.R. Greer, Applied Physics Letters 103 (2013) 101906.

[58] C.A. Schuh, J.K. Mason, A.C. Lund, (n.d.).

[59] J.C. Trenkle, C.E. Packard, C.A. Schuh, Review of Scientific Instruments 81 (2010) 73901.

[60] D. Mordehai, S.-W. Lee, B. Backes, D.J. Srolovitz, W.D. Nix, E. Rabkin, Acta Materialia 59 (2011) 5202–5215.

[61] W.T. Ashurst, W.G. Hoover, Physical Review Letters 31 (1973) 206.

[62] X.-Y. Liu, J.B. Adams, F. Ercolessi, J.A. Moriarty, Modelling and Simulation in Materials Science and Engineering 4 (1996) 293.

[63] F.H. Stillinger, T.A. Weber, R.A. LaViolette, The Journal of Chemical Physics 85 (1986) 6460–6469.

[64] T.D. Huan, R. Batra, J. Chapman, S. Krishnan, L. Chen, R. Ramprasad, NPJ Computational Materials 3 (2017) 1–8.

[65] J.R. Ray, Physical Review A 44 (1991) 4061.

[66] S. Nosé, Molecular Physics 52 (1984) 255–268.

[67] G.J. Martyna, D.J. Tobias, M.L. Klein, The Journal of Chemical Physics 101 (1994) 4177–4189.

[68] V. Bulatov, F.F. Abraham, L. Kubin, B. Devincre, S. Yip, Nature 391 (1998) 669–672.

[69] R.E. Rudd, J.Q. Broughton, Physical Review B 58 (1998) R5893.

[70] G. Agarwal, R.R. Valisetty, R.R. Namburu, A.M. Rajendran, A.M. Dongare, Scientific Reports 7 (2017) 1–12.

[71] G. Agarwal, A.M. Dongare, Computational Materials Science 145 (2018) 68–79.

[72] L. Atomic, M.M.P. Simulator, Available at: Http:/Lammps. Sandia. Gov (2013).

[73] K. Kang, W. Cai, (2005).

# Chapter 2. Uni-axial tension of single crystalline bcc Nb micropillars at cryogenic temperature: Low Temperature Failure Mechanism of [001] Niobium Micropillars under Uniaxial Tension

## 2.1. Introduction

Mechanical properties of materials in a cryogenic environment have been of prime interest for the development of aerospace and deep-sea applications. The mechanical behavior of components at low temperature conditions must be understood to obtain mechanically reliable technologies and desirable performance. Otherwise, the mechanical damage of components can result in unpredictable failure in assemblies and the system as a whole. Recently, the development of small sensors and devices working under extreme conditions has been actively investigated due to their excellent energy efficiency and significant savings in cost and resources [1]. Therefore, it is important to gain a fundamental understanding of deformation and failure mechanisms at small length scales under cryogenic environments.

Failure mechanisms of crystalline materials can differ according to thermal, mechanical, and microstructural conditions, but they are, in general, closely related to how dislocation plasticity suppresses crack propagation. The Rice-Thomson model, which has been the most widely accepted failure process of bcc metals at low temperatures, suggests that the emission of dislocations at a crack tip can suppress the propagation of the crack due to strain hardening in front of the crack tip as well as the relaxation of the strain energy [2,3]. In this case, the failure mechanism is the dislocation-nucleation-limited process. In addition, the mobility of dislocations has been often considered as a critical factor to determine whether brittle failure occurs or not [4]. If the mobility of the dislocations are not high enough to accommodate the imposed strain rate

around the crack tip, failure would occur immediately even though plenty of nucleated dislocations are present. This failure mechanism is a dislocation-mobility-limited process and has been observed in intrinsically brittle materials, such as silicon [5].

For the last two decades, there have been a large number of studies on the influence of sample dimension on dislocation plasticity at the micrometer scale. These studies revealed that small-scale plasticity is controlled primarily by the stochastic operation of truncated dislocation sources, which leads to the size effects on the mechanical behavior of materials [6-10]. Flow strength can increase readily, up to a factor of 10, by reducing the sample dimension down to the micrometer scale [11-13]. Additionally, jerky plastic flow is observed due to intermittent source operation of dislocations [14-17]. More surprisingly, dislocation multiplication can be completely suppressed if the sample volume is sufficiently small enough, for instance, a sub-micrometer dimension [18,19]. All mobile dislocations can be annihilated rapidly at the free surface during plastic deformation before dislocations interact with each other and form another dislocation source. In other words, plastic deformation can make a material mobile-dislocation-free. This phenomenon is called dislocation starvation, which is the antithesis of dislocation multiplication in bulk metals [20,21]. All of these observations indicate that dislocation plasticity and the evolution of dislocation structure at the micrometer scale are different from those at bulk scale. This difference in plasticity mechanism also suggests that the failure process of metals at the micrometer scale could also be different than those at bulk scale because their failure process is closely related to how dislocations behave before fracture occurs. For instance, if the pre-existing mobile dislocations cannot accommodate the imposed strain rate, the occurrence of failure could be determined based on the competition between dislocation nucleation and crack nucleation. If the critical stress of dislocation nucleation is lower than crack nucleation, plastic deformation

will occur continuously because new dislocations can keep generating plasticity. This case has been observed in gold nanopillars under compression at room temperature [11,20]. If the critical stress of dislocation nucleation is higher than crack nucleation, or if stress concentration promotes crack nucleation, brittle failure will occur. So far, the temperature-dependent failure mechanism at the micrometer scale has been investigated primarily by high temperature micro-beam bending testing on materials which are brittle at room temperature, such as tungsten and silicon [22-26]. However, the failure mechanism of metals under uni-axial tension and under cryogenic environment has not been explored, yet. For the past six years, we have developed a state-of-the-art *in-situ* cryogenic micromechanical testing system, which can perform a reliable micro-tensile test at temperatures between 35K and 298K using a liquid helium cryostat [27]. In this study, therefore, we performed *in-situ* cryogenic micro-tensile experiments to unveil the failure mechanism of micron-sized bcc single crystal at cryogenic temperature. We chose bcc niobium (Nb) for this study due to its exceptional ductility at room temperature, the strong temperature sensitivity of mechanical properties, and the practical importance in low temperature applications such as superconducting devices [28,29]. Our *in-situ* cryogenic micro-tensile experiments at 56 and 100K showed significant reduction in tensile ductility, discrete strain bursts, and brittle cleavage morphology of the fracture surface, while those at 298K showed continuous plastic flow and perfect plasticity fracture. Transmission electron microscopy (TEM) on deformed samples showed a dense dislocation network in the sample tested at 298K but an array of nucleated dislocations in the sample tested at 56K. Dislocation dynamic (DD) simulation demonstrated that the suppression of thermally-activated cross-slip at low temperatures prevents dislocation multiplication, resulting in dislocation-starvation. As soon as all mobile dislocations are starved, dislocation nucleation occurs until stress concentration at a slip step nucleates a

crack, the propagation of which leads to catastrophic brittle failure. In other words, the competition between dislocation nucleation and crack nucleation controls the failure process. We believe that this failure mechanism is not limited only to Nb because dislocation starvation can occur in some other metals [20,30,31]. In the dislocation starvation state, if a crack nucleation is promoted by stress concentration, brittle failure can occur regardless of material systems. In this sense, our results and interpretations will give an important insight in fundamental understanding of failure process in metals at the micrometer scale and at low temperature.

## 2.2. Results and Discussion

### *In-situ Micro-tensile Experiments*

Failure processes of metals can be investigated in various ways, the two most common of which are the uniaxial tensile test and the fracture toughness test [25,32-35]. Here, we chose the former because we want to examine how the dislocation plasticity, i.e., the source-controlled plasticity at the micrometer scale, influences the failure process. Fracture toughness measurements with a pre-notched sample could be a better method to study crack propagation, but the samples used in these tests are designed to suppress dislocation plasticity and to promote atomic debonding at the crack tip. Thus, a uniaxial tensile test is the preferred method to observe the effects of source-controlled dislocation plasticity on the failure process. Micro-tensile samples of single-crystalline Nb with a cross-sectional area of~$2.5^2 \mu m^2$ on average were fabricated along the [001]-direction. The [001] orientation was selected to ensure that dislocation multiplication occurs easily at room temperature through prolific dislocation interactions. Micro-tensile stress-strain data were obtained at three different temperatures, 56K, 100K, and 298K. Thermal drift was minimized to 0.5 nm/s by simultaneous cooling of both the tip and sample,

resulting in a negligible error in displacement measurements and corresponding strain calculations.

Scanning electron microscope (SEM) snapshots of *in-situ* micro-tensile tests show that the micropillar at 298K exhibits conventional deformation and fracture behavior of ductile metals (FIG. 1(a)). Necking occurred in the middle of the gauge section, and fracture occurred at the necking region. In contrast, the micropillars tested at 56K and 100K did not show any visual signs of necking. Rather, fracture occurred with limited plasticity (FIG. 1(b)). Videos of micro-tensile tests at 298K and 56K are available as Supplementary Movies 1 and 2, respectively. More interestingly, the stress-strain data confirms distinctively different mechanical behaviors (FIG. 2(a)). At 298K, the micropillar initially exhibits a smooth and continuous stress-strain curve, however the latter stages of deformation exhibit strain-burst behavior. Note that a strain burst is the section of the stress-strain curve between stress drops that occur due to a feedback loop response of the displacement control. If a strain burst occurs, the displacement rate abruptly rises. Then, the instrument rapidly reduces the load to normalize the displacement rate, this phenomenon leads to a drop in stress immediately after each strain burst occurs. The micropillar tested at 298K fractured at ~23% of the total % elongation. At 56K and 100K, however, the micropillars exhibited several large strain bursts at the beginning of plastic deformation and followed by fracture. The flow stresses measured at 56K and 100K are much higher than that of the sample tested at 298K, but the total % elongation at fracture is only around 5%.

The higher flow stress of Nb at low temperature is usually understood based on the temperature-dependent intrinsic lattice resistance [6,7]. At a low temperature, the operation of dislocation sources requires higher applied stress due to the increase in intrinsic lattice resistance. However, the transition from smooth plastic flow (298K) to discrete source-controlled plasticity

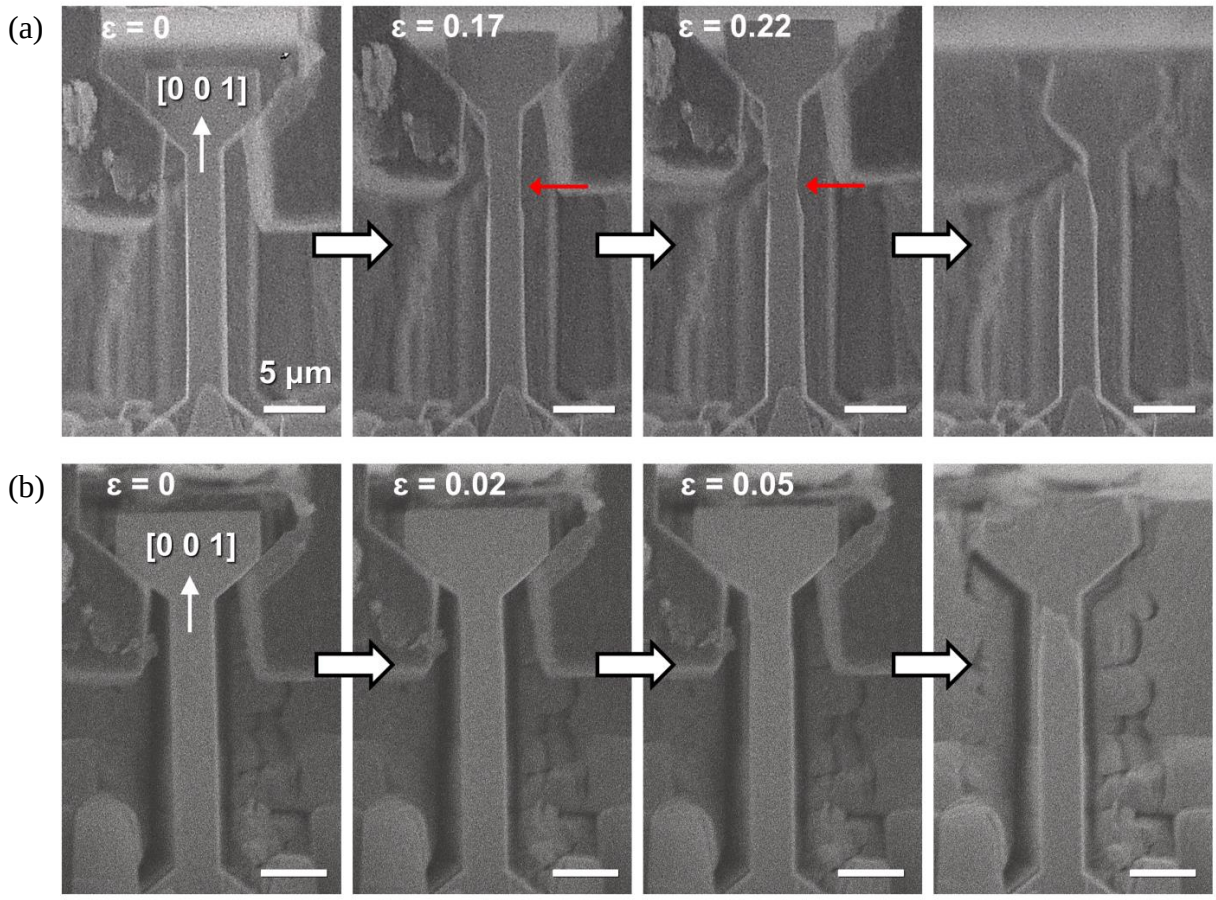


**Figure. 2.1. Snapshots of *in-situ* micro-tensile tests at (a) 298K and (b) 56K. Red arrows in (a) indicate the formation of necking. The length of the scale bars is 5μm.**

(56K and 100K) as the temperature decreases needs to be understood carefully. High-resolution SEM images clearly show that wavy slip traces are densely and widely spread on the surface of the sample tested at 298K (FIG. 2(b, left and middle)) whereas straight and highly localized slip traces, which possess a step height larger than that at 298K, were developed on the surface of the sample tested at 56K (FIG. 2(c, left and middle)). Note that the decrease in temperature may not modify the initial dislocation structure because the increase in intrinsic lattice resistance stabilizes the initial dislocation structure. If a similar initial dislocation structure is considered,

the evolution path of the dislocation structure seems to change significantly as the temperature decreases. Duesbery *et al.* found that slip traces of Nb bulk single crystals become straighter as the temperature decreases [36]. They explained this straightening of slip traces in terms of suppression of cross-slip of screw dislocation at a low temperature. Because cross-slip is a thermally activated process, cross-slip probability usually decreases as the temperature decreases. At the micrometer scale, if a cross-slip of screw dislocation is suppressed, a dislocation source would operate on its initial slip plane for a long time and could produce a relatively large straight slip step, leading to a strain burst. On the other hand, cross-slip events can occur abundantly at 298K. So, the dislocation structure could evolve into much more complicated 3D network structures, where plenty of slip traces can be generated (FIG. 2(b, left and middle)).

The significant reduction of % elongation at low temperatures can be understood by fractography. The sample tested at 298K shows a pointy fracture surface (FIG. 2(b, left)), which is evidence of perfect plasticity fracture, which corresponds to the failure as a result of the continuous plasticity. In this case, dislocation plasticity occurs continuously until fracture occurs at two pointy regions. The position of the fracture point is close to the middle of sample cross-section (FIG. 2(b, right)), implying that multi-slip occurred almost equally on all available slip planes. However, the sample tested at 56K shows a brittle cleavage fracture surface (FIG. 2(c, right)). The rough fracture surface implies that brittle fracture occurs via local atomic debonding. Note that the 5% of ductility is attributed to the highly localized slip bands, which actually do not form necking. Although some ductility is present, we have not seen the cup-and-cone fracture morphology, which is the typical signature of the ductile fracture. Thus, the Nb micropillars seem to exhibit brittle failure after the occurrence of a few strain bursts at low temperatures.

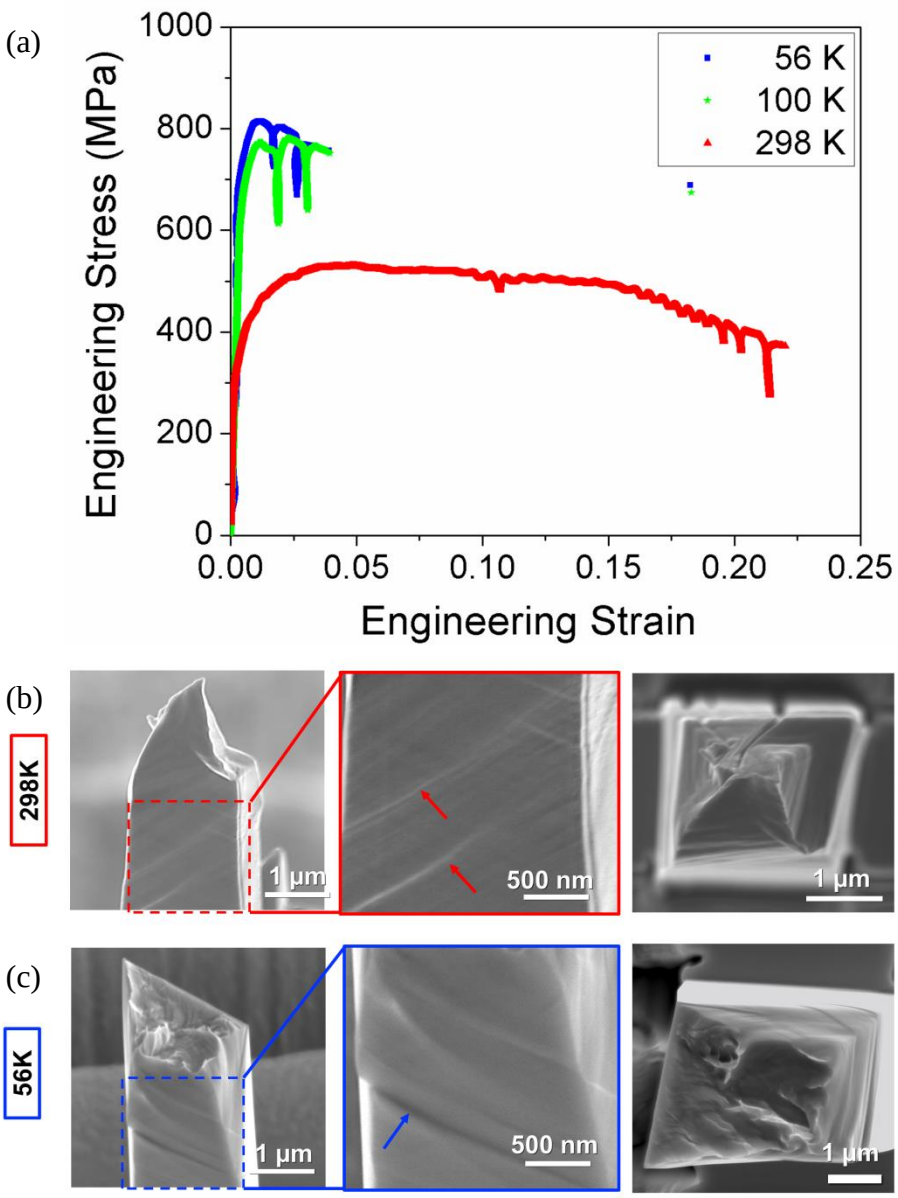


**Figure. 2.2. (a) Representative stress-strain data at 298K, 100K, and 56K; Sideview of the sample fractured at (b, left) 298K and (c, left) 56K; The magnified image of slip traces for (b, middle) 298 K and (c, middle) 56K. The red and blue arrows indicate the wavy slip traces and the straight slip trace, respectively; Fracture surface of the sample fractured at (b, right) 298K and (c, right) 56K.**

*Evolution of Dislocation Structures*

The failure process is related to the dislocation plasticity before fracture occurs [4,5]. In order to obtain the mechanistic description of the failure process, therefore, it is critical to understand how dislocations behave in our samples at different temperatures. Obtaining a clean dislocation image of bcc metals is often challenging because FIB milling sometimes forms a thin amorphous layer on the surface of the TEM samples. In our case, the usage of FIB milling is unavoidable due to the small dimension of the specimens. Fortunately, most dislocations are visible in our TEM images (FIG.s 3(a)-(d)) after image processing, which enhances the contrast of dislocation structures.

As-received Nb sample is well-annealed during single crystal growth (FIG. 3(a)), so the micro-tensile samples are expected to contain few dislocation sources before mechanical testing. We observed the dislocation structure near the fracture surface of samples tested at 298K and 56K. The sample tested at 298K shows a dense dislocation structure at the fracture strain, ~23% (FIG. 3(c)), confirming that dislocation multiplication occurred extensively. This result is consistent with the dislocation multiplication in Nb nanopillars under compression at room temperature [37]. Interestingly, however, the sample tested at 56K showed an array of dislocations at the fracture strain, ~5% (FIG. 3(d)). One might think that this comparison is unfair because the sample tested at 298K underwent substantial amount of plastic deformation. Therefore, TEM analysis was also performed on the sample strained only up to ~5% strain at 298K, which corresponds to the fracture strain of the sample tested at 56K. The dense dislocation structure was found again (FIG. 3(c)), which appears to be similar with that observed at the fracture strain of 23% (FIG. 3(b)). These results indicate that at 298K, the number of dislocations increases rapidly at the early stage of deformation but does not change much after the middle of plastic

deformation. At the micrometer scale, dislocations can be annihilated at the free surface readily, so a steady state of dislocation density could be reached due to the balance between dislocation multiplication and annihilation rates. This explains the small increase in dislocation density after 5% strain. Once a neck forms, the plastic volume becomes smaller, and the dislocation annihilation rate at the neck region becomes higher. Then, a small number of dislocation sources are available in such a small neck region, so the strain bursts of source-controlled plasticity is shown more distinctively at the later stage of deformation. This explains the presence of strain burst at the last stage of plastic deformation at 298K (FIG. 2(a)).

TEM results show that the path of dislocation evolution is different between 298K and 56K. The dislocation structure evolves into the denser and more complicated structure at 298K, whereas a sample at 56K contains the parallel arrays of dislocations. By comparing the trajectory of dislocations with the crystallography of slip planes, we confirmed that all dislocations are mobile dislocations on {111} planes (FIG. 3(d)). Note that it is almost geometrically impossible for the few initial grown-in dislocations to form the parallel arrays of dislocations after plastic deformation. The initial grown-in dislocation on {111} planes could move quickly out of micropillar during plastic deformation. Therefore, all dislocations in FIG. 3(d) appear to be new dislocations that are nucleated consecutively from the free surface. This similar behavior was observed in Mo alloy nanofiber [31]. One might argue that FIB damages (e.g. Ga implantation, interstitial loop, vacancy loop) produce single arm dislocation sources that produce the observed dislocation arrays [38]. By assuming that a single arm source is created in the FIB damage layer near the free surface, the source operation stress can be estimated [39]. The majority of FIB damage is present within a 20 nm thick layer in the surface region. Then, if the FIB damage forms a

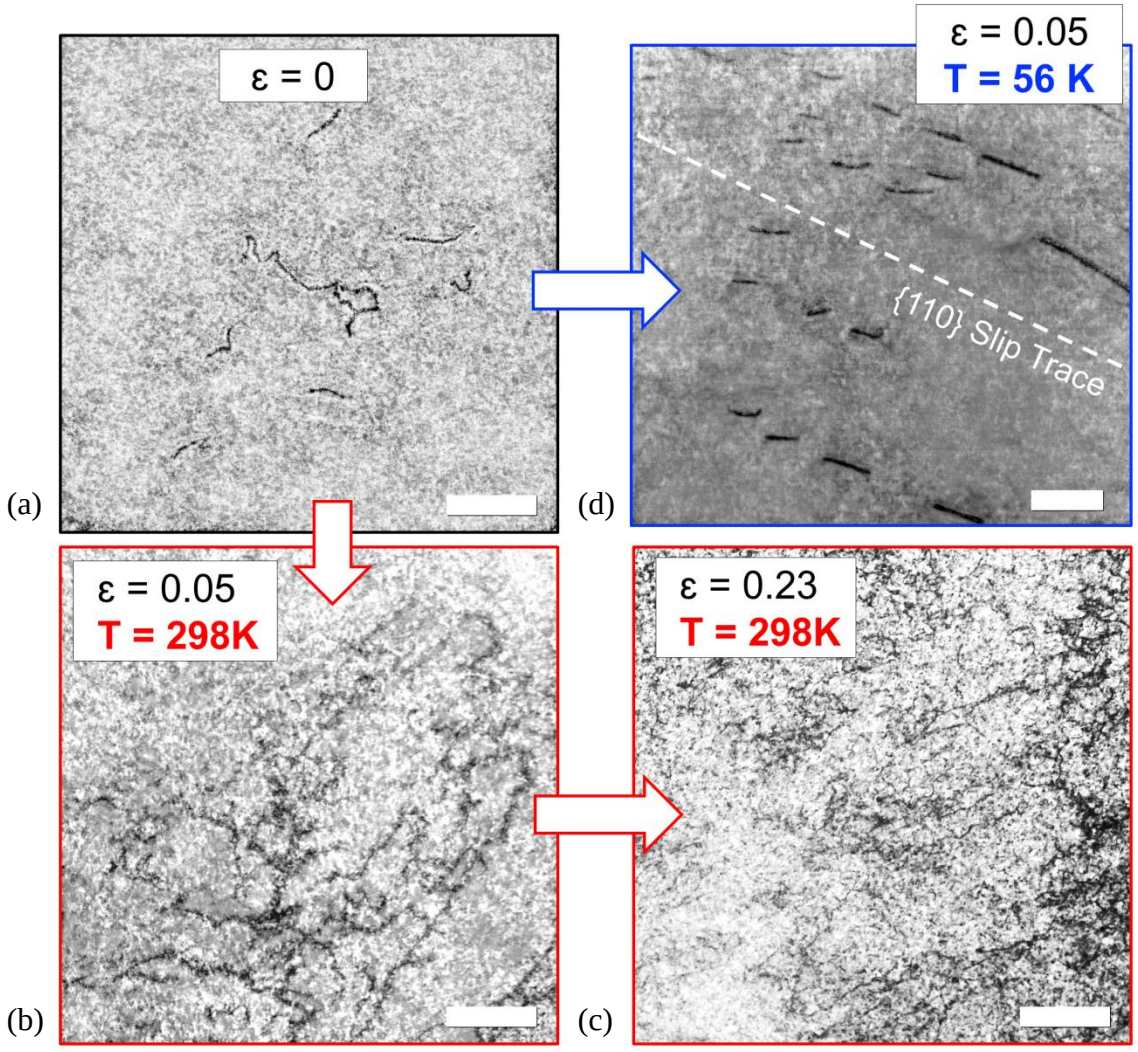


**Figure. 2.3. Dislocation structure (a) as received; (b) at ~5% of axial strain (298K) and (c) at ~23% of axial strain (298K); (d) at ~5% of axial strain (56K); The length of the scale bars is 200 nm. All TEM images here are observed in [100] zone axis with g = [101].**

single arm dislocation source, the shortest length of the dislocation source, which provides the highest resistance of source operation, could also be approximately ~20 nm. According to the measured dislocation density ($3.50\times10^{13}m^{-2}$ from FIG. 3(a)), the single arm source model[39] predicts over 1.5 GPa of the axial stress to operate single arm source, and this estimation is much

higher than experimental data. Instead of the creation of single arm dislocation source, therefore, FIB damages could induce a local lattice distortion, lower the barrier of the dislocation nucleation, and eventually promote the nucleation of dislocations at the free surface. The phenomenon, the removal of pre-existing mobile dislocations, has been termed dislocation starvation, which has been observed in Au (290 nm in diameter) [20] and Ni (150 nm in diameter) nanopillars [30] and Mo alloy nanofibers (100~150 nm in diameter) [31]. Usually, dislocation starvation is observed when a sample's dimensions are extremely small such as the sub-micrometer scale. However, our results show that it is possible to observe dislocation starvation even at the micrometer scale if dislocation multiplication is suppressed effectively by decreasing the temperature.

*Dislocation Dynamics*

In an effort to investigate the details of the evolution of dislocation structures, DD simulation has been widely used to model micro-mechanical tests directly at the micrometer scale [40-42]. In this work, we modified ParaDiS (Parallel Dislocation Simulator) code to examine the dislocation source mechanisms at different temperatures and their corresponding plastic flow behavior [43,44], and simulated two different temperature cases (FIG.s 4, 5, and 6). From atomistic simulations, edge dislocations have a much higher dislocation mobility than those of screw dislocations at low temperatures because a screw dislocation has a non-planar core structure and a high Peierls barrier [45-47]. In addition, the motion of screw dislocation in bcc metals is known to be governed by kink-pair nucleation. In our model, the overall effect of the thermally activated process could be captured by assigning a much lower glide mobility to the screw dislocations, following the atomistic modeling results [48]. As the temperature approaches the critical value, the

difference in mobility between edge and screw dislocations decreases [49]. In this study of Nb micropillar plasticity, we make rough approximations on the mobility ratio and perform simulations with two different mobility cases: $M_{edge}=100M_{screw}$ and $M_{edge}=10M_{screw}$. The former condition corresponding to the cryogenic temperature that is far below the critical temperature, and the latter condition corresponding to room temperature that is close to the critical temperature of Nb, 350K [50]. We also performed simulations with lower mobility ratios, up to 5, and the change in overall dislocation behavior and corresponding stress-strain curve is almost negligible.

In bcc metals, dislocation plasticity is mainly driven by the motion of screw dislocations. Following the molecular dynamics results [51], an algorithm for a bcc nanopillar was developed to implement a surface cross-slip process that leads to multiplication without the presence of artificial dislocation sources or pinning points [44]. Further modification was made to take into account the effect of temperature on source mechanisms and accompanying plastic response of Nb micropillars. In previous work [44,52], DD results showed that surface-initiated cross-slip could create a dynamic dislocation source, leading to self-multiplication. Note that the strong image stress near the free surface induces the surface-initiated cross-slip. Thus, the surface-initiated cross-slip is almost an athermal stress-driven process. Our previous MD studies also demonstrated that the surface-initiated cross-slip occurs even at an extremely low temperature [53]. At a low temperature, therefore, we model the surface-initiated cross-slip to occur, but the thermally activated cross-slip of internal dislocation segment is suppressed.

At low temperature, a few screw dislocations exist at the initial stage of loading, and most of them leave out of the micropillar simply by gliding on their slip planes (FIG. 4). For one screw dislocation, however, the surface-initiated cross-slip occurs, and the cross-slipped part

rotates as a single arm dislocation source, giving rise to strain burst in the stress-strain curve. A detailed microstructure evolution can also be seen in Supplementary Movie 3. We confirmed that the surface cross-slipped part of the dislocation has a higher resolved shear stress than the non-cross-slipped part, which serves as an anchoring dislocation due to its slow motion. Thus, the surface-initiated cross-slip produces a dynamic dislocation source. After multiple operations of this dynamic single arm source, the micropillar goes eventually into a mobile dislocation starved state because the dislocation source is annihilated at the free surface. The multiple operation of dynamic dislocation source on a single slip plane explains the presence of large strain bursts in the experimental stress-strain data (FIG. 2(a)) and localized slip steps at 56K and 100K (FIG. 2(c, middle)). DD simulation shows that dislocation starvation inevitably occurs even though a dislocation source is formed in the course of plastic deformation. Then, dislocation nucleation is required to produce the plasticity further. Note that the simulation (FIG. 4(d) and Supplementary Movie 3) stopped when dislocation starvation, which corresponds to the state of no mobile dislocation, is reached because our DD simulation does not simulate the nucleation of new dislocation. The remaining two dislocations correspond to the immobile dislocations that have a Schmid factor of zero. So, FIG. 4(d) corresponds to the state right before the nucleation of the array of dislocations (FIG. 3(d)).

In our DD models for high temperature, surface-initiated cross-slip as well as conventional thermally activated cross-slip of internal dislocation segments were allowed to occur (FIG. 5). Both surface-initiated cross-slip and thermally activated cross-slip produce a large number of dislocation sources, which lead to dislocation multiplication. Contrary to the results at low temperature where samples could reach dislocation starved state, the dislocation density increases throughout the loading step. Supplementary Movie 4 shows a detailed

microstructure evolution at high temperature. The DD stress-strain curve (FIG. 6) shows that our DD modeling shows good agreement with the experimental results. At low temperature, dynamic dislocation sources induce the source-controlled plasticity, which produces the discrete strain burst in stress-strain curve. At high temperature, however, the significant dislocation multiplication produces the smooth and continuous plastic flow. Note that the yield strengths in DD simulations is higher than those in experiments. This result is related to the size effect. The micropillar dimension of DD simulation (1μm) is smaller than that of experiment (2.5μm). We used the smaller dimension to reduce the computational cost, but the dimension used in our DD simulation is still large to enough to capture the essential dislocation behaviors at the micrometer scale.

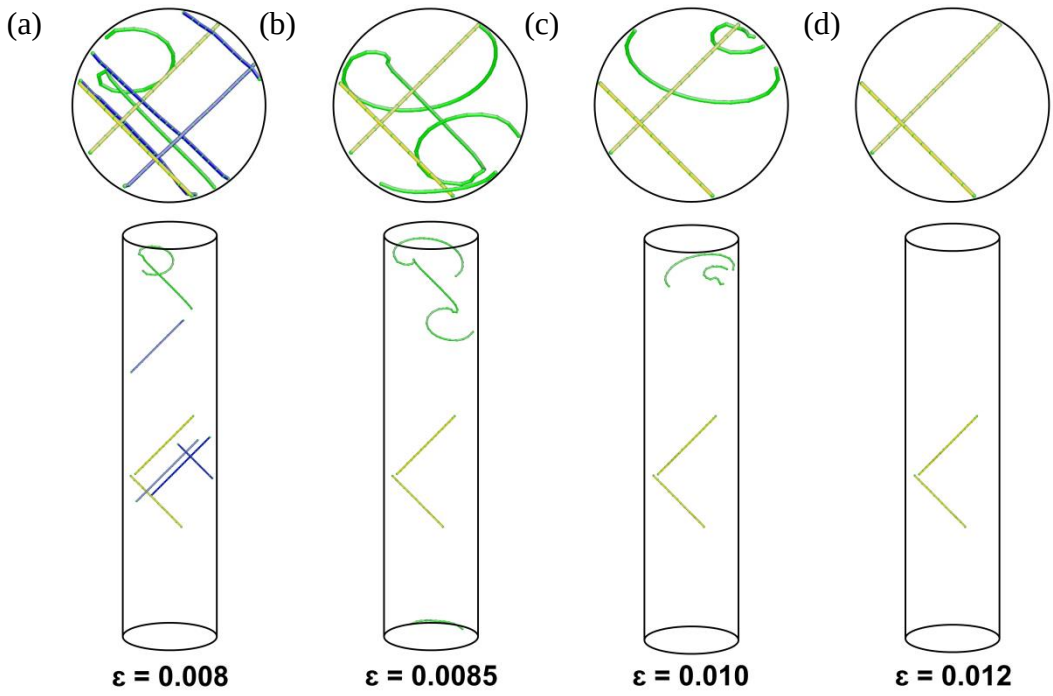


**Figure. 2.4. Snapshots of dislocation motion with surface-initiated cross slip for a cryogenic temperature ($M_{edge}$=100$M_{screw}$) in a Nb micropillar with 1μm in diameter at strain values of (a) 0.7%, (b) 1.0%, (c) 1.6% and (d) 1.7%. The top four figures show the top view of the micropillars, and the bottom four figures show the side view of the micropillars. After the dynamic source is annihilated at the free surface, the micropillar becomes mobile-dislocation-starved.**

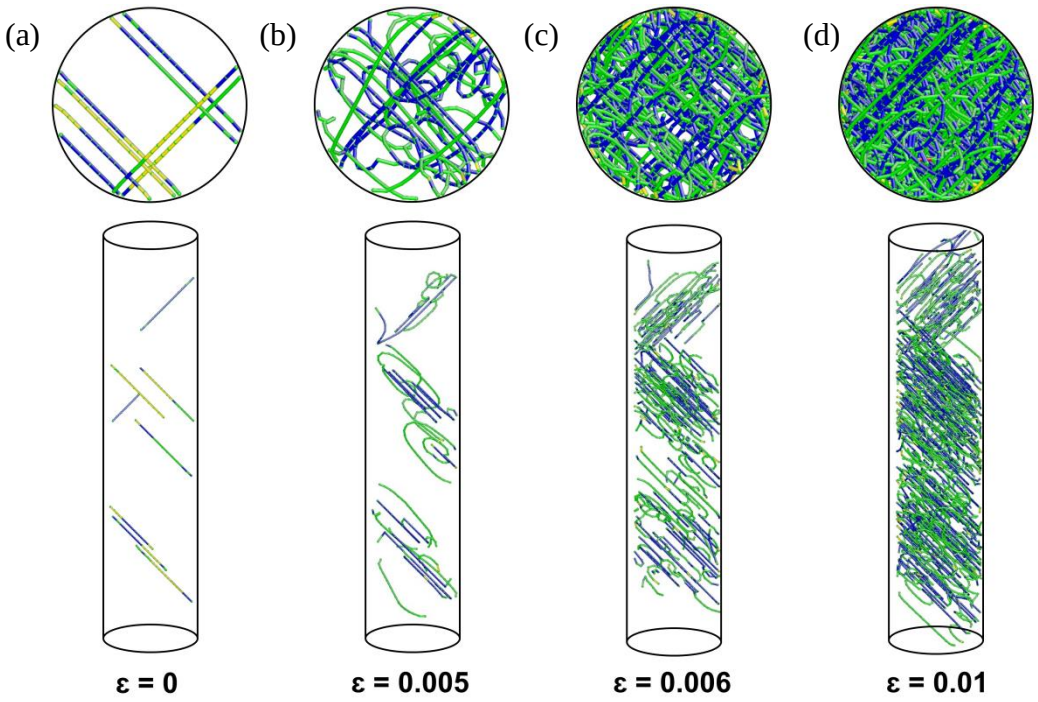


**Figure. 2.5. Snapshots of dislocation motion with surface-initiated cross slip in a Nb micropillar with 1μm in diameter at room temperature ($M_{edge}$=10$M_{screw}$) at strain values of (a) 0%, (b) 0.5%, (c) 0.6% and (d) 1.0%. The dislocation density increases continuously due to the multiplication process.**

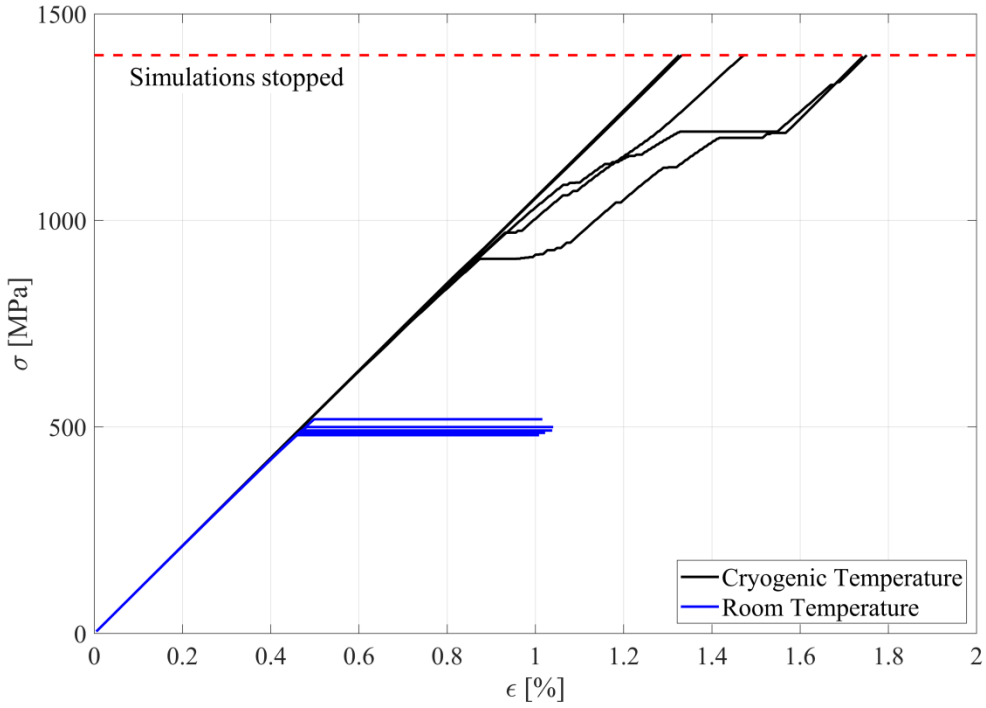


**Figure. 2.6. Stress-strain curves for the 1µm sized micropillars at cryogenic temperature ($M_{edge}$=100$M_{screw}$) and room temperature ($M_{edge}$=10$M_{screw}$) from the DD simulations. Elastic deformation in stress-strain curve at the later stage is a computational artifact due to the absence of dislocation nucleation and fracture in DD simulations.**

*Mechanistic Description of Failure Process*

Brittle failure of bcc metals is closely related to dislocation plasticity. If a dislocation nucleation is limited or the mobility of nucleated dislocations is sufficiently low, the dislocation plasticity cannot relax the stored strain energy, and brittle fracture occurs. In our case, the mobility of dislocation does not appear to be a critical factor even at 56K. The presence of multiple strain bursts in a stress-strain curve (FIG. 2(a)) implies that dislocations are able to move relatively easily. One of the strain bursts has the size of ~0.006 axial strain in [001]-

direction, which corresponds to 200.7 nm of shear displacement in [111]-direction based on the slip geometry. Because the magnitude of Burgers vector of Nb is 0.2860 nm, the strain burst size corresponds to ~700 rotations of the dynamic dislocation source or nucleation/propagation of 700 dislocations on its original slip plane. This estimation indicates that the mobility of dislocation is high enough to generate the plasticity even at low temperature. Therefore, a failure process of Nb micropillar at low temperature should not be dislocation-mobility-limited.

The fracture strain of [100] Nb single crystal appears to be strongly related to the sample dimensions (FIG. 7(a)). At room temperature, [001] Nb shows a fracture strain of nearly 1 at bulk scale [37,54] but ~0.2 at the micrometer scale (our result). At the submicrometer scale, the fracture strain at room temperature is only ~0.03 [55]. Thus, fracture strain decreases significantly as the sample dimension decreases. The decrease in sample size certainly reduces the chance for a dislocation to produce a complex dislocation network because of (1) the rapid annihilation of dislocations at the free surface before they interact with other dislocations and (2) the reduced number of cross-slip occurrence before dislocations reach the free surface. At small length scales, therefore, plastic deformation could be much more localized, leading to smaller fracture strain. In addition, (3) the reduction of temperature suppresses thermally activated cross-slip and prevents the chance of dislocation interaction even further. Therefore, dislocation starvation in our Nb micropillars could result from the combined effects of the size reduction (rapid dislocation annihilation) and the temperature decrease (suppression of cross-slip).

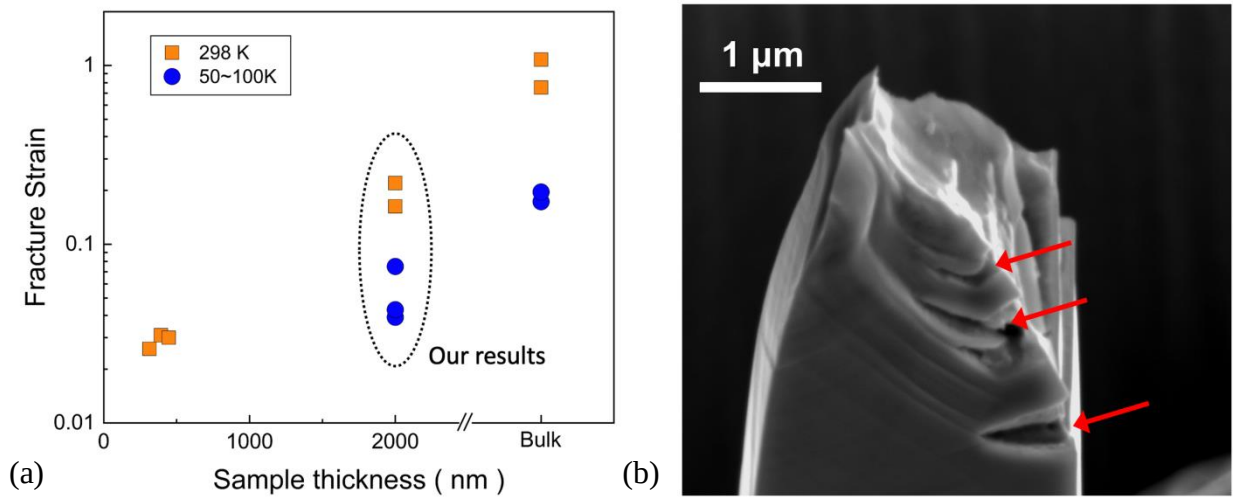


**Figure. 2.7. (a) Size-dependent fracture strain of [001] Nb single crystals. Bulk data were obtained from the referenced works [36,54], and submicron-size data were obtained from the referenced work [55]. Note that the log-scale was used in fracture strain axis; (b) Formation of micro-cracks at slip steps in a sample fractured at 56K. Red arrows indicate the location of micro-cracks that were nucleated at slip steps that dislocations generated.**

As discussed above, dislocations in our specimen seems to be sufficiently mobile even at 56K and 100K. Once pre-existing mobile dislocations are starved during plastic deformation, a material must choose either dislocation nucleation or crack nucleation to relax the stored elastic energy. It is still unclear at which strain dislocation starvation occurs, but as discussed in Section 2.2, the presence of parallel dislocation arrays in the fractured sample at 56K (FIG. 3(d)) suggests strongly that dislocation nucleation occurs prior to fracture. Note that our sample does not need to reach a stress state near the theoretical strength for dislocation nucleation as seen in whiskers [56], Mo-alloy pillars [57], and microparticles [58] because large slip steps, which a

dislocation source produces, can act as a stress concentrator. Also, as discussed in Section 2.2, FIB damages could promote the dislocation nucleation due to local lattice distortions [59].

We assume that the critical stress for dislocation nucleation is slightly lower than the critical stress for crack nucleation at the beginning of plastic deformation. At the state of dislocation starvation, dislocation nucleation could occur at the slip steps that pre-existing dislocations create. Once plastic deformation continues, the sample width becomes smaller, leading to a sudden increase in normal stress (red region in FIG. 8). Stress-strain curves at 56K and 100K show that fracture always occurs at the end of strain burst. Due to the abrupt change in geometry at a slip step, stress concentration could be rapidly developed at the slip step before the feedback response of equipment reduces the applied force, and crack nucleation would become more favorable instantly than dislocation nucleation. Then, brittle fracture would occur immediately once a crack propagates across a sample. SEM images of the sample fractured at 56K show that all micro-cracks are developed exactly at the slip traces produced by dislocations (FIG. 7(b)). This results clearly support the development of stress concentration at a slip step. Our interpretation is relatively similar to Lupinacci, *et al.*'s interpretation on brittle fracture of Sn micropillars in that a stress concentrator, which is created by plasticity process (deformation twinning in Sn micropillars and dislocation slip in Nb micropillars), induces cracking [60]. This failure process is also consistent with the Rice-Thomson model, one of the ideal brittle failure mechanisms, because the brittle failure process in our sample results from the competition between dislocation nucleation and crack nucleation/propagation. In our case, a slip step could be regarded as a pre-notch in the Rice-Thomson model. As soon as a crack nucleation becomes more favorable than dislocation nucleation, brittle fracture occurs immediately. The schematics of fracture process in Nb micropillars at two different temperatures are described in FIG. 8.

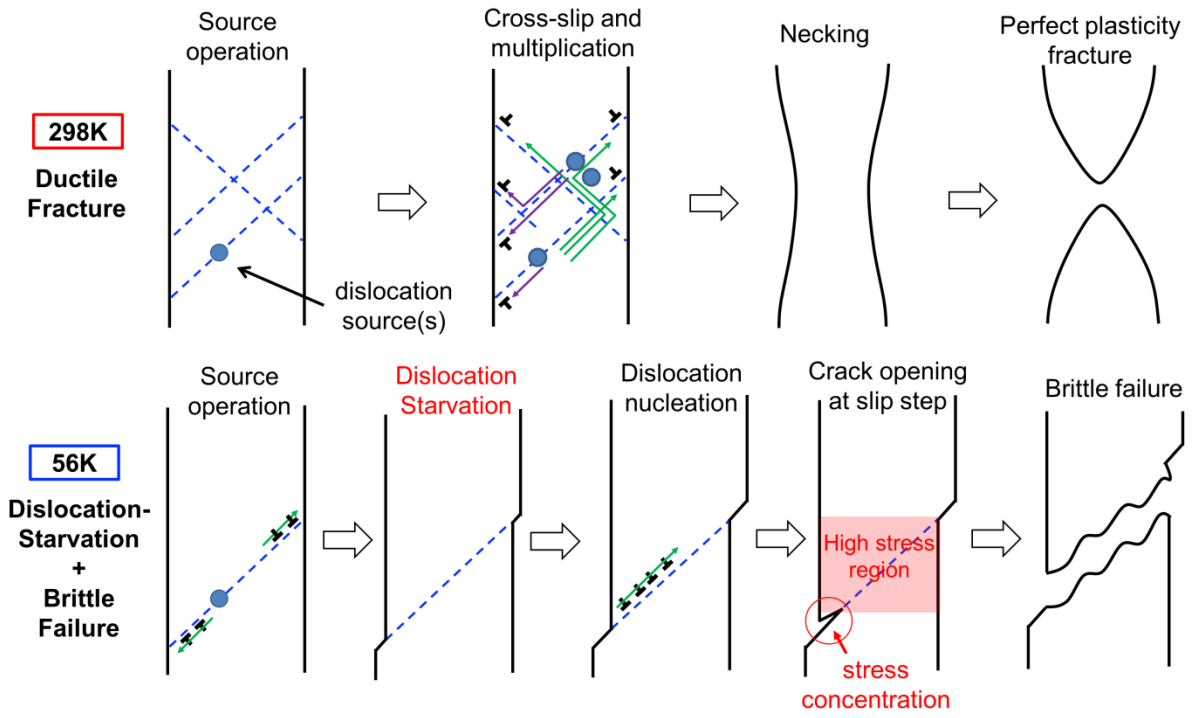


**Figure. 2.8.** Schematics of plastic deformation and fracture processes at the micrometer scale at different temperatures. The red region at 56K indicates the higher stress region due to the reduction of cross-section.

## 2.3. Concluding Remark

Based on our *in-situ* cryogenic micro-tensile tests, transmission electron microscopy, and DD simulations on Nb micropillars, the following conclusions are drawn from this study:

1. Two important factors which affect the failure mechanism at small scales were found to exist with respect to Temperature. First, cryogenic temperatures suppress dislocation cross-slip. This enables uninterrupted source operation (large strain bursts with the size of ~200 nm in the shear direction) and leads to large slip steps at the surface until pre-existing dislocations and sources

are annihilated (starved dislocation structure at 56 K). Second, cryogenic temperatures make dislocation nucleation difficult and crack propagation becomes preferable.

2. The small size of the samples bring the “Smaller is Stronger” effect. The lowered mobility of screw dislocations in bcc metals at cryogenic temperature recovers under high stress (over 800 MPa at 56 K) and it is enough for them to move easily. Otherwise, the large strain bursts would not have been observed at 56 and 100 K. Thus, the brittleness at small scales is not caused by the well-known mechanism, lowered mobility of screw dislocations in bcc metals at low temperatures.

3. Arrays of new straight dislocations were nucleated from the free surface after the sample was deformed and dislocation starvation occurred at 56 K. It is unlikely that they were from randomly oriented pre-existing dislocations or FIB damage, based on their arrangement and the calculation of the required stress for it to happen. On the other hand, the dense dislocation structure after deformation observed in the 298 K sample suggests that dislocation multiplication was highly active under stress.

4. The DD simulations resulted in a similar dislocation structure evolution to what was found in experiments on bcc micron-sized samples. The DD simulations reflected the different mobilities and cross-slip probabilities of dislocations between cryogenic and room temperatures and showed the dislocation density can increase or decrease under stress, depending on the temperatures.

5. The cracks observed at low Temperature tests are well-aligned with the straight slip traces, suggesting that the large slip steps at the surface worked as stress concentrators and promoted cracking after dislocation starvation.

At bulk scale, it would be difficult to observe all these results because dislocation multiplication almost always occurs. Therefore, the failure process that we discovered results from the combined effects of sample dimension (annihilation of dislocation at the free surface) and temperature (suppression of cross-slip) on the evolution of dislocation structures. Note that the low temperature failure process observed in this study could occur in other metal systems where dislocation starvation occurs. Several experimental studies showed the brittle tensile failure in dislocation-free Cu, Ni, and Au nanowires at room temperature [56,61-63]. Brittle failure could be even more favorable at low temperatures because dislocation nucleation becomes more difficult. Thus, micron-sized metals, which exhibit dislocation starvation, are likely to undergo brittle fracture at low temperature. At a dislocation-starved state, if the temperature is sufficiently low enough to suppress dislocation nucleation and a crack can be developed at a stress concentrator, the brittle failure can occur immediately. This failure process could be seen even more easily in high Peierls barrier bcc metals, such as tungsten or molybdenum, where it is much more difficult for dislocation nucleation to occur at low temperature. Therefore, the results in this study provide an important insight in fundamental understanding of failure process in metals at the micrometer scale and at low temperature.

## 2.4. Methodology

### *Fabrication of micro-tensile specimens*

The [001] micro-tensile specimens were fabricated out of single-crystalline [001] Nb with a 10 mm diameter and 2 mm thickness (Princeton Scientific, inc.) using focused-ion beam (FIB) milling (Helios Plasma FIB Dual Beam, Strata 400S and Helios 460F1 Dual Beam, Thermo Fisher Scientific, USA). The FIB machining started with shaping relatively large plate-

like samples with a Plasma FIB. The large square plates were milled down to the target dimension of the micro-tensile specimen using $Ga^+$ FIB. Typical tensile testing samples are shown in FIG. 1. The beam current was decreased systematically down to 10 pA of the final milling stage to minimize the FIB damage on the sample surface. The micro-tensile specimens have a square cross-section with a thickness of ~2.5μm and the gauge lengths of 15 ~ 19 μm along the [0 0 1]-direction.

*In-situ micro-tensile test*

The uni-axial tensile tests were performed at a constant nominal displacement rate of 10 nm/s utilizing a NanoFlip™ (KLA, TN, USA) with a custom-fabricated tension grip, which gives a strain rate of 5.3 ~ 6.6 x $10^{-4}$ /s throughout the tests. All experiments were conducted under ultra-high vacuum condition (< $10^{-4}$ Pa) in a field-emission gun JEOL 6335F SEM (JEOL, Japan). After each micro-tensile test, the fracture surface was characterized using SEM immersion mode (Helios 460F1 Dual Beam, Thermo Fisher Scientific, USA) to image the fracture surface and the slip bands. TEM (Talos F200X, Thermo Fisher Scientific, USA) analysis was carried out to characterize the evolution of dislocation structure at 56K and 298K.

Temperatures between 298K and 56K were obtained using liquid He (LHe) and a customized Janis cryostat system (Janis Research Company, MA, USA). Even though the cold finger reaches ~4K, cold loss occurs due to heat transfer through the sample stage and radiation emitted in the SEM chamber environment. We used a high-density polyethylene sample stage due to its excellent thermal insulation capability. During the cryogenic test, the thermal drift is effectively minimized by equilibrating the tip temperature with the sample temperature. The flat

punch tip maintains contact to the cold sample surface for more than 30 minutes. We monitored the change in displacement under a constant load condition and waited until the temperature change of the tip falls into a steady state. Then, the tip is immediately translated to a dog-bone sample, and the tensile test is performed. Thermal drift measurements after each test show that the thermal drift is always below 0.5 nm/s, which ensures a minimal change in temperature during a micro-tensile test. The detailed description of cryogenic system is available elsewhere [27].

*Dislocation Dynamics Simulation*

Dislocation dynamics simulations were performed using a modified version of ParaDiS (Parallel Dislocation Simulator, Lawrence Livermore National Laboratory, CA, USA) [64] Accommodating experimental conditions, the cylinder geometry is considered with satisfying traction free boundary conditions using the spectral method [65]. At the submicron scale, the mechanical behavior can be strongly affected by the initial microstructure. To start the loading step, we create an initial microstructure of randomly distributed pure screw dislocations, following the atomistic modeling results where a random dislocation tends to rotate into a screw orientation to reduce their energy [44], when placed in a submicron sample. For both temperatures, the initial dislocation density was around $2\times10^{12}$ $m^{-2}$, and 5 independent simulations were performed under the same conditions to obtain reasonable statistics.

To parallel quasi-static loading seen in the experiment, our DD model implements stress-controlled loading via a cut-off plastic strain rate method [17,66,67], with which, results of our DD simulations are reasonably insensitive to the loading rate. The applied loading axis was in the

direction of [001] crystal orientation. Slip was only allowed to occur on the BCC major slip system of <111>/{110} for the simplicity of simulation. Periodic boundary conditions are imposed along the cylinder axis to mimic the long cylinder.

## 2.5. References


1. J.-M. Stauffer, B. Dutoit, and B. Arbab: Standard MEMS sensor technologies for harsh environment. (2006).

2. J. R. Rice: Dislocation nucleation from a crack tip: an analysis based on the Peierls concept. *Journal of the Mechanics and Physics of Solids* **40**(2), 239 (1992).

3. J. R. Rice and R. Thomson: Ductile versus brittle behaviour of crystals. *The Philosophical Magazine: A Journal of Theoretical Experimental and Applied Physics* **29**(1), 73 (1974).

4. P. B. Hirsch, S. G. Roberts, and J. Samuels: Dislocation mobility and crack tip plasticity at the ductile-brittle transition. *Revue de Physique Appliquée* **23**(4), 409 (1988).

5. P. B. Hirsch and S. G. Roberts: The brittle-ductile transition in silicon. *Philosophical Magazine A* **64**(1), 55 (1991).

6. T. A. Parthasarathy, S. I. Rao, D. M. Dimiduk, M. D. Uchic, and D. R. Trinkle: Contribution to size effect of yield strength from the stochastics of dislocation source lengths in finite samples. *Scripta Materialia* **56**(4), 313 (2007).

7. S.-W. Lee and W. D. Nix: Size dependence of the yield strength of fcc and bcc metallic micropillars with diameters of a few micrometers. *Philosophical Magazine* **92**(10), 1238 (2012).

8. W. D. Nix and S.-W. Lee: Micro-pillar plasticity controlled by dislocation nucleation at surfaces. *Philosophical Magazine* **91**(7–9), 1084 (2011).

9. D. M. Norfleet, D. M. Dimiduk, S. J. Polasik, M. D. Uchic, and M. J. Mills: Dislocation structures and their relationship to strength in deformed nickel microcrystals. *Acta Materialia* **56**(13), 2988 (2008).

10. A. A. Elmustafa and D. S. Stone: Nanoindentation and the indentation size effect: Kinetics of deformation and strain gradient plasticity. *Journal of the Mechanics and Physics of Solids* **51**(2), 357 (2003).

11. J. R. Greer, W. C. Oliver, and W. D. Nix: Size dependence of mechanical properties of gold at the micron scale in the absence of strain gradients. *Acta Materialia* **53**(6), 1821 (2005).

12. M. D. Uchic, D. M. Dimiduk, J. N. Florando, and W. D. Nix: Sample dimensions influence strength and crystal plasticity. *Science* **305**(5686), 986 (2004).

13. B. R. S. Rogne and C. Thaulow: Strengthening mechanisms of iron micropillars. *Philosophical Magazine* **95**(16–18), 1814 (2015).

14. P. Lin, Z. Liu, Y. Cui, and Z. Zhuang: A stochastic crystal plasticity model with size-dependent and intermittent strain bursts characteristics at micron scale. *International Journal of Solids and Structures* **69**, 267 (2015).

15. F. Mompiou, M. Legros, A. Sedlmayr, D. S. Gianola, D. Caillard, and O. Kraft: Source-based strengthening of sub-micrometer Al fibers. *Acta materialia* **60**(3), 977 (2012).

16. K. S. Ng and A. H. W. Ngan: Stochastic theory for jerky deformation in small crystal volumes with pre-existing dislocations. *Philosophical Magazine* **88**(5), 677 (2008).

17. I. Ryu, W. Cai, W. D. Nix, and H. Gao: Stochastic behaviors in plastic deformation of face-centered cubic micropillars governed by surface nucleation and truncated source operation. *Acta Materialia* **95**, 176 (2015).

18. J. R. Greer and W. D. Nix: Size dependence of mechanical properties of gold at the sub-micron scale. *Applied Physics A* **80**(8), 1625 (2005).

19. C. A. Volkert and E. T. Lilleodden: Size effects in the deformation of sub-micron Au columns. *Philosophical Magazine* **86**(33–35), 5567 (2006).

20. J. R. Greer and W. D. Nix: Nanoscale gold pillars strengthened through dislocation starvation. *Physical Review B* **73**(24), 245410 (2006).

21. W. D. Nix, J. R. Greer, G. Feng, and E. T. Lilleodden: Deformation at the nanometer and micrometer length scales: Effects of strain gradients and dislocation starvation. *Thin Solid Films* **515**(6), 3152 (2007).

22. P. Gumbsch, J. Riedle, A. Hartmaier, and H. F. Fischmeister: Controlling factors for the brittle-to-ductile transition in tungsten single crystals. *Science* **282**(5392), 1293 (1998).

23. J. Samuels and S. G. Roberts: The brittle–ductile transition in silicon. I. Experiments. *Proceedings of the Royal Society of London. A. Mathematical and Physical Sciences* **421**(1860), 1 (1989).

24. M. Elhebeary, T. Harzer, G. Dehm, and M. T. A. Saif: Time-dependent plasticity in silicon microbeams mediated by dislocation nucleation. *Proceedings of the National Academy of Sciences* **117**(29), 16864 (2020).

25. J. Ast, J. J. Schwiedrzik, J. Wehrs, D. Frey, M. N. Polyakov, J. Michler, and X. Maeder: The brittle-ductile transition of tungsten single crystals at the micro-scale. *Materials & Design* **152**, 168 (2018).

26. C. Thaulow, D. Sen, and M. J. Buehler: Atomistic study of the effect of crack tip ledges on the nucleation of dislocations in silicon single crystals at elevated temperature. *Materials Science and Engineering: A* **528**(13–14), 4357 (2011).

27. G. Song, V. Borisov, W. R. Meier, M. Xu, K. J. Dusoe, J. T. Sypek, R. Valent\'\i, P. C. Canfield, and S.-W. Lee: Ultrahigh elastically compressible and strain-engineerable intermetallic compounds under uniaxial mechanical loading. *APL Materials* **7**(6), 61104 (2019).

28. A. Farag, S. Bagheri, and H. Giessen: Towards superconducting niobium plasmonics for light detection. *Verhandlungen der Deutschen Physikalischen Gesellschaft* (2018).

29. A. I. Braginski: Superconductor electronics: status and outlook. *Journal of Superconductivity and Novel Magnetism* **32**(1), 23 (2019).

30. Z. W. Shan, R. K. Mishra, S. A. S. Asif, O. L. Warren, and A. M. Minor: Mechanical annealing and source-limited deformation in submicrometre-diameter Ni crystals. *Nature materials* **7**(2), 115 (2008).

31. C. Chisholm, H. Bei, M. B. Lowry, J. Oh, S. A. S. Asif, O. L. Warren, Z. W. Shan, E. P. George, and A. M. Minor: Dislocation starvation and exhaustion hardening in Mo alloy nanofibers. *Acta Materialia* **60**(5), 2258 (2012).

32. M. C. Li, M. Q. Jiang, G. Li, L. He, J. Sun, and F. Jiang: Ductile to brittle transition of fracture of a Zr-based bulk metallic glass: Strain rate effect. *Intermetallics* **77**, 34 (2016).

33. R. Liontas, M. Jafary-Zadeh, Q. Zeng, Y.-W. Zhang, W. L. Mao, and J. R. Greer: Substantial tensile ductility in sputtered Zr-Ni-Al nano-sized metallic glass. *Acta Materialia* **118**, 270 (2016).

34. B. D. Snartland, A. B. Hagen, and C. Thaulow: Fracture mechanical testing of single crystal notched α-iron micro-cantilevers. *Engineering Fracture Mechanics* **175**, 312 (2017).

35. B.-S. Li, T. J. Marrow, and D. E. J. Armstrong: Measuring the brittle-to-ductile transition temperature of tungsten–tantalum alloy using chevron-notched micro-cantilevers. *Scripta Materialia* **180**, 77 (2020).

36. M. S. Duesbery and R. A. Foxall: A detailed study of the deformation of high purity niobium single crystals. *Philosophical Magazine* **20**(166), 719 (1969).

37. Y. Kim, D. Jang, and J. R. Greer: Insights into deformation behavior and microstructure evolution in Nb single crystalline nano-pillars under uniaxial tension and compression. *Scr. Mater* **61**(3), 300 (2009).

38. D. Kiener, C. Motz, M. Rester, M. Jenko, and G. Dehm: FIB damage of Cu and possible consequences for miniaturized mechanical tests. *Materials Science and Engineering: A* **459**(1–2), 262 (2007).

39. S.-W. Lee and W. D. Nix: Size dependence of the yield strength of fcc and bcc metallic micropillars with diameters of a few micrometers. *Philosophical Magazine* **92**(10), 1238 (2012).

40. J. R. Greer, C. R. Weinberger, and W. Cai: Comparing the strength of fcc and bcc sub-micrometer pillars: Compression experiments and dislocation dynamics simulations. *Materials Science and Engineering: A* **493**(1–2), 21 (2008).

41. H. M. Zbib and E. C. Aifantis: Size effects and length scales in gradient plasticity and dislocation dynamics. *Scripta materialia* **48**(2), 155 (2003).

42. S.-W. Lee, A. T. Jennings, and J. R. Greer: Emergence of enhanced strengths and Bauschinger effect in conformally passivated copper nanopillars as revealed by dislocation dynamics. *Acta materialia* **61**(6), 1872 (2013).

43. W. Cai, V. v Bulatov, T. G. Peirce, M. Hiratani, M. Rhee, M. Bartelt, and M. Tang: (2004).

44. I. Ryu, W. D. Nix, and W. Cai: Plasticity of bcc micropillars controlled by competition between dislocation multiplication and depletion. *Acta materialia* **61**(9), 3233 (2013).

45. W. Cai and V. v Bulatov: Mobility laws in dislocation dynamics simulations. *Materials Science and Engineering: A* **387**, 277 (2004).

46. W. Cai, V. v Bulatov, J. Chang, J. Li, and S. Yip: Dislocation core effects on mobility. *Dislocations in solids* **12**, 1 (2004).

47. D. Caillard: Kinetics of dislocations in pure Fe. Part I. In situ straining experiments at room temperature. *Acta Materialia* **58**(9), 3493 (2010).

48. G. Po, Y. Cui, D. Rivera, D. Cereceda, T. D. Swinburne, J. Marian, and N. Ghoniem: A phenomenological dislocation mobility law for bcc metals. *Acta Materialia* **119**, 123 (2016).

49. A. S. Schneider, C. P. Frick, E. Arzt, W. J. Clegg, and S. Korte: Influence of test temperature on the size effect in molybdenum small-scale compression pillars. *Philosophical magazine letters* **93**(6), 331 (2013).

50. A. S. Schneider, D. Kaufmann, B. G. Clark, C. P. Frick, P. A. Gruber, R. Mönig, O. Kraft, and E. Arzt: Correlation between critical temperature and strength of small-scale bcc pillars. *Physical review letters* **103**(10), 105501 (2009).

51. C. R. Weinberger and W. Cai: Surface-controlled dislocation multiplication in metal micropillars. *Proceedings of the National Academy of Sciences* **105**(38), 14304 (2008).

52. S.-W. Lee, Y. Cheng, I. Ryu, and J. R. Greer: Cold-temperature deformation of nano-sized tungsten and niobium as revealed by in-situ nano-mechanical experiments. *Science China Technological Sciences* **57**(4), 652 (2014).

53. G. Song and S.-W. Lee: Effects of temperature on surface-controlled dislocation multiplication in body-centered-cubic metal nanowires. *Computational Materials Science* **168** (2019).

54. P. Kneisel, G. Ciovati, P. Dhakal, K. Saito, W. Singer, X. Singer, and G. R. Myneni: Review of ingot niobium as a material for superconducting radiofrequency accelerating cavities. *Nuclear Instruments and Methods in Physics Research Section A: Accelerators, Spectrometers, Detectors and Associated Equipment* **774**, 133 (2015).

55. J.-Y. Kim, D. Jang, and J. R. Greer: Tensile and compressive behavior of tungsten, molybdenum, tantalum and niobium at the nanoscale. *Acta Materialia* **58**(7), 2355 (2010).

56. G. Richter, K. Hillerich, D. S. Gianola, R. Monig, O. Kraft, and C. A. Volkert: Ultrahigh strength single crystalline nanowhiskers grown by physical vapor deposition. *Nano Letters* **9**(8), 3048 (2009).

57. H. Bei, S. Shim, E. P. George, M. K. Miller, E. G. Herbert, and G. M. Pharr: Compressive strengths of molybdenum alloy micro-pillars prepared using a new technique. *Scripta Materialia* **57**(5), 397 (2007).

58. T. J. Flanagan, O. Kovalenko, E. Rabkin, and S.-W. Lee: The effect of defects on strength of gold microparticles. *Scripta Materialia* **171**, 83 (2019).

59. S. Shim, H. Bei, M. K. Miller, G. M. Pharr, and E. P. George: Effects of focused ion beam milling on the compressive behavior of directionally solidified micropillars and the nanoindentation response of an electropolished surface. *Acta Materialia* **57**(2), 503 (2009).

60. A. Lupinacci, J. Kacher, A. Eilenberg, A. A. Shapiro, P. Hosemann, and A. M. Minor: Cryogenic in situ microcompression testing of Sn. *Acta materialia* **78**, 56 (2014).

61. C. Peng, Y. Ganesan, Y. Lu, and J. Lou: Size dependent mechanical properties of single crystalline nickel nanowires. *Journal of Applied Physics* **111**(6), 63524 (2012).

62. Y. Lu, J. Song, J. Y. Huang, and J. Lou: Fracture of sub-20nm ultrathin gold nanowires. *Advanced Functional Materials* **21**(20), 3982 (2011).

63. J. Wang, F. Sansoz, J. Huang, Y. Liu, S. Sun, Z. Zhang, and S. X. Mao: Near-ideal theoretical strength in gold nanowires containing angstrom scale twins. *Nature communications* **4**(1), 1 (2013).

64. A. Arsenlis, W. Cai, M. Tang, M. Rhee, T. Oppelstrup, G. Hommes, T. G. Pierce, and V. v Bulatov: Enabling strain hardening simulations with dislocation dynamics. *Modelling and Simulation in Materials Science and Engineering* **15**(6), 553 (2007).

65. C. R. Weinberger and W. Cai: Computing image stress in an elastic cylinder. *Journal of the Mechanics and Physics of Solids* **55**(10), 2027 (2007).

66. I. Ryu, W. Cai, W. D. Nix, and H. Gao: Anisotropic size-dependent plasticity in face-centered cubic micropillars under torsion. *JOM* **68**(1), 253 (2016).

67. J. A. El-Awady, M. Wen, and N. M. Ghoniem: The role of the weakest-link mechanism in controlling the plasticity of micropillars. *Journal of the Mechanics and Physics of Solids* **57**(1), 32 (2009).

# Chapter 3. Uniaxial compression of single crystalline bcc nanopillars at various temperatures: Effect of temperature on Surface-controlled dislocation multiplication under constant compression

(Reproduced from "Song, G, et al., *Computational Materials Science* 168 (2019): 172-179", with the permission of Elsevier)

## 3.1. Introduction

Mechanical properties of metals are mostly controlled by the motion of dislocations, which is a line imperfection in crystalline solids. Thus, the understanding of dislocation behavior is critical to develop structurally robust metallic components in devices [1, 2]. Recently, nano-/micro-electro-mechanical systems (NEMS/MEMS) have been developed to produce small-scale sensors and actuators. It is necessary to understand how dislocations behave in the nanoscale volume in order to make mechanically-reliable miniaturized systems [3-5]. For the last two decades, nanomechanical testing techniques have been extensively developed to study dislocation plasticity in small metals such as thin films, micropillars, nanowires, and nanoparticles [6-12]. These works have demonstrated the presence of strong size effects on mechanical properties when a sample dimension reaches microstructural length scales. In the case of a single-crystalline metal, the interaction between dislocations and free surface leads to size-affected strength, scale-free intermittency, dislocation starvation, Schmidt's law breakdown, and so forth [13-15].

Recent experimental studies demonstrated that body-centered-cubic (bcc) metallic nanopillars exhibit significant dislocation multiplication while face-centered-cubic (fcc) metallic nanopillars do not. Bei *et al*. found that dislocation-free bcc Mo-alloy single-crystal nanopillars

are catastrophically strain-softened, presumably by nucleation of dislocations followed by their extensive multiplication [16]. Chisholm *et al.* observed extremely high dislocation density right after yielding in bcc Mo-alloy nanofibers through *in-situ* transmission electron microscope (TEM) nanomechanical tests [17]. Furthermore, Brinckmann *et al.* showed that the stress-strain curves of bcc nanopillars are usually much smoother than those of fcc nanopillars [18]. Their post-mortem TEM analysis revealed higher dislocation density in bcc nanopillars while fcc nanopillars are nearly dislocation-free even after applying significant plastic deformation. All this experimental evidence indicates that bcc metals are able to induce significant dislocation multiplication in the nanoscale volume.

To clarify the mechanism of dislocation multiplication which occurs preferentially in bcc metal nanopillars, Weinberger *et al.* performed both dislocation dynamics (DD) and molecular dynamics (MD) simulations on bcc molybdenum nanowires containing a single screw dislocation [19]. It was discovered that a screw dislocation can self-multiply through cross-slips near the free surface, which is followed by the formation and operation of dynamic dislocation sources. Strong image stresses force both ends of the screw dislocation to cross-slip from {1 1 0} to {1 1 2} planes, creating two dynamic single arm dislocation sources joined at a mobile pinning point. If the applied stress is higher than a critical stress, these two dynamic dislocation sources can produce new dislocations. Weinberger *et al.* termed this phenomenon surface-controlled dislocation multiplication (SCDM) [19]. Their computational studies showed that the critical stress of SCDM is a strong function of pillar diameter. They also confirmed that SCDM cannot be seen easily in fcc nanowires, particularly for low stacking fault energy materials such as gold, because the wide width of dislocation core does not permit a cross-slip at the free surface, which is a prerequisite process for SCDM.

Nowadays, studies on small-scale mechanical properties of materials under harsh environments have drawn increased attention due to the necessity to develop micro-/nano-scale devices working in different chemical and thermal environments [20, 21]. MEMS/NEMSs which operate in the presence of high temperature, corrosive media and/or high radiation can reduce weight, improve machine reliability, and reduce cost in strategic market sectors such as automotive, avionics, oil well logging, nuclear power, and space exploration [22-24]. In order to produce a mechanically-reliable small-scale device used in various environments, it is important to understand how environmental conditions influence dislocation behaviors at the micro-/nano-meter length scales. Note that the motion of dislocations in bcc metals is strongly affected by temperature [25]. Particularly for a screw dislocation, the double-kink mechanism, which is a thermally-activated process, controls its mobility. Furthermore, cross-slip of screw dislocations is usually regarded as a thermally-activated process. At an elevated temperature, strong thermal vibrations would induce cross-slip more frequently and could lead to different evolutions of the dislocation structure. Therefore, SCDM of a screw dislocation in bcc nanowires, which requires cross-slip at the free surface, could be significantly sensitive to temperature.

In this work, therefore, we performed atomistic simulations on two representative bcc metals, molybdenum (Mo) and niobium (Nb) nanowires containing a single screw dislocation to study the effects of temperature on SCDM. We developed the constant uniaxial stress method and characterized the critical shear stress ($\tau_{[111](1\bar{2}1)}$) of SCDM as a function of temperature. Both systems showed three distinct regimes of the critical shear stress of SCDM with respect to temperature, and each regime can be characterized based on the corresponding dislocation behavior; (1) lattice resistance dominant; (2) segmentation dominant, and (3) steady-state segmentation. We will discuss the presence of these three regimes in terms of the temperature-

dependence of lattice resistance and the dynamics of dislocation segmentation in the nano-scale volume. Note that our simulation results would not be applied only to Nb and Mo but can also be applied to other bcc metals. Thus, our results will provide a mechanistic description of the dislocation multiplication process of a screw dislocation in bcc metals at small length scales at various temperatures.

## 3.2. Computational method

### 3.2.1. Basic simulation set-up

SCDM in bcc metal nanowires was systematically studied as a function of material and temperature. We chose bcc Nb and Mo due to their large difference in Peierls barrier (Nb: 70 MPa and Mo: 629 MPa [26] measured by bulk-scale experiments), which influences the mobility of screw dislocations. The range of temperature was appropriately chosen (10~400K for Nb and 10~800K for Mo) to study the transitions of SCDM processes. We did not study SCDM at too high temperatures because significant thermally-activated events make the analysis of dislocation structure too difficult. Also, we do not discuss size effects in this study and focus only on how the temperature change influences SCDM processes at a given nanometer scale. Size effects will be presented in a separate publication.

The MD simulations were conducted using 'Large-scale Atomic/Molecular Massively Parallel Simulator' (LAMMPS) [27] under NσT ensemble time integration via Nose/Hoover method with Finnis-Sinclair (FS) potential for Mo [28] and Embedded-atom method (EAM) potential for Nb [29]. These interatomic potentials have been extensively used for various simulations, and their transferability has been demonstrated successfully. Both interatomic

potentials were used reliably in MD simulations at temperatures and loading conditions used in our work [19, 30, 31]. The stresses were computed by using the constant NPT time integration via Nose/Hoover. In fact, the LAMMPS code provides the macroscopic stress tensor for the simulation cell volume. To obtain the stress tensor for our pillar, the LAMMPS stress tensor outputs must be scaled by the ratio of the pillar volume to the cell volume. This ratio is exactly the same with the ratio of the cross-sectional area of pillar to the top (or bottom) area of simulation cell because the height is identical. To calculate the cross-sectional area of pillar, the diameter (D) of pillar was estimated by measuring the distance between most distantly separated two atoms on the top surface, and then, the cross-sectional area of pillar was obtained by $\pi D^2/4$. The same method was also used to compute the stress in silicon nanowire in the work done by Kang and Cai [32], and the description of stress estimation is available in their paper. The diameter and height of the nanowires were ~14 nm and ~31 nm, respectively, for all simulations (**Figure 3.1(a)**). The number of atoms for Mo and Nb were 310,600 and 282,600, respectively. We used the periodic boundary condition along x, y and z directions, but because the empty space is available around a pillar, the periodic images along x and y directions do not affect the pillar in the simulation cell. The nanowires that have a pure screw dislocation with **b**=a/2[1 1 1] on the $(0\ 1\ \bar{1})$ plane were constructed using MD++ [33]. The initial position of the screw dislocation was carefully chosen (1.6 nm from the center of nanowire) to provide enough time for dislocation multiplication under a reasonable stress value (**Figure 3.1(b)**). We kept the same initial position of the screw dislocation for all simulations. We did not try to start from a dislocation-free system as usually considered to study the mechanical behavior of nanowires because it is challenging to control the behavior of dislocations due to the stochastic nature of thermally-activated process of dislocation nucleation [34, 35]. In this case, multiple dislocations

are often nucleated together at the first yield point. These dislocations sometimes interact with each other, and dislocation multiplication could result from dislocation interaction in addition to surface-induced cross-slip. They are also nucleated at different locations and at different stress levels depending on the initial atomic velocity distribution. Furthermore, the dislocation nucleation stress, which is usually close to the theoretical strength, is always higher than the critical stress of surface-controlled dislocation multiplication in our study. Once a screw dislocation is nucleated, it will always self-multiply under load-control, or the load will drop significantly under displacement control. Thus, it is difficult to study the effect of stress on surface-controlled dislocation multiplication when a simulation starts from the dislocation-free state. Therefore, we preferred to use a straight screw dislocation as an initial condition, and it is much easier to control the applied stress systematically.

At a given temperature, a wide range of constant compressive stress ($\sigma_{zz}$) was applied along the [0 0 1]-direction until we observe SCDM. Then, the critical axial stress of SCDM was taken as the lowest stress, at which a dislocation self-multiplies. In our analysis, we used the resolved shear stress of a [1 1 1](1 $\bar{2}$ 1) slip system ($\tau_{[111](1\bar{2}1)}$) because cross-slipped dislocations usually stay in [1 1 1](1 $\bar{2}$ 1) and [1 1 1]($\bar{2}$ 1 1) slip systems, both of which have the same Schmid factor, 0.236 under the [0 0 1] loading. Note that at an elevated temperature, a single dislocation can sometimes reside on multiple slip planes due to localized cross-slip events, but we still used $\tau_{[111](1\bar{2}1)}$ for the consistent comparison. Dislocation structures were visualized based on the Dislocation Extraction Algorithm (DXA). Surface atoms and dislocation atoms were visualized by Ovito [36]

Additionally, to evaluate the effects of periodic image dislocations by changing the z-dimension of simulation cell, we also conducted the simulation with a nanowire three times

longer in z-direction. However, we did not find any significant differences. This result implies that the effect of periodic image dislocations is less significant in determination of critical stress, and the applied stress on the dislocation in a simulation cell would control the dislocation multiplication dominantly.

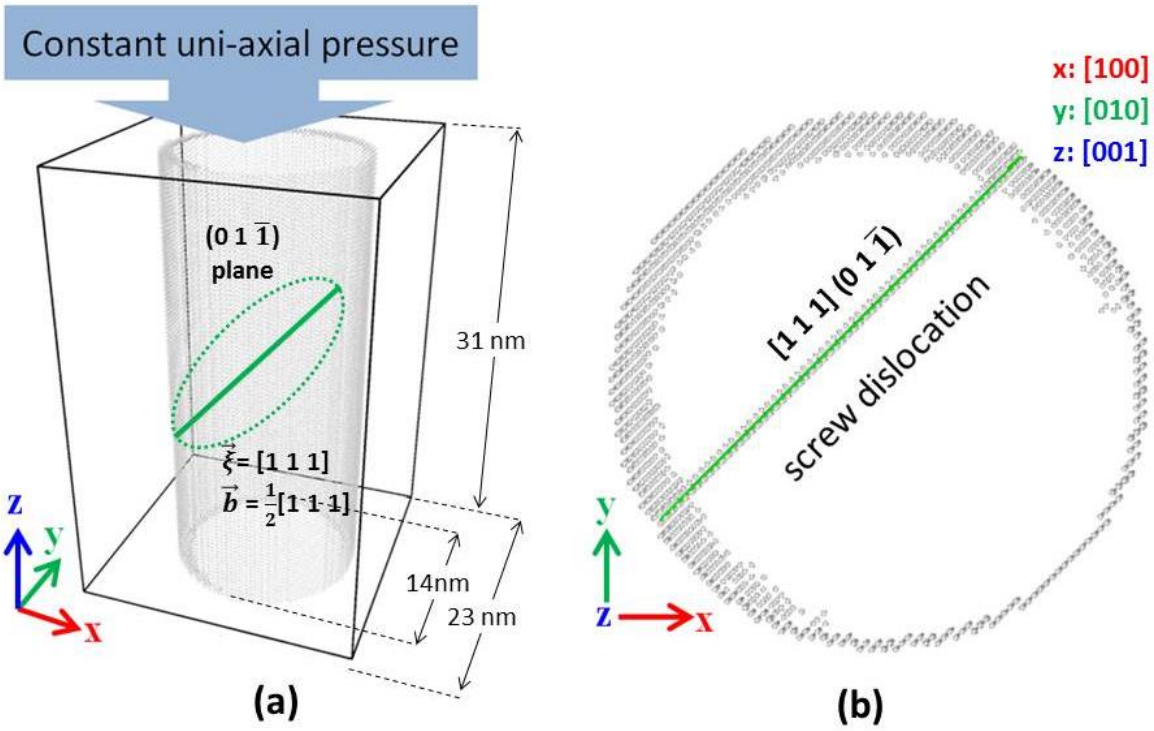


**Figure 3.1. Initial atomistic simulation set-up (a) A nanowire containing a dislocation in a simulation box with periodic boundary condition in 3 dimensions; (b) The top view of a screw dislocation in a Nb nanowire.**

### 3.2.2. Constant stress simulation

In this study, we do not use the low strain rate simulation. If the low strain rate is used, it is almost impossible to study the effect of stress because the applied stress changes over time and a

dislocation structure would already change significantly before a target stress is reached. Our simulation aimed to observe how a screw dislocation behaves under a constant stress directly from the beginning of the simulation. In this way, it is possible to avoid any complications caused by the evolution of dislocation structure that occurs until a stress reaches the target stress.

To confirm the importance of constant stress application from the beginning of the simulation, we first tried the conventional method available in the default setting of LAMMPS. We increased the applied stress rapidly to the target stress and let the system stabilize toward the target stress state ($\sigma_{zz} \neq 0$ and $\sigma_{xx}=\sigma_{yy}=0$) as quickly as possible. We noted that $\sigma_{zz}$ is easily stabilized, but the other two axial stresses ($\sigma_{xx}$ and $\sigma_{yy}$) are not stabilized quickly. The sudden application of $\sigma_{zz}$ at the beginning always induced significant elastic waves along the transverse directions. For instance, the initial application of $\sigma_{zz}$ = 17.6 GPa produces a large transverse stress wave with the amplitude of $\sigma_{xx}$ ($\sigma_{yy}$) = 5 GPa, which is nearly ~28% of $\sigma_{zz}$ (**Figure 3.2**). These elastic fluctuations are diminished relatively slowly, thus they could significantly affect the evolution of the dislocation structure. Thus, to perform a reliable constant stress simulation, the transverse elastic fluctuation must be suppressed from the beginning of the simulation.

In order to minimize the transverse elastic fluctuations, we imposed axial pre-strains ($\varepsilon_{xx}$, $\varepsilon_{yy}$, and $\varepsilon_{zz}$). First, we estimated the required pre-strain values based on the anisotropic elasticity theory. Then, all atoms were displaced according to the calculated pre-strains. However, the elasticity calculation is not the optimized solution at every temperature used in this study. Thus, we systematically increased or decreased the lateral dimension until the transverse elastic fluctuation was almost completely suppressed. **Figure 3.2** shows the large difference in stress amplitude when the pillar dimension is pre-adjusted or not. Therefore, it is important to pre-adjust the dimensions of the nanowire to perform constant stress simulations properly. Within each

simulation the amplitude of the transverse elastic waves was less than 0.5 GPa; this ensures that the effect on dislocation behavior is negligible.

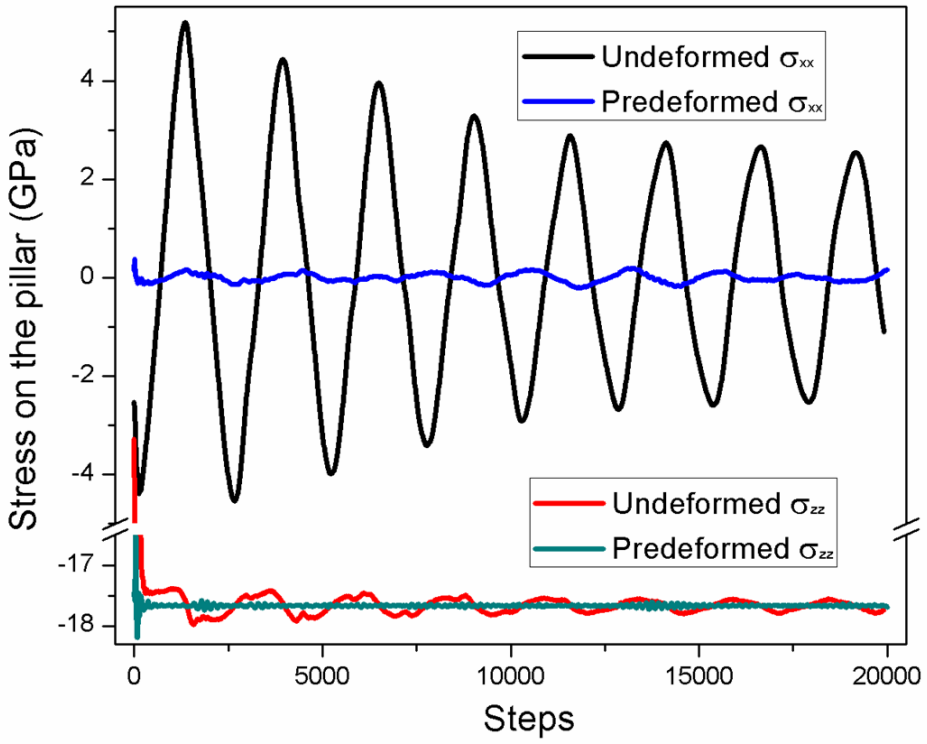


**Figure 3.2. The effect of pre-strain on the transverse stresses. The application of pre-strain successfully suppresses the transverse elastic waves from the beginning of the simulation.**

## 3.3. Results and Discussion

As described in Weinberger *et al.*'s work, if the applied stress is higher than the critical shear stress, a screw dislocation becomes the dynamic dislocation source, which produces new dislocations (**Figure 3.3**) [19]. In our study, following Weinberger *et al.*'s definition, the critical shear stress of SCDM was selected only when the isolated secondary dislocation is successfully formed and glides. Then, we obtained the critical shear stress leading to SCDM as a function of

temperature. We confirmed that our room temperature data of Mo nanowires agrees with Weinberger *et al.*'s results based on their scaling relation (our nanowire is smaller than their smallest nanowires) [19]. This result ensures that our simulation was correctly set up. In this study, when different temperatures were considered, we found that there are three distinct regimes of critical shear stress of SCDM with respect to temperature in both Nb and Mo nanowires (**Figure 3.4**). Our simulation data show a relatively good agreement with the experimentally measured Peierls stresses that we cited in terms of the difference in magnitude of stress levels (**Figure 3.4**); the level of critical stresses for Mo is a few factors higher than that of Nb in general. This large difference of stress level should result from the large difference in Peierls stress (or lattice resistance). Therefore, the interatomic potentials used in our work reflects the large difference in Peierls stress between Mo and Nb relatively well. The details of each regime will be discussed in the following sub-sections.

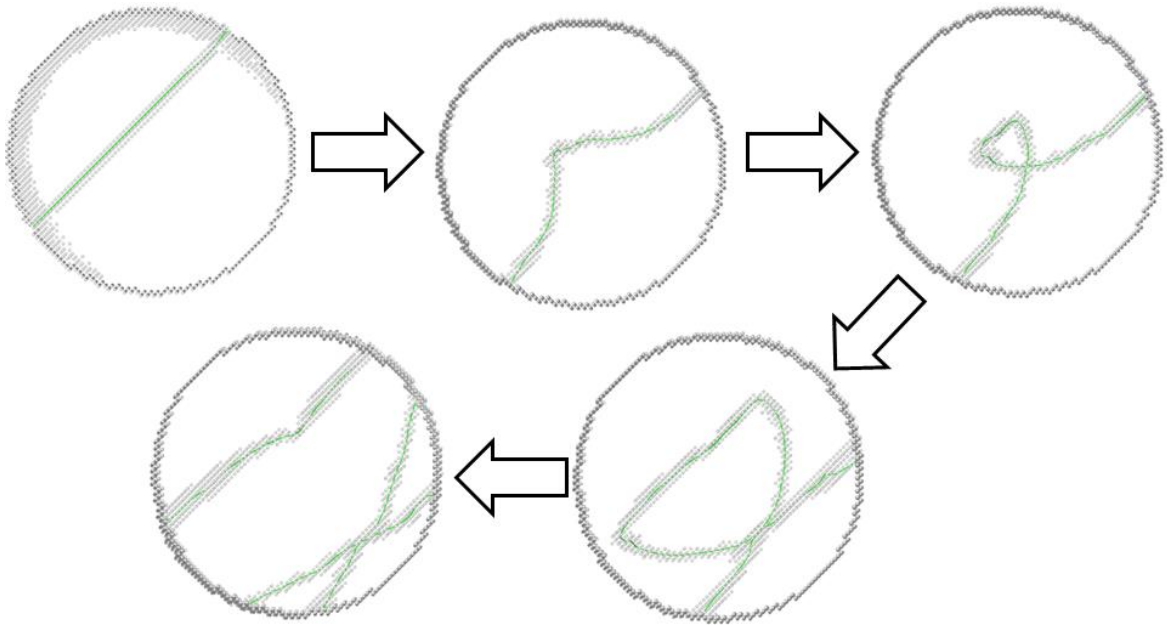

**Figure 3.3. Surface-controlled dislocation multiplication in a bcc Mo nanowire (T=10K, σzz=7.5 GPa). The multiplication process is consistent with Weinberger et al.'s results [19].**

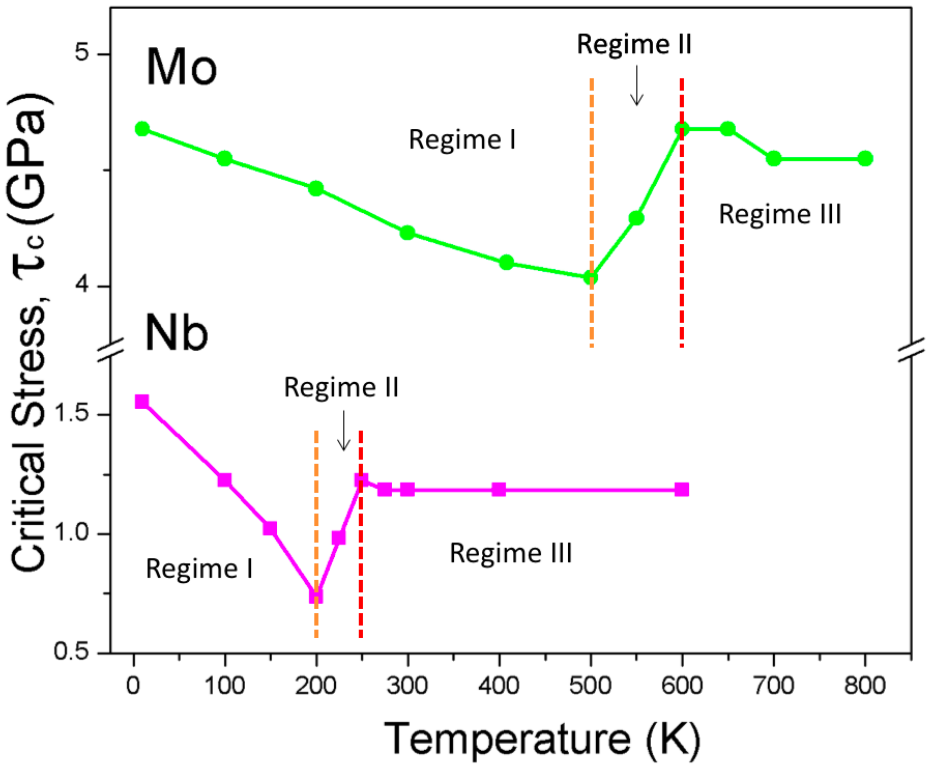


**Figure 3.4. Critical resolved shear stress ($\tau_{[111](1\bar{2}1)}$) as a function of temperature. There are three distinct regimes of critical shear stress of SCDM with temperature for both Nb and Mo nanowires. In Regime I, the critical shear stress decreases with temperature for both Nb and Mo nanowires. In Regime I, the critical shear stress decreases with temperature, but in Regime II, the critical shear stress increases abruptly. After the small peak value, the critical shear stress becomes nearly constant in Regime III**

### 3.3.1. Regime I: Lattice resistance control

In Regime I, the SCDM behavior resembles the behavior observed in Weinberger *et al.*'s Mo nanowire simulations done at room temperature, which belongs to Regime I according to our

results (**Figure 3.4**). Cross-slip occurs at both ends of the dislocation due to the image stresses, and the screw dislocation moves onto [1 1 1](1 $\bar{2}$ 1) and [1 1 1]($\bar{2}$ 1 1) slip systems. Then, the cusp is formed in the middle of the dislocation. If the applied stress is higher than a critical shear stress, the dislocation with the cusp produces the secondary dislocation (**Figure 3.3**). We noticed that in Regime I, the critical shear stress ($\tau_{[111](1\bar{2}1)}$) of SCDM decreases monotonically with temperature for both Nb and Mo nanowires (**Figure 3.4**). The critical shear stress of Mo nanowires is ~4.6 GPa at 10K and ~4.0 GPa at 500K, whereas that of Nb nanowires is ~1.6 GPa at 10K and is ~0.7 GPa at 200K.

The mobility of screw dislocations in bcc metals is usually a strong function of temperature and is determined by the nucleation and propagation of double kinks. The double-kink mechanism is a thermally-activated process [37, 38]. At higher temperatures, thus, the nucleation rate of double kinks becomes higher, leading to the higher mobility of a screw dislocation at a given stress. At early stages of simulations, we carefully monitored the motion of dislocation and confirmed that it moves faster at a higher temperature. For instance, at ~1.23 GPa, a screw dislocation in Nb nanowire barely moves at 10 K but moves much farther at 200 K (**Figure 3.5**). In case of Mo, the result looked similar (not shown here). At a given stress, therefore, a dislocation can move forward more easily at higher temperatures, leading to the lower critical shear stress of SCDM in Regime I.

The mobility of dislocation is usually related to the magnitude of intrinsic lattice resistance, which is the critical shear stress required for the motion of a straight and infinitely-long single dislocation without elastic interaction with other dislocations. Usually, the higher the intrinsic lattice resistance is, the lower the mobility of dislocation is. At any given temperature, the intrinsic lattice resistance of Mo is known to be higher than that of Nb [7, 26]. Thus, the

higher critical shear stresses for SCDM in Mo nanowires within Regime I would result partly from its higher intrinsic lattice resistance (**Figure 3.4**) (The contribution of dislocation line tension will be discussed in Section 3.3.4.).

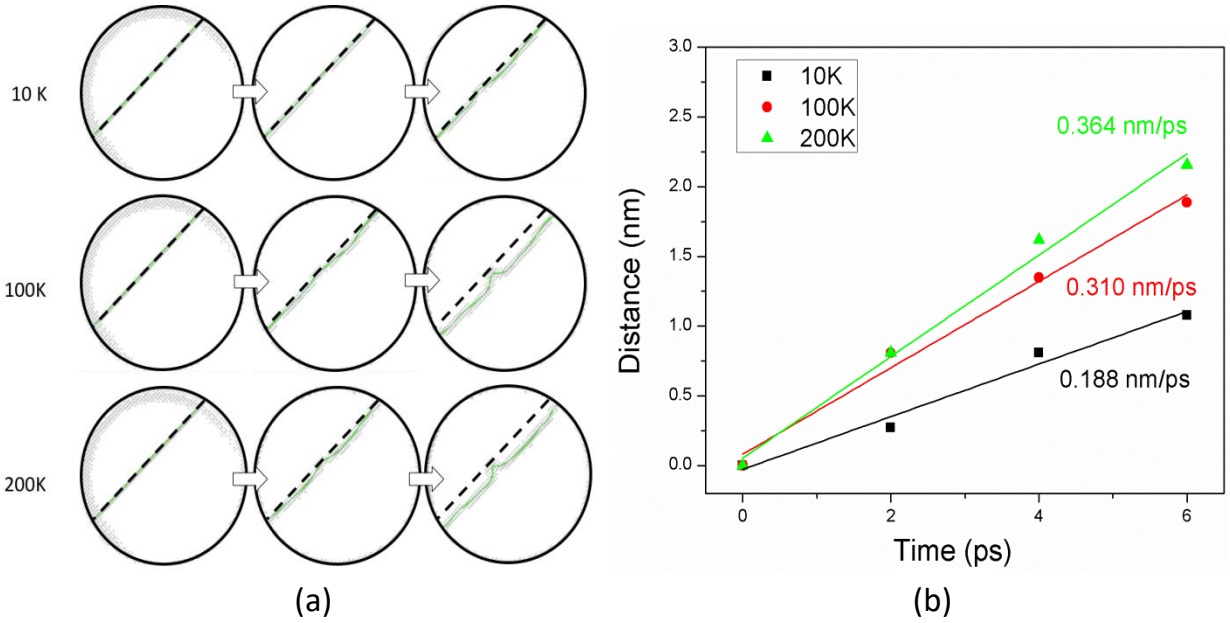


**Figure 3.5. Temperature-dependent dislocation motion in Regime I. (a) Dislocation motion at a given stress/time but at different temperatures in Nb nanowire at 0, 2, 4 picoseconds. Dotted line indicates the initial position of dislocation. (b) The velocities of dislocations at different temperatures.**

### 3.3.2. Regime II: Dynamic cross-slip dominant

As the temperature continues to rise from Regime I, the critical shear stress of SCDM stops decreasing and begins to increase abruptly (**Figure 3.4**). The critical shear stress of Mo nanowires increases up to 4.7 GPa for the shorter range of temperature from 500K to 600K. The critical shear stress of Nb nanowires increases up to 1.2 GPa over 50K range from 200 to 250K.

These results are not consistent with the generally accepted idea of intrinsic lattice resistance discussed in Section 3.3.1. Therefore, there might be the operation of another thermally-activated dislocation mechanism.

We carefully compared the evolution of dislocation structures in Regime II with that in Regime I. The evolution of the dislocation structure in Nb nanowires was monitored at the constant stress of 1.14 GPa and at 250 K (Regime II, no multiplication condition). At 250 K, we found that additional cross-slip occurs at the free surface, and the dislocation suddenly consists of three segments (**Figure 3.6**). Here, a segment means a section of dislocation that resides on the slip plane different from that of neighboring segments. We made a thin slice of sample, which is parallel to a slip plane to monitor the trajectory of the dislocation segments as a function of time and identified the slip plane of each segment precisely. For instance, in the case of Nb nanowires, a dislocation stays on the $(\bar{2}\ 1\ 1)$, $(1\ 1\ \bar{2})$, and $(1\ \bar{2}\ 1)$ planes in the middle of simulation. Note that the $(1\ 1\ \bar{2})$ slip plane was not observed in Regime I. The cross-slip events in Regime I were driven only by the image stress and was a completely athermal process (In other words, it can occur even at 0 K.) [19], but the additional cross-slip in Regime II could be a thermal process. Note that cross-slip is usually regarded as a thermal activation process. This thermally-activated cross-slip is less likely to occur at a low temperature (Regime I) but could occur easily at higher temperatures (Regime II). In Regime II, therefore, the thermally-activated cross-slip could lead to the segmentation of dislocation.

If the temperature becomes higher, a thermal cross-slip event would occur more vibrantly, and the dislocation would be segmented more easily. The operation of Frank-Read type dislocation source is inversely proportional to the length of the dislocation source, which would correspond to the length of longest segment in our case. The critical shear stress of Frank-

Read type dislocation source ($\tau_{F-R}$) is usually expressed by $\mu b/L$, where $\mu$ is the shear modulus, $b$ the magnitude of Burgers vector, and $L$ the source length. Obviously, the source length ($L$) becomes abruptly shorter once a dislocation is segmented and therefore the source operation stress ($\tau_{F-R}$) could increase abruptly, too. Although the intrinsic lattice resistance keeps decreasing as the temperature increases, the dislocation segmentation would be much more dominant in the determination of the critical shear stress of SCDM in Regime II. This explains the sudden change in critical shear stress Regime II within the narrow temperature range.

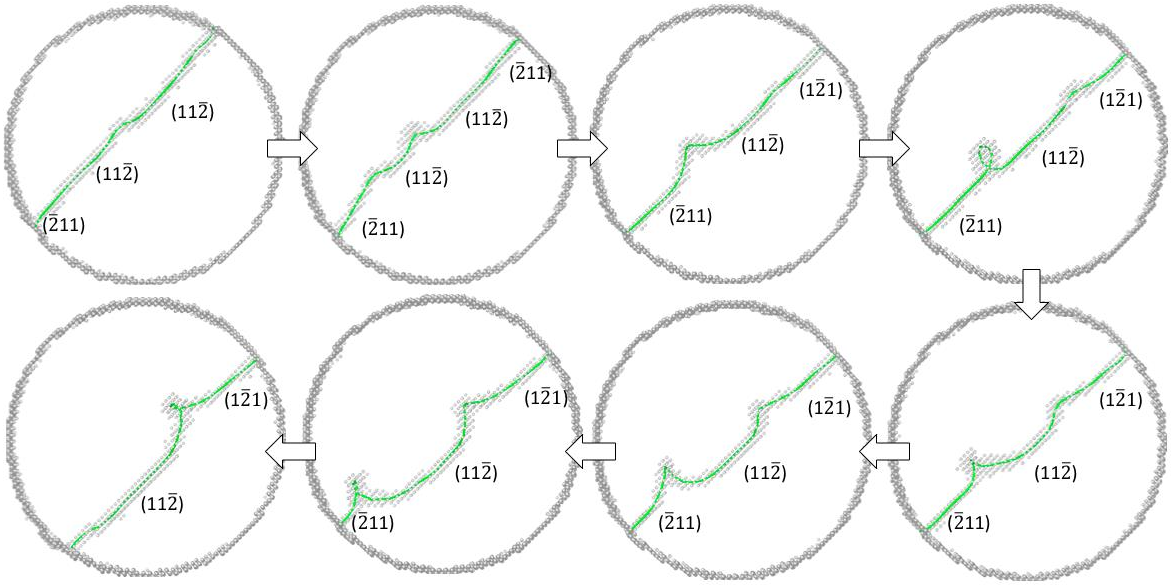


**Figure 3.6. Evolution of dislocation structures in Regime II. Dislocation segmentation in Nb nanowire at τ=1.14 GPa and 250 K. Note that three dislocation segments are available in the middle of the simulation.**

The similar self-pinning behavior was observed in Marian *et al.*'s MD simulation on a screw dislocation in bcc iron [39]. This work demonstrated that a line structure of dislocation becomes rough due to dynamic cross-slip events, leading to the more difficult motion of

dislocation, called dislocation roughening. Dislocation roughening is the transition from a smooth line of dislocation moving via formation and migration of atomic-sized kinks to a rugged line moving in a jerky way and leaving debris and vacancies behind. We also, sometimes, observed the formation of vacancies behind a dislocation in Regime II (**Figure 3.7**).

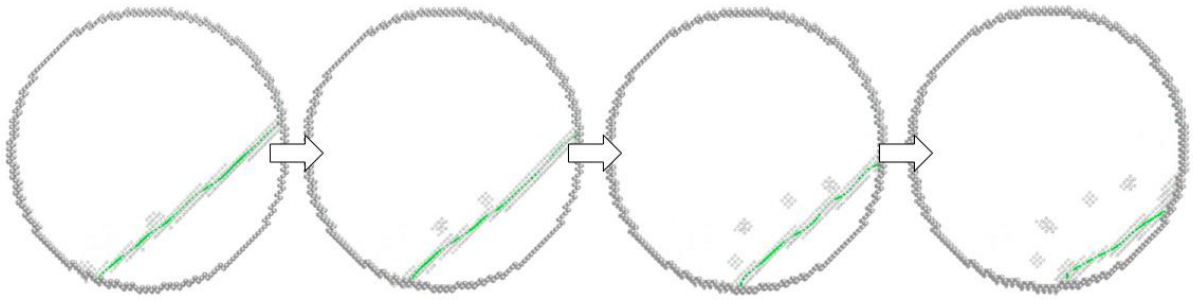

**Figure 3.7. Formation of vacancies after the motion of dislocation in Regime II. Thermally-assisted evolution of dislocation structures produces vacancies.**

### 3.3.3. Regime III: Segmentation Steady-state

As discussed in the previous two Sections, there are two competitive mechanisms in the operation of dynamic dislocation source; lattice resistance and dislocation segmentation. Our results show that the effect of these two main mechanisms becomes saturated in Regime III (**Figure 3.4**). The saturation of critical shear stress could be understood by the balance between the formation and annihilation of dislocation segments. Each segment is joined at the connecting node, i.e., pinning point, which is also mobile. We noticed that the source operation sometimes pushes out the connecting nodes toward the free surface, and the surface dislocation segment is annihilated. In Regime III, we often saw that the first connecting node is annihilated (**Figure 3.8**). Thus, at a temperature in Regime III, the creation of dislocation segment due to thermal cross-slip would balance with the annihilation at the free surface. Then, the total number of

segment (or the average length of each segment) would be relatively constant, and the critical shear stress of SCDM does not change much in Regime III. In Regime III, the intrinsic lattice resistance is zero for both Nb and Mo. Thus, the critical stress of SCDM would be determined by dislocation structure more than dislocation mobility. Because a dislocation structure is dynamically under steady-state, constant critical stress of SCDM can be expected as seen in our results (**Figure 3.4**).

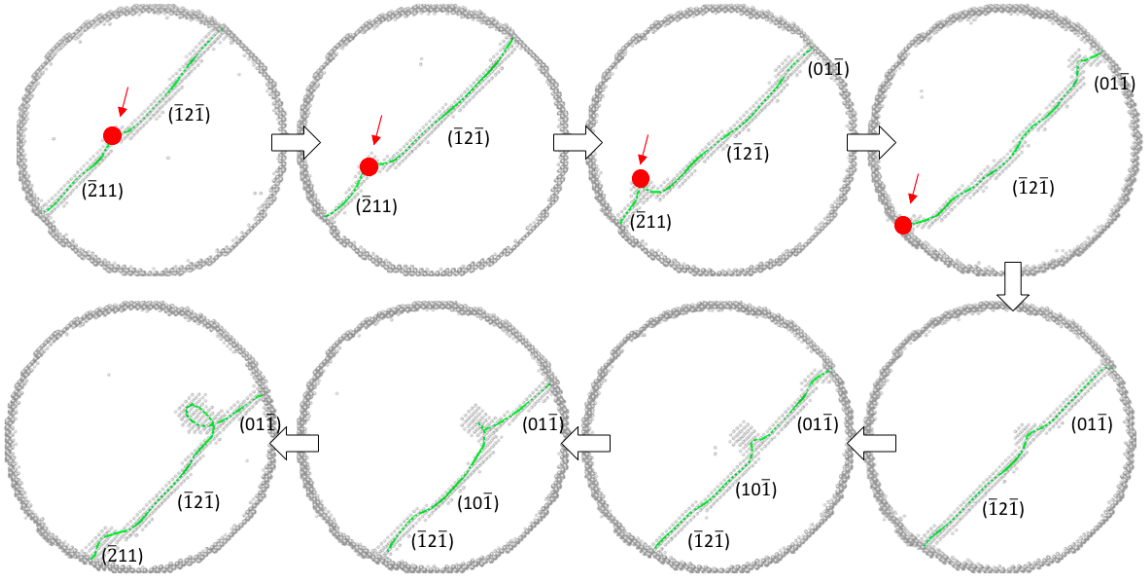


**Figure 3.8. Evolution of dislocation structures in Regime III. In Regime III, dislocation segmentation becomes more dynamic, so cross-slip occurs more vibrantly. Creation and annihilation of dislocation nodes occur continuously. The red point (with the red arrow) corresponds to the dislocation node, which is initially created, and is annihilated during the motion of dislocation.**

### 3.3.4. Dislocation source model

As Weinberger *et al.* suggested, the SCDM is fundamentally similar with the dislocation multiplication of Frank-Read source. Several micropillar studies have suggested that the operation of dislocation source at the nano-/micro-meter scale consists of three contributions, (1) intrinsic lattice resistance, (2) elastic interaction with other dislocations, and (3) dislocation line tension [40]. Because we have only one dislocation at the beginning of simulation, the elastic interaction term could be ignored. Thus, the intrinsic lattice resistance and dislocation line tension would be the major factors that determine the critical shear stress of SCDM.

Regime I shows the monotonic decrease in critical shear stress. As a first order approximation, let us assume the linear dependence of critical shear stress with temperature (**Figure 3.9(a)**). Because there is no segmentation in Regime I, the effects of line tension should be nearly constant in Regime I. In Regime II, the effect of line tension increases significantly due to the dislocation segmentation but becomes constant in Regime III. Thus, we can assume that the contribution of line tension to the critical shear stress for SCDM is nearly a step-like function (**Figure 3.9(b)**). Finally, the total three regimes can be described by the summation of the temperature-dependent lattice resistance and line tension (**Figure 3.9(c)**). Surprisingly, our model can capture even the presence of the small peak at the beginning of region III (**See the arrow in Figure 3.9(c)**). The combined effects of lattice resistance tail and segmentation saturation at the beginning of Regime III produces the small peak of critical shear stress. Once the lattice resistance becomes zero, the critical shear stress of SCDM becomes constant due to the steady-state segmentation as discussed in Section 3.3.

Based on the suggested scheme above, it is possible to extract the contributions of lattice resistance and line tension separately from our simulation results (**the second and third figures**

**in Figure 3.9(b) and 3.9(c)**). First, based on our analysis above, we can assume that the lowest temperature in the constant critical shear stress range in Regime III corresponds to the temperature at which the lattice resistance disappears completely. Then, we can estimate the temperature dependence of lattice resistance with the linear-fitted line that starts from the zero lattice resistance point. This fitted line of lattice resistance should have the same slope with the simulation data because the line tension is not dependent on temperature in Regime I. Then, by subtracting the lattice resistance from the total data, we can obtain the temperature-dependent line tension data. This simple model also allows us to obtain several useful quantities such as the lattice resistance at 0 K (Peierl's barrier), the temperature at which the lattice resistance becomes zero, and the athermal stress of source operation (Regime I). All these quantities are available in **Table 3.1**.

| | Peierls barrier [GPa] | Temperature at which the lattice resistance becomes zero [K] | Athermal stress of source operation [GPa] |
|---|---|---|---|
| Mo nanowire | 4.7 | 650 | 4.5 |
| Nb nanowire | 1.6 | 275 | 1.2 |

**Table 3.1.** Useful quantities obtained by the dislocation source model

Therefore, our model can capture the general trend of critical shear stress of SCDM with temperature by combining the temperature dependences of lattice resistance and line tension (dislocation segmentation). Several calculations of intrinsic lattice resistance indeed show the nearly linear dependence of temperature only except the tail region at a high temperature [41]. In our works, other factors (the presence of free surfaces, the shape of dislocations, and the

dislocation line tension) seem to slightly change the shape of curve from linear-like exponential to linear ones. As noted in the previous paragraph, it is challenging to extract the non-linear behavior from the data in Figure 4 because the contributions of other factors cannot be quantified easily. However, the linear approximation would be good enough as the first order approximation because the dislocation mobility is a dominant factor and its temperature dependence is not far from the linear dependence.

Note that Nb has a low Peierl's barrier while Mo has a relatively high Peierl's barrier. Regardless of a large difference in Peierl's barrier, both showed the similar trend. This result implies that our observation could be extended to other bcc metal nanowires. Thus, the SCDM behavior could be controlled generally by the temperature-dependent lattice resistance and the dynamics of dislocation segmentation in bcc metal nanowires.

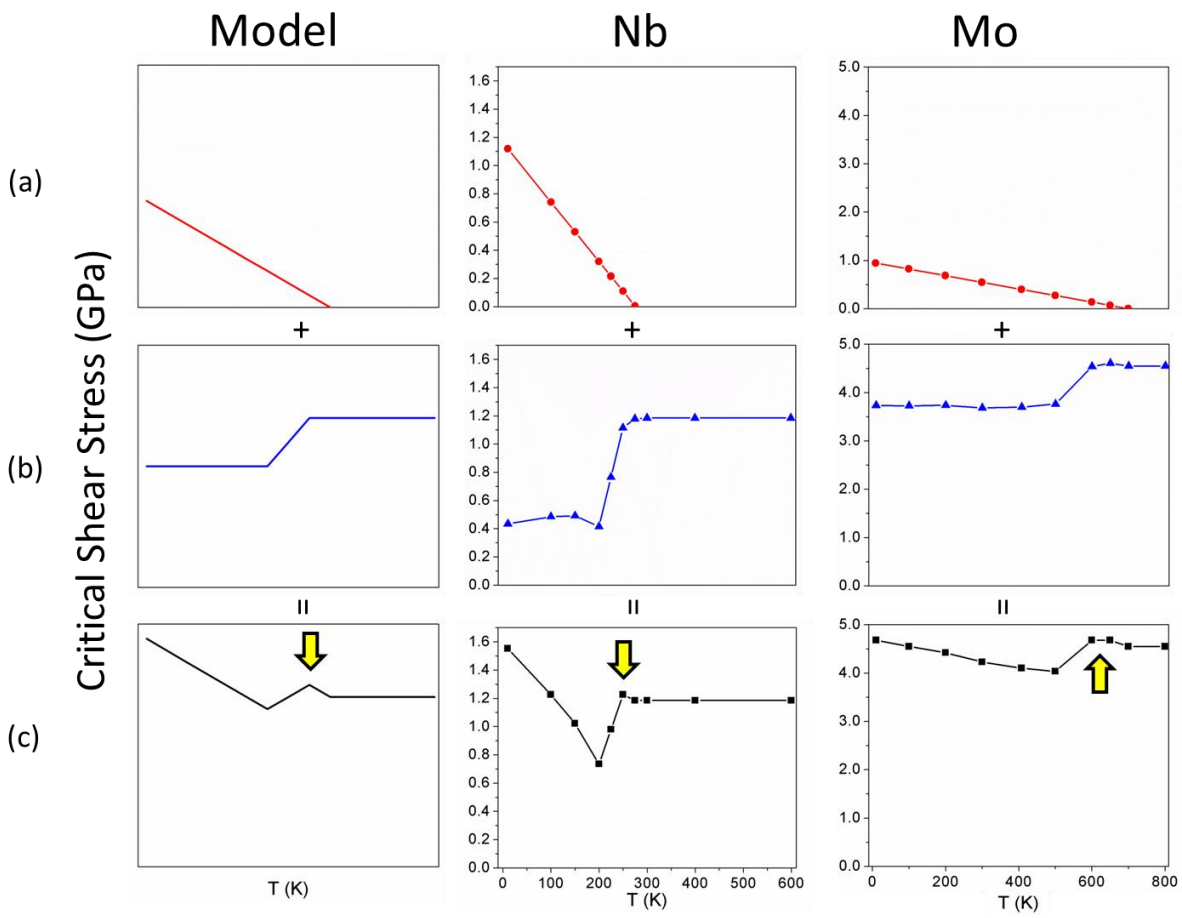


**Figure 3.9. he effects of lattice resistance and line tension on the critical shear stress of SCDM. (a) Schematics of lattice resistance; (b) line tension; (c) the critical stress, which is the summation of (a) and (b). Starting from the left, the figures are from an analytic model, Nb nanowire simulations, and Mo nanowire simulations. Note that the tail of lattice resistance produces the small peak of critical shear stress at the beginning of Regime III. This result is consistent with our simulation data.**

## 3.4. Concluding remarks

The main goal of this work was to understand how temperature affects dislocation self-multiplication in bcc metals by means of atomistic simulations and a dislocation source model. We implemented the constant stress method to achieve more precise control of the applied stress. We observed that as temperature changes, the dislocation motion and its multiplication mechanism in both Nb and Mo nanowires appear to have three distinct regimes regardless of different lattice resistance (or Peierls barrier). Our analysis showed that the temperature dependence of lattice resistance and dislocation segmentation explain the presence of three different regime of critical shear stress. In Regime I, the lattice resistance varies with temperature, but there is no dislocation segmentation. Thus, the critical shear stress decreases with temperature in Regime I. In Regime II, dislocation segmentation starts to occur, so the line tension stress increases significantly. Thus, the critical shear stress abruptly increases with temperature in Regime II. In Regime III, the dislocation segmentation seems to be nearly constant, and the lattice resistance is completely removed. Thus, the critical shear stress does not change with temperature. In addition, we suggested a dislocation source model that combines the linear dependence of lattice resistance and the step function-like dependence of line tension stress. This model successfully describes three different regimes of critical stress and even the presence of a small peak at the early stage of Regime III. We believe that our results can provide a mechanistic description of the dislocation multiplication process of a screw dislocation in bcc metals at small length scales at various temperatures.

3.5. References

[1] V. Volterra, in: Annales scientifiques de l'École normale supérieure, 1907, pp. 401-517.
[2] G.I. Taylor, Proceedings of the Royal Society of London. Series A, Containing Papers of a Mathematical and Physical Character, 145 (1934) 362-387.
[3] M.D. Uchic, D.M. Dimiduk, J.N. Florando, W.D. Nix, Science, 305 (2004) 986-989.
[4] D.S. Gianola, A. Sedlmayr, R. Mönig, C.A. Volkert, R.C. Major, E. Cyrankowski, S. Asif, O.L. Warren, O. Kraft, Review of Scientific Instruments, 82 (2011) 063901.
[5] S. Shim, H. Bei, M.K. Miller, G.M. Pharr, E.P. George, Acta Materialia, 57 (2009) 503-510.
[6] A. Budiman, S. Han, J. Greer, N. Tamura, J. Patel, W. Nix, Acta Materialia, 56 (2008) 602-608.
[7] Y. Cui, G. Po, N. Ghoniem, Acta Materialia, 108 (2016) 128-137.
[8] E.L. Huskins, Z.C. Cordero, C.A. Schuh, B.E. Schuster, Journal of materials science, 50 (2015) 7058-7063.
[9] S. Wang, Y. Yang, L. Zhou, Y.-W. Mai, Journal of Materials Science, 47 (2012) 6047-6055.
[10] Y. Yang, C.T. Liu, Journal of Materials Science, 47 (2012) 55-67.
[11] D. Dimiduk, M. Uchic, S. Rao, C. Woodward, T. Parthasarathy, Modelling and Simulation in Materials Science and Engineering, 15 (2007) 135.
[12] G. Song, T. Kong, K.J. Dusoe, P.C. Canfield, S.-W. Lee, Journal of Materials Science, 1-11.
[13] J.R. Greer, W.C. Oliver, W.D. Nix, Acta Materialia, 53 (2005) 1821-1830.
[14] S.-W. Lee, S.M. Han, W.D. Nix, Acta Materialia, 57 (2009) 4404-4415.
[15] K. Ng, A. Ngan, Scripta Materialia, 59 (2008) 796-799.
[16] H. Bei, S. Shim, E.P. George, M.K. Miller, E. Herbert, G.M. Pharr, Scripta Materialia, 57 (2007) 397-400.
[17] C. Chisholm, H. Bei, M. Lowry, J. Oh, S.S. Asif, O. Warren, Z. Shan, E.P. George, A.M. Minor, Acta Materialia, 60 (2012) 2258-2264.
[18] S. Brinckmann, J.-Y. Kim, J.R. Greer, Physical review letters, 100 (2008) 155502.
[19] C.R. Weinberger, W. Cai, Proceedings of the National Academy of Sciences, 105 (2008) 14304-14307.
[20] K. Maier, M. Peo, B. Saile, H. Schaefer, A. Seeger, Philosophical Magazine A, 40 (1979) 701-728.
[21] A. Misra, M. Demkowicz, X. Zhang, R. Hoagland, Jom, 59 (2007) 62-65.
[22] M. Brivio, W. Verboom, D.N. Reinhoudt, Lab on a Chip, 6 (2006) 329-344.
[23] I. Augustyniak, J. Dziuban, P. Knapkiewicz, M. Matusiak, M. Olszacki, P. Pons, in: Solid-State Sensors, Actuators and Microsystems (TRANSDUCERS & EUROSENSORS XXVII), 2013 Transducers & Eurosensors XXVII: The 17th International Conference on, IEEE, 2013, pp. 1503-1506.
[24] C.W. Roddy, R.L. Covington, K.M. Ravi, C. Bonavides, M. Bittar, G. Moake, B. Mandal, in, Google Patents, 2012.
[25] A. Schneider, D. Kaufmann, B. Clark, C. Frick, P. Gruber, R. Mönig, O. Kraft, E. Arzt, Physical review letters, 103 (2009) 105501.
[26] J. Millett, M. Cotton, N. Bourne, N. Park, G. Whiteman, Journal of Applied Physics, 115 (2014) 073506.
[27] S. Plimpton, Journal of computational physics, 117 (1995) 1-19.
[28] G. Ackland, R. Thetford, Philosophical Magazine A, 56 (1987) 15-30.
[29] M.R. Fellinger, H. Park, J.W. Wilkins, Physical Review B, 81 (2010) 144119.

[30] S. Kotrechko, O. Ovsjannikov, N. Stetsenko, I. Mikhailovskij, T. Mazilova, M. Starostenkov, Philosophical Magazine, 96 (2016) 473-485
[31] L.G. Wang, and A.Van de Walle, Physical Chemistry Chemical Physics, 14 (2012) 1529-1534.
[32] K. Kang, W. Cai, International Journal of Plasticity 26 (2010) 1387-1401.
[33] V. Bulatov, W. Cai, Computer simulations of dislocations, Oxford University Press on Demand, 2006.
[34] D. Mordehai, S-W. Lee, B. Backes, D.J. Srolovitz, W.D. Nix, E. Rabkin, Acta Materialia 59 (2011) 5202-5215.
[35] R. Kositski, O. Kovalenko, S-W. Lee, J.R. Greer, E. Rabkin, D. Mordehai, Scientific reports 6 (2016) 25966
[36] A. Stukowski, Modelling and Simulation in Materials Science and Engineering, 18 (2009) 015012.
[37] G. Po, Y. Cui, D. Rivera, D. Cereceda, T.D. Swinburne, J. Marian, N. Ghoniem, Acta Materialia, 119 (2016) 123-135.
[38] H. Conrad, W. Hayes, Trans. Am. Soc. Metals, 56 (1963).
[39] J. Marian, W. Cai, V.V. Bulatov, Nature Materials, 3 (2004) 158.
[40] B. Devincre, M. Condat, Acta metallurgica et materialia, 40 (1992) 2629-2637.
[41] T. Suzuki, H. Koizumi, H.O. Kirchner, Acta metallurgica et materialia 43 (1995) 2177-2187

**Chapter 4.** Uni-axial compression of single crystalline intermetallic compound at low temperatures: Superelasticity of an intermetallic compound, $CaKFe_4As_4$ and its temperature dependence

**(**Reproduced from "Song, G, et al., *APL Materials* 7.6 (2019): 061104", with the permission of AIP Publishing)

## 4.1. Introduction

Intermetallic compounds often exhibit superior/exceptional physical and chemical properties due to their uniquely ordered atomic arrangements [1] but their practical applications have been significantly limited because most of them are extremely brittle and cannot absorb a sufficient amount of mechanical energy before failure occurs [2]. Their rigid covalent/ionic bonds and complex crystal structures usually do not permit plastic deformation or structural transition, leading to brittle failure at an elastic limit of less than 1%. Therefore, it is extremely rare to obtain a large elastic limit over 10% in intermetallic compounds except for some special cases such as shape memory alloys where the heat or magnetic field induces the large strain recovery [3-8].

Recent studies on mechanical behavior of materials at the nano-/micro-meter scale revealed that a material could sustain a higher stress and higher elastic limit as its dimension decreases [9-15]. Particularly for a brittle material, according to the weakest link mechanism, a smaller sample contains a smaller number of defects statistically, leading to higher fracture strength as well as a higher fracture strain [16-18]. For instance, nanowires and nanoparticles often exhibit ultrahigh elastic strain, compared to their corresponding bulk materials [19-21]. Large elastic deformation at the nano-/micro-scale could induce substantial changes in structure and material property and could enable strain engineering, which refers to the modification of material

properties through elastic strain [15]. One of the most known examples would be the increase in carrier mobility in elastically-strained silicon under bi-axial strain [22]. Because the size effect on elastic strain has been widely observed in brittle materials at small length scales, it could be seen also in novel intermetallic compounds at the nano-/micro-meter scale.

Recently, high temperature Fe-based superconductors have drawn strong attention due to their superconducting capability even in the presence of magnetic Fe, which has been regarded as a harmful element for superconductivity [23-24]. Now, they are regarded as a great material system that allows the study of relationship between superconductivity and magnetism. $ThCr_2Si_2$-structured Fe-based pnictides have been extensively studied due to their strong pressure sensitivity of structure and electronic/magnetic properties [25]. Particularly, $CaFe_2As_2$ single crystals undergoes the collapsed tetragonal (cT) phase transition, which leads to ~10% reduction of c-axis lattice parameter under hydrostatic pressure [26]. We also performed uniaxial mechanical tests on $CaFe_2As_2$ micropillars and observed unique mechanical behaviors including ~13% of superelasticity, superior fatigue resistance, and cryogenic shape memory effects, and micaceous plasticity [27, 28]. Notably, magnetism of $CaFe_2As_2$ changes from paramagnetic (or antiferromagnetic) to nonmagnetic states when the cT transition occurs [26]. Thus, strain engineering of magnetism is possible for $CaFe_2As_2$ or its related structures.

Recently, the hybrid structures of Fe-based pnictides, $CaKFe_4As_4$, has been actively investigated due to its high temperature superconductivity (Tc~35 K) [29]. The previous study confirmed that superconductivity can be switched off under hydrostatic pressure through the half collapsed tetragonal transition (hcT) around Ca atom [29]. However, uniaxial mechanical tests on $CaKFe_4As_4$ have never done, and it should be interesting to see how differently $CaKFe_4As_4$ behaves, compared to $CaFe_2As_2$ in terms of superelasticity. The insertion of large K atoms into

the lattice makes the As-As distance around K atom larger. The larger interplanar spacing could allow the larger linear elastic strain simply because the widely-spaced layers could be compressed more. However, the large As-As distance would make the As-As bond formation more difficult. Thus, the competition of these two factors could affect the total elastic strain. In addition, we noticed that the plastic slip (or shear fracture) of $CaFe_2As_2$ occurs in the 1/3[3 1 $1\bar{]}$(1 0 3) slip system under compression along c-axis. Due to the larger c-axis length of $CaKFe_4As_4$ [29], the slip vector of $CaKFe_4As_4$ in the same slip system should be larger than that of $CaFe_2As_2$, implying that $CaKFe_4As_4$ would exhibit the higher yield strength, based on the Peierls-Nabarrow model [30, 31]. In this sense, $CaKFe_4As_4$ could exhibit the elastic strain larger than that of $CaFe_2As_2$.

In this study, therefore, we performed uniaxial micropillar compression tests and Density Functional Theory calculation to investigate the superelastic properties of $CaKFe_4As_4$ and compared the mechanical data with those of $CaFe_2As_2$. We found a giant elastic limit, up to 17%, in $CaKFe_4As_4$, under uniaxial compression along the c-axis of their unit cells. Density functional theory calculations revealed that its enormously large elastic strain primarily results from atomic bond formation around Ca atom and local elastic compliance around K atom. Also, the cyclic compression test on $CaKFe_4As_4$ showed that the superelastic deformation over 10% strain is completely reversible when the applied force is relaxed. This uniaxial process is entirely distinct from the conventional shear-based superelastic mechanism, martensite-austenite phase transformation of shape memory alloys and ceramics [3-8]. Moreover, we also used our custom-built in-situ cryogenic micromechanical testing system to investigate the effects of temperature on the first hcT transition, which is known to remove superconductivity in $CaKFe_4As_4$. We found that the onset stress of the first hcT transition near the superconducting transition

temperature is much lower than the fracture strength. This result suggests that there is a strong possibility to see the superconductivity switching even under uniaxial compression before fracture occurs.

## 4.2. Experiments and Computation

$CaFe_2As_2$ is grown from a Sn-rich solution, and $CaKFe_4As_4$ was grown from excess FeAs. The constituent materials were put in alumina crucibles, which are located in an amorphous silica ampule. Single crystals were slowly grown under slow cooling in a furnace and were quickly decanted using a centrifuge. The detailed descriptions of the solution growth of our crystals are also available elsewhere [32, 33]. Micropilllars are fabricated using focused-ion beam milling, Helios Nanolab 460F1 (Thermo Fisher, USA). Gallium ion beam currents from 300 to 10 pA under an operating voltage of 30 kV were used from the initial to final thinning with concentric circle patterns. Because the typical thickness of FIB damage layer is about 20 nm, which is much thinner than our pillar diameter (~2 μm), we expect negligible effects of FIB damage on the mechanical data. In-situ nanomechanical test was performed at room temperature and under an high vacuum condition ($<10^{-4}$ Pa) using a NanoFlipTM (KTL-Tencor, USA), which is installed in a field-emission gun JEOL 6335F scanning electron microscope (JEOL, Japan). A nominal displacement rate of 10 nm/s, which corresponds to the engineering strain rate of ~0.002 $s^{-1}$, was used for all in-situ compression tests in this study. Strain calculations for experiments were done with the Sneddon punch correction using the effective Young's modulus that can be measured by nanoindentation [34]. The recorded video was often used to visually confirm that our strain measurements were accurate. A liquid nitrogen and helium cryostat, ST-100, was used to perform nanomechanical testing at low temperatures to investigate the

temperature effects on mechanical properties. The temperature of the diamond tip was maintained to be similar with that of the sample by using thermal equilibration, leading to a thermal drift below 0.5 nm/sec at all times. A detailed description of our cryogenic system is also available in the Supplementary Information (**Supplementary Note 1** in the supplementary material). Contact stiffness was measured during compression testing by applying a force oscillation with 10 nN in amplitude and 200 Hz in frequency and measuring the resultant displacement oscillation. Contact stiffness data often shows the clearer evidence of lattice collapse than stress-strain curve [35]. The contact stiffness, S, is measured by

$$S = \left[ \frac{1}{\frac{P_{OS}}{h(\omega)} cos\phi - (K_S - m\omega^2)} - K_f^{-1} \right]^{-1} \quad \text{(Equation 3.1)}$$

, where $P_{OS}$ is the magnitude of force oscillation, h(ω) the magnitude of resulting displacement oscillation, ω is the frequency of oscillation, ϕ the phase angle between the force and displacement signals. $K_S$ and $K_f$ are the stiffnesses of the leaf spring and indenter frame, respectively [34]. When structural collapse occurs, the phase angle becomes smaller, providing a lower contact stiffness. This method is useful to capture the availability of structural collapse during micromechanical test.

For Density Functional Theory calculations, structure optimization in the $CaKFe_4As_4$ system was performed using state-of-the-art projector-augmented wave method [36] and the generalized-gradient approximation [37] available in VASP code [38]. The energy cutoff was set to 800 eV and the k-mesh dimensions were (5x5x5). Although the system doesn't show a long-range magnetic order, the inclusion of Fe local moments in the simulation is necessary for a correct description of structural transitions under pressure, as detailed in previous studies [29,39]. For that reason, we imposed the "frozen" spin-vortex spin configuration on the Fe sublattice

which approximates the effect of spin fluctuations present in this material [39]. In the current work, we simulate the uniaxial [001]-strain conditions by varying the c-lattice parameter and calculating the total energies of $CaKFe_4As_4$ structures optimized for different a-lattice parameters. Fit to the Birch-Murnaghan equation of state

$$E(V) = E_0 + \frac{bV}{b_0(b_0-1)}\left[b_0\left(1-\frac{V_0}{V}\right)+\left(\frac{V_0}{V}\right)^{b_0}-1\right] \quad \text{(Equation 3.2)}$$

allowed to estimate the equilibrium lattice parameters for a given value of strain. In the final step, the internal atomic positions are optimized for the fixed lattice dimensions and the stress value along the c-axis was obtained. The electronic properties of the optimized structures were calculated using the all-electron full-potential localized orbitals basis set (FPLO) code [40] within the GGA approach. The half-collapsed tetragonal transition was captured by inspecting the energy position of the As 4pz antibonding orbitals near the Ca layer [29,39]. In order to illustrate the two half-collapse transitions in $CaKFe_4As_4$ under the uniaxial load, we plot the real-space distribution of the electron density associated to the As 4pz orbitals across both Ca and K layers at different pressures. These density maps were obtained from the Wannier functions calculated using the FPLO code [40] and the tricubic interpolation [41,42] on a three-dimensional grid.

Bulk single crystals (**Figures 4.1(a)** and **4.1(b)**) of $ThCr_2Si_2$-type intermetallic compound ($CaFe_2As_2$) and its hybrid structure ($CaKFe_4As_4$) were grown using a solution growth method [17, 18], and cylindrical micropillars with ~2 μm in diameter and ~6 μm in height were fabricated along the [0 0 1] direction using focused-ion beam (FIB) milling. Note that the $CaKFe_4As_4$ structure can be thought of as a periodic replacement of half of the Ca in $CaFe_2As_2$

with K in an alternating order along the c-axis, and it looks like a hybrid of $CaFe_2As_2$ and $KFe_2As_2$ [29,43].

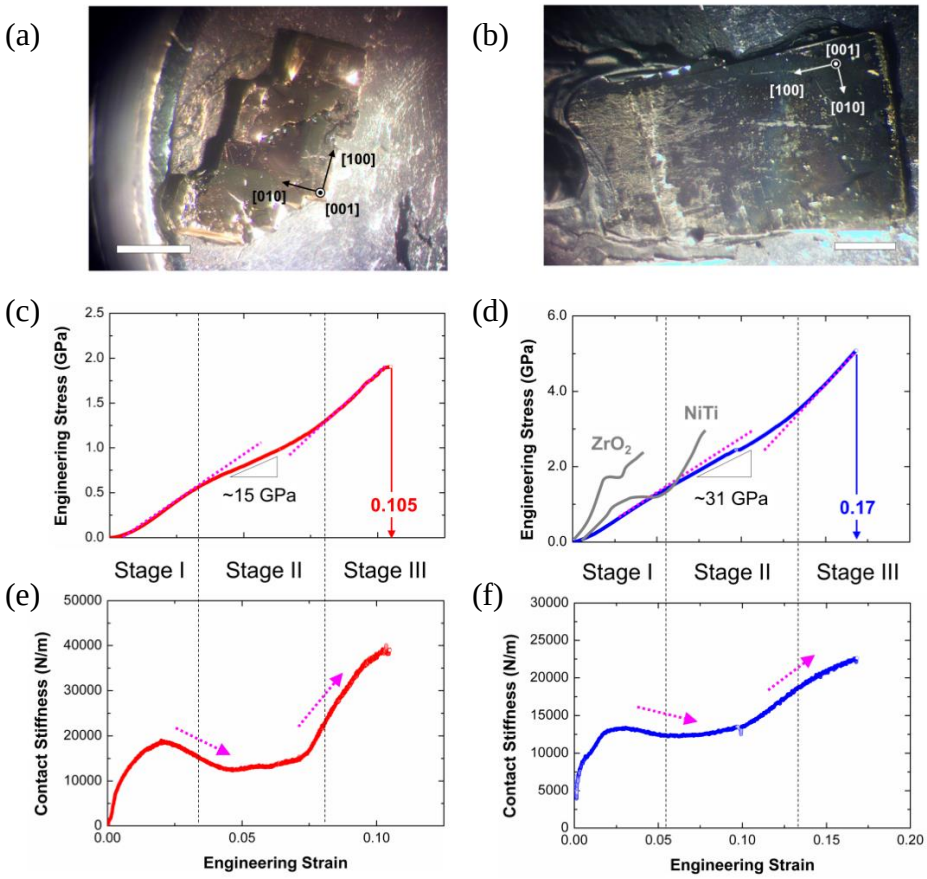


**Figure 4.1. Solution-grown single-crystalline intermetallic compounds and room temperature mechanical data.** Optical micrographs of (a) $CaFe_2As_2$ (scale bar, 1mm) and (b) $CaKFe_4As_4$ (scale bar, 1mm); Uniaxial engineering stress-strain data until failure occurs of (c) $CaFe_2As_2$ and (d) $CaKFe_4As_4$; Contact stiffness as a function of engineering strain of (e) $CaFe_2As_2$ and (f) $CaKFe_4As_4$. All stress-strain data exhibit three stages of elastic deformation, which is similar with that of shape memory alloys. The decrease in contact stiffness implies that a material becomes more elastically compliant under compression and corresponds to the structural transition from tetragonal to fully-collapsed ($CaFe_2As_2$) or one or both half-collapsed

($CaKFe_4As_4$) tetragonal structures. For comparison, the stress-strain curves of the elastic regime of superelastic zirconia [44] and NiTi [45] micropillars were added in Figure 4.1(d)**.**

## 4.3. Results and Discussion

The representative stress-strain data of $CaFe_2As_2$ and $CaKFe_4As_4$ show a large compressive elastic limit of 10.5 and 17%, respectively (**Figures 4.1(c)** and **4.1(d)**). For comparison, the superelastic regime of the stress-strain data for superelastic zirconia [44] and NiTi [45] micropillars, both of which are well-known superelastic materials, are plotted together with our $CaKFe_4As_4$ data (**Figure 4.1(d)**). It is clearly seen that our materials exhibit much greater performance in terms of both yield strength and elastic limit. We identify three stages in the stress-strain data. Interestingly, the non-linear stress-strain responses of our crystals resemble that of typical superelastic shape memory alloys, suggesting that the uniaxial deformation of our crystals would induce a structural transition, too. Also, the deformation is completely reversible when the applied load is relaxed (**Figure S. 1 in the supplementary material and the inset of Figure 5 shown below**) and is repeatable under cyclic deformation (Ref. 28 and **Figure S. 2 in the supplementary material**). Note that we have never seen any evidences of shear deformation from more than 20 samples tested. The real-time SEM videos always showed a clean surface until fracture occurs. Thus, our superelasticity does not appear to be related to any conventional shear-based mechanism such as martensite-austenite phase transformation, which forms shear bands and causes a significant lateral displacement particularly in the case of a single crystal [44].

The decrease in contact stiffness within Stage II looks counter-intuitive (**Figures 4.1(e)** and **4.1(f)**) because the contact stiffness of a solid material usually increases during compression

[10]. Hoffmann and Zheng hypothesized that such a decrease would be possible through a process of forming and breaking Si-Si-type bonds in $ThCr_2Si_2$-type structures under uniaxial compression along the c-axis [46]. Our previous works on $CaFe_2As_2$ confirmed that the main mechanism of phase transition is the structural collapse through the formation of As-As bonds under uniaxial compression along the c-axis [27,47-49]. Thus, the decrease in contact stiffness indeed results from a strain-induced structural collapse through As-As bond formation in these structures. On the course of deformation, the formation of As-As bonds makes materials more elastically compliant, but once the lattice collapse is almost complete, the contact stiffness increases again. Thus, stage I and III would correspond to the elastic deformation before and after formation of As-As bonds, respectively. Stage II would correspond to the deformation on the course of As-As bond formation.

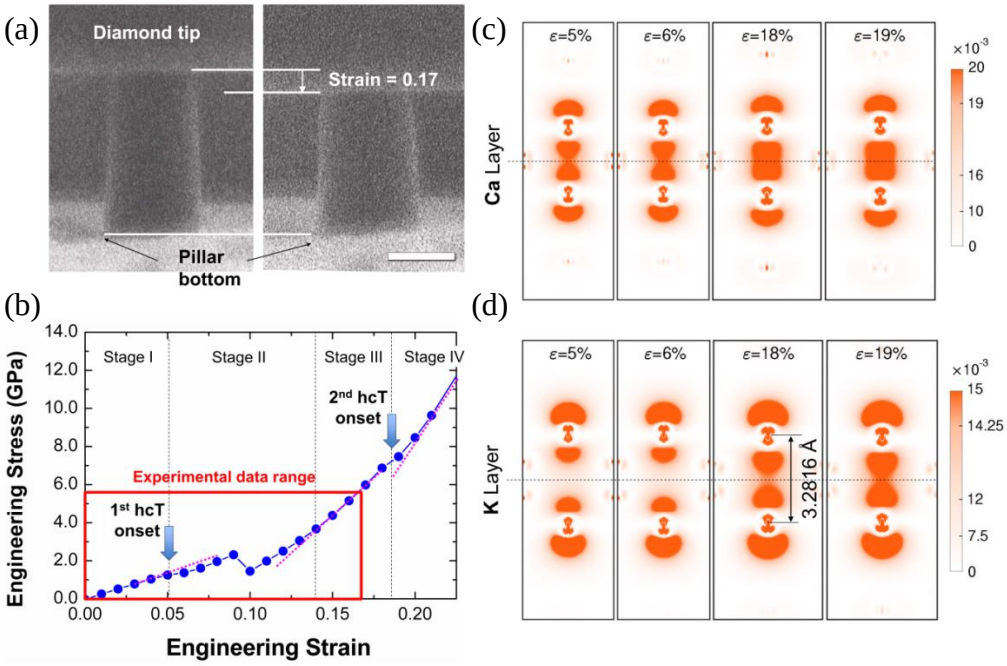


**Figure 4.2. Superelasticity of $CaKFe_4As_4$.** (a) Snapshots of *in-situ* video right before contact with the diamond tip and right before failure (scale bar, 1μm); (b) DFT simulation results of

engineering stress-strain data. Red-line box represents the experimental data range that is limited by fracture. Note that the sharp drop of engineering stress around 0.1 strain occurs due to the collapse of magnetic moments, which are intentionally introduced to mimic paramagnetic state. Due to random distribution of magnetic moments at a finite temperature in a real system, this effect would spread within Stage II. Stage IV corresponds to the elastic deformation after the second hcT transition, which cannot be seen in a real system due to fracture in Stage III.; Non-spin-polarized electron density in the *ac* plane associated with the As-$4p_z$ orbitals near (c) Ca and (d) K at different strains. (c) shows clear bond formation across the Ca-layer by 0.05 strain and (d) shows clear bond formation across K-layer by 0.18 strain.

Note that the elastic limit 15~17% of $CaKFe_4As_4$ is truly extraordinary, compared to any other shape memory intermetallic compounds, as well as $CaFe_2As_2$ (11~14%) in this study (**Figures 4.1(d)** and **4.2(a)**). Our Density Functional Theory (DFT) calculations of $CaKFe_4As_4$ under uniaxial strain find two half-collapsed tetragonal (hcT) transitions for this system (**Figures 4.2(b)**, **4.2(c)**, and **4.2(d)**), while the full-collapsed tetragonal (cT) transition is observed in $CaFe_2As_2$ [27,48]. This result is qualitatively similar to results of application of hydrostatic pressure [26,29,49,50]. Non-spin-polarized electron density associated with the As-4pz orbitals clearly shows the presence of two separate hcT transitions in $CaKFe_4As_4$ at different strains (**Figures 4.2(c)** and **4.2(d)**). In $CaKFe_4As_4$, the first hcT appears at a strain of ~0.05-0.08 when As atoms around Ca form As-As bonds. The smaller atomic radius (231 pm) of the Ca atom allows a shorter As-As distance (3.107 Å) around it, leading to the formation of As-As bonds under a low compressive strain (~0.05). Thus, the structural transition in Stage II of $CaKFe_4As_4$ (**Figure 4.1(d)**) would be related to the deformation after the onset of the first hcT transition.

Based on our DFT data, the second hcT occurs at strain values near the experimentally measured elastic limit (fracture strain), ~0.18-0.19. At this transition, As atoms around K form As-As bonds. Since the atomic radius of K (280 pm) creates a longer-distance between the As-As layer (4.205 Å), larger elastic strain is needed to reach the second hcT transition. Thus, Stage III of $CaKFe_4As_4$ would correspond to the gradual formation of As-As bonds around K atom. All these results also explain a higher rate of structural collapse per strain for the full collapse in $CaFe_2As_2$ (~15 GPa) than that for the half collapse in $CaKFe_4As_4$ (~31 GPa) for Stage II deformation (**Figures 4.1(c)** and **4.1(d)**).

We also carefully monitored our DFT data to examine the contribution of As-As layers near a K atom to the total elastic strain. The interlayer distance of As-As layer around a K atom is 3.2816Å near the elastic limit. By considering that it is 4.205Å before compression, its change contributes to (4.205Å -3.2816Å)/(12.6205 Å, initial c-length) ≈ 0.073 of strain (~41% of the total elastic limit), which is remarkably high. (**the third figure in Figure 4.2(d)** and **Figure S. 3 in the supplementary material**). This result implies that the larger atom size of K makes the formation of As-As bond more difficult but makes the region between As-As layers around the K atom more elastically compliant. Also, note that our elastic limit, ~17%, is close to the elastic strain at which the second hcT occurs in our DFT data. The driving force of the second hcT, i.e., the formation of As-As bonds around the K atom would partially contribute to a large elastic compliance. In view of these observations, we attribute the extraordinary elastic limit of $CaKFe_4As_4$ to the presence of these two hcT transitions and the larger atomic size of K. Therefore, it is important to control bond formation and local elastic compliance to tune the superelastic properties.

The elastic limits of our intermetallic compounds are exceptionally high, compared to other superelastic materials even in similar length scales (**Figure 4.3(a)**, **Figure. S. 4 and Supplementary Note 2 in the supplementary material**) [51]. The comparable superelastic strain can be observed only when the dimension of shape memory intermetallic compounds become close to 100 nm. Usually, materials become stronger when the sample dimension is reduced to the nanometer length scale for various reasons [9-19]. For instance, NiTi nanopillars with 150 nm in diameter exhibit an improved yield strength, leading to a 15% elastic limit [52]. If the micrometer length-scale of our specimen is considered, the observed elastic limit (10~17%) is absolutely outstanding. Note that we also observed size effect in $CaFe_2As_2$. Its sub-micron sized pillars exhibit ~17% elastic strain (**Figure S. 5 in the supplementary material**). This size effect could be related to the weakest-link mechanism [16]. Brittle materials often exhibit higher strength and higher elastic limit when they become extremely small. This has been observed in various brittle materials, such as ceramic, diamond, metallic glass, and nanowires, and the weakest-link mechanism is one of the most widely accepted ideas [16-18,53]. If a sample dimension becomes larger, it is more likely to have weaker defects that can induce brittle failure at a lower strength. Vice versa, fracture strength (also, elastic limit) increases as the sample dimension becomes smaller because it is unlikely to find the weak defect. If the diameter of our specimens is also reduced further down to sub-100 nm, it would be possible for them to show much greater performance, and the detailed analysis on the size effect will presented in a separate work.

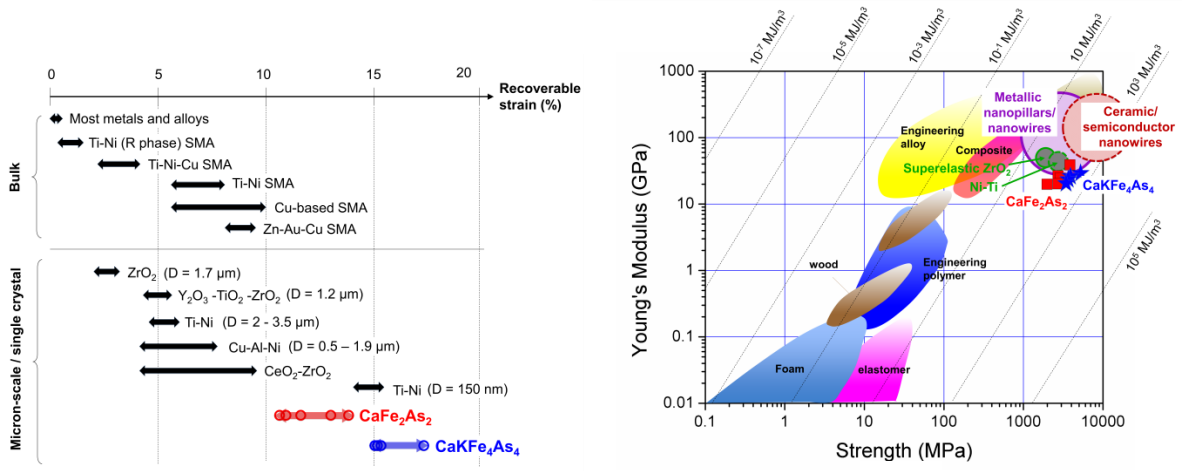


(a) (b)

**Figure 4.3. Superelastic performance of of $CaFe_2As_2$ and $CaKFe_4As_4$.** (a) Elastic limit of superelastic materials at different length scales [51]. The range of recoverable strain (the range of double-headed arrow) shows the minimum and maximum values of our experimental data. Circles in the arrows of our samples indicate the data we obtained (**Figures S6** and **S7** in the supplementary material); (b) Ashby Chart of Young's modulus and yield strength. The dotted lines are the contours of modulus of resilience, which is the total strain energy absorption per unit volume prior to yielding. Data of nanopillars and nanowires are available in Supplementary Information (See **Supplementary Note 3**).

It is also worthwhile to compare the elastic performance with other advanced engineering materials. The Ashby Chart has been extensively used when material properties of new materials need to be compared with those of other materials [54-56]. Our materials are located in the $E$-$\sigma_y$ space of the Ashby chart (**Figure 4.3(b)**), where $\sigma_y$ is yield strength and E is Young's modulus [57]. Due to the non-linearity of the stress-strain curve, the effective Young's modulus ($E_{eff}$) can be estimated by $E_{eff} = \frac{\sigma_y^2}{2R}$, where R is the modulus of resilience. The modulus of resilience

is the maximum mechanical energy absorption per unit volume prior to yielding and can be calculated by integrating the stress-strain curve from 0 to the elastic limit. In the $E$-$\sigma_y$ space of the Ashby chart, as a material is located closer to the right-bottom corner, it can absorb higher mechanical energy per unit volume. Note that both $CaFe_2As_2$ and $CaKFe_4As_4$ are located in the white space, indicating their superior elastic performance to absorb large amounts of strain energy before yielding (**Figure 4.3(b)**). The average moduli of resilience are 143 MJ/m$^3$ and 291 MJ/m$^3$ for $CaFe_2As_2$ and $CaKFe_4As_4$, respectively (**Figures S. 6 and S. 7 in the supplementary material**). By considering the accurate measurement of stress-strain curve and their reproducibility, our R data are accurate for our micropillar samples. Note that the total strain energy absorption of our specimen are orders of magnitude higher than most engineering materials at both bulk and micrometer scales such as elastomers (~1 MJ/m$^3$), advanced composites (~0.5 MJ/m$^3$), conventional shape memory alloys (~50 MJ/m$^3$), metallic nanopillars (~10 MJ/m$^3$), and superelastic ceramic micropillars (~50 MJ/m$^3$). Semiconductor or ceramic nanowires sometimes show the extremely high modulus of resilience (> 1000 MJ/m$^3$) due to their defect-free structure in their ultra-thin diameter (~50 nm) (**Figure 4.3(b)** and **Supplementary Note 3**). In sum, **Figures 4.3(a)** and **(b)** shows the giant superelasticity of $CaKFe_4As_4$ as well as the great potential of Fe-based pnictide superconductors as a superelastic material.

The giant elastic limit of our materials could make strain-engineering possible. Strain-engineering refers to a significant modification of the properties of solid materials by applying an elastic strain [15]. As a similar material with ours, Co-doped $CaFe_2As_2$, $Ca(Fe_{1-x}Co_x)As_2$, shows the superconductivity switching by application of bi-axial deformation on *ab* plane, which changes the *c/a* ratio of the unit cell and results in the significant shift of superconductivity

region in the temperature-composition phase diagram [58,59]. This strong effect of the *c/a* ratio on superconductivity could extend to our $CaKFe_4As_4$ system, which is also a high temperature superconductor (Tc ≈ 35K), under c-axis uniaxial compression that should change the *c/a* ratio much more significantly.

Previous experimental study with hydrostatic pressure demonstrated that superconductivity of $CaKFe_4As_4$ can be turned off reversibly by the application of hydrostatic pressure of 4GPa when the system undergoes the first hcT transition [29]. That is, the formation of As-As bonds around the Ca atoms is a key process to turn off superconductivity. We recently developed an in-situ cryogenic micro-mechanical testing system (**Supplementary Note 1 in the supplementary material**) and confirmed that the first hcT transition occurs only around 1 GPa under uniaxial compression without failure (**Figure 4.4(a)**). Interestingly, the structural collapse behavior in $CaKFe_4As_4$ is insensitive to a change in temperature, whereas pure and Co-doped $CaFe_2As_2$ exhibits strong temperature sensitivity (**Figure S. 9 in the supplementary material**). These different temperature dependences under uniaxial stress are consistent with the hydrostatic pressure experimental data [29,49].

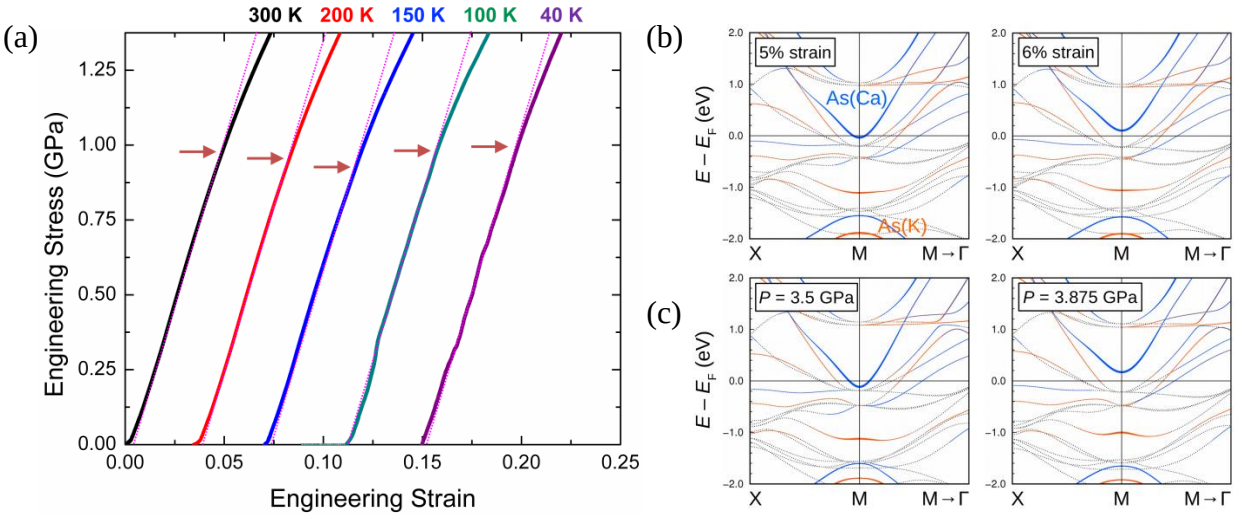

**Figure 4.4. Cryogenic nanomechanical test and DFT simulation near the onset of the first hcT transition.** (a) Engineering stress-strain curves of $CaKFe_4As_4$ at various cryogenic conditions. The arrow indicates the onset of the first hcT transition; Orbital-resolved non-spin-polarized band structure of $CaKFe_4As_4$ under (b) uniaxial and (c) hydrostatic pressure before and after the first hcT (hcT) transition. As $4p_z$ orbitals near the Ca (K) layer are marked by the blue (orange) color. Upon the hcT transition, the antibonding As orbitals shift above the Fermi level. These results show that the change in electronic structure under uniaxial compressive stress (strain) does not differ from that under hydrostatic pressure, implying that the change in electronic properties (here, superconductivity) will be similar under both uniaxial compressive stress and hydrostatic pressure.

The weak temperature dependence of $CaKFe_4As_4$ is not fully understood, yet. However, there are several indirect experimental and computational evidences to explain the different temperature sensitivity between $CaKFe_4As_4$ and $CaFe_2As_2$. Several computational studies suggested that the length between atomic layers in Fe-based pnictides are strongly affected by the distribution of magnetic moments [60]. Interestingly, the magnetic susceptibility of $CaKFe_4As_4$ exhibit the weak temperature dependence [61]. This result implies that the magnetic structure or the spin ordering does not change with temperature, so that the c-axis does not change much with temperature [61]. As a consequence, mechanical properties are insensitive to temperature, too. This scenario is consistent with our experimental data in **Figure. 4.4(a)**.

$CaFe_2As_2$ behaves differently. Magnetic susceptibility decreases with temperature when it is the paramagnetic tetragonal structure [32]. Inelastic neutron scattering measurement showed that as the temperature decreases, the short-range antiferromagnetic ordering increases [62]. At

the same time, the c-axis length decreases substantially with temperature [63]. Thus, magnetism and structure of $CaFe_2As_2$ are more sensitive to temperature than $CaKFe_4As_4$. Interestingly, once $CaFe_2As_2$ becomes antiferromagnetic orthorhombic structure at a temperature below the transition temperature, it becomes magnetically rigid because magnetic ordering does not occur anymore. Then, the c-axis length of $CaFe_2As_2$ does not change much with temperature [63], as that of $CaKFe_4As_4$ does. This is probably why the onset stress of cT transition drastically decrease when $CaFe_2As_2$ is tetragonal but becomes nearly constant once $CaFe_2As_2$ becomes antiferromagnetic orthorhombic structure under hydrostatic pressure [49] and uniaxial stress (**Supplementary Figure S. 9c** shows the weak temperature dependence between 40 K and 100 K.).

Our DFT simulation confirms that the formation of As-As bonds and the change in electronic structure under uniaxial compression are nearly similar to those under hydrostatic compression (**Figures 4.4(b)** and **4.4(c)**). A similar situation has been found in $CaFe_2As_2$ when comparing the electronic structure under uniaxial and hydrostatic stress [48]. These results make sense because the deformation along c-axis is much more significant than that along a- and b-axes direction even under hydrostatic pressure due to the large elastic compliance and As-As bond formation along c-axis. Under the assumption that the origin of superconductivity is linked to the electronic and magnetic properties of the system, these results suggest that superconductivity could also be switched off by inducing the first hcT transition (the formation of As-As bond around a Ca atom) under uniaxial compression. Therefore, our experimental and computational results strongly suggest that superconductivity of $CaKFe_4As_4$ could be reliably turned on and off at the onset of the first hcT transition (~1 GPa) without any fracture or plastic deformation, even under uniaxial compression. By considering the presence of the onset and offset of the first hcT transition in

Stage II, $CaKFe_4As_4$ would begin to show the finite resistivity at the uniaxial stress above ~1GPa and would become completely non-superconducting above ~2.7GPa (**Figure 4.5**). Note that our result does not provide the direct evidence of superconductivity switching, yet. Resistivity measurement or permanent magnetic field measurement would be necessary under uniaxial compression to prove our prediction. By considering all experimental and computational data, superconductivity switching is likely to occur even under uniaxial deformation. Thus, electrical and magnetic measurements at the small length scales are considered as the next step we would like to pursue.

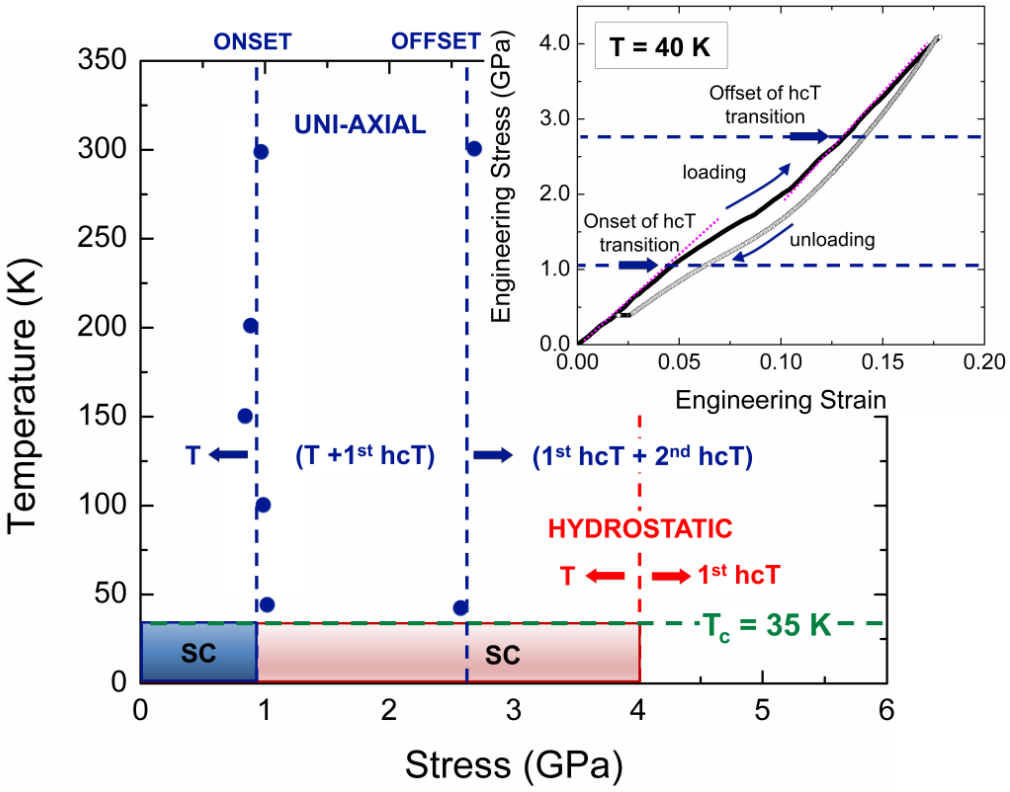


**Figure 4.5. Prediction of superconductivity phase diagram in temperature-stress space under uniaxial compression.** At both T= 300 K and 40 K, the hcT transition begins at around 1 GPa of uniaxial stress and complete at around 2.7 GPa. The inset is the loading-unloading curve

of $CaKFe_4As_4$ at 40 K, which still shows complete recovery even after ~17% of elastic deformation. The onset stress (~1 GPa) is only 20% of the yield strength (~5 GPa), implying that superconductivity switching would be repeatedly done without failure or even without significant fatigue damage. SC stands for superconductivity. Blue broken lines indicate the onset and offset stresses of the 1st hcT transition under uniaxial compression. Red broken line indicates the onset of 1st hcT transition under hydrostatic compression [29].

## 4.4. Concluding remarks

Strain-engineering is usually possible when a material can absorb a large amount of strain without permanent deformation. Hydrostatic stress or bi-axial stress would often be regarded as a convenient way to see the strain effect because the maximum shear stress is zero or too low to cause plastic deformation or fracture. Thus, it is really rare to see substantial strain effect on material properties in brittle intermetallic compounds, particularly under a uniaxial strain condition, because the shear stress is usually sufficiently high to cause brittle failure too easily. In contrast, the structural transition in our intermetallic compounds, $CaFe_2As_2$ and $CaKFe_4As_4$, through formation of covalent bonds leads to a giant uniaxial elastic strain, which can cause substantial changes in their electronic and magnetic properties before failure, even under uniaxial mechanical loading. The uniaxially-loaded superconductivity switching capability may never be imagined in conventional oxide-base superconductors, which have no superelasticity mechanism and easily shatter at a small elastic limit under uniaxial stress due to their extreme brittleness. In addition, our previous experimental studies also demonstrated that $CaFe_2As_2$ could exhibit shape memory effect and thermal actuation under cryogenic environments and have a strong potential for cryogenic actuation technology for space exploration [27]. Some groups of $CaKFe_4As_4$

structured intermetallic compounds are regarded as quantum materials that exhibit unique electronic and magnetic properties [50]. More interestingly, $ThCr_2Si_2$-type and its related structures have been considered to be one of the most populous of all crystal structure types [64]. There are nearly 2500 $ThCr_2Si_2$-structured intermetallic compounds [25]. Even non-FeAs-based compounds demonstrate the same superelasticity mechanism [35]. If we consider their hybrid structure, such as $CaKFe_4As_4$, there could be some groups of similar superelastic intermetallic compounds [39,43]. Also, their microstructure and composition can easily be tuned through heat treatment and solid solutionization [65]. Thus, our observation can be extended to search for a large group of superelastic and strain-engineerable functional materials. Computer simulations with machine-learning could be extremely beneficial to rapidly identify compounds with these desired properties [66,67]. In sum, our discovery of superelasticity and strain-engineerability under "uniaxial" mechanical loading will lead to a grand research opportunity in materials science, solid-state physics, device engineering, and computer simulations.

## 4.5.Information about Supplementary materials

See **Appendix III** for the supplementary materials. Also, find videos at (https://doi.org/10.1063/1.5087279#suppl)

**Supplementary Movie 1. Uniaxial deformation of $CaKFe_4As_4$ until fracture occurs.** Total fracture strain is about 17% (See also the snapshot in Fig. 2(a))

**Supplementary Movie 2. Cyclic compression test of $CaKFe_4As_4$ (20 cycles).** The cyclic compression strain is about 11%, and this large deformation is recoverable. The stress-strain data and video snapshots are available in Fig. S2.

4.6.References


[1] C. R. Barrett, A. S. Tetelman, & W. D. Nix, The Principles of Engineering Materials, Prentice-Hall, New Jersey, USA (1973).
[2] M. Russell, Adv. Eng. Mater. **5**, 629 (2003).
[3] Y. Tanaka, Y. Himuro, R. Kainuma, Y. Sutou, T. Omori, K. Ishida, Science **327**, 1488 (2010).
[4] K. Otsuka, H. Sakamoto, K. Shimizu, Acta Metall. **27**, 585 (1979).
[5] D. M. Norfleet, P. M. Sarosi, S. Manchiraju, M. F.-X. Wagner, M. D. Uchic, P. M. Anderson, M. J. Mills, Acta Mater. **57**, 3549 (2009).
[6] R. Kainuma, Y. Imano, W. Ito, Y. Sutou, H. Morito, S. Okamoto, O. Kitakami, K. Oikawa, A. Fujita, T. Kanomata, K. Ishida, Nature **439**, 957 (2006).
[7] Z. H. Liu, M. Zhang, Y. T. Cui, Y. Q. Zhou, W. H. Wang, G. H. Wu, Appl. Phys. Lett. **82**, 424 (2003).
[8] Y. Sutou, Y. Imano, N. Koeda, T. Omori, R. Kainuma, K. Ishida, Appl. Phys. Lett. **85**, 4358 (2004).
[9] M. D. Uchic, D. M. Dimiduk, J. N. Florando, W. D. Nix, Science **305**, 986 (2004).
[10] J. R. Greer, W. C. Oliver, W. D. Nix, Acta Mater. **53**, 1821 (2005).
[11] C. A. Volkert, E. T. Lilleodden, Phil. Mag. **86**, 5567 (2006).
[12] M. D. Uchic, P. A. Shade, D. M. Dimiduk, Ann. Rev. Mater. Res. **39**, 361 (2009).
[13] J. R. Greer, J. T. M. de Hossen, Prog. Mater. Sci. **56**, 654 (2011).
[14] O. Kraft, P. A. Gruber, R. Mönig, D. Weygand, Ann. Rev. Mater. Res. **40**, 293 (2010).
[15] T. Zhu, J. Li, Prog. Mater. Sci. **55**, 710 (2010).
[16] J. Weiss, L. Girard, F. Gimbert, D. Amitrano, D. Vandembroucqe, Proc. Nat. Acad. Sci. **111**, 6231 (2014).
[17] J. M. Wheeler, R. Raghavan, J. Wehrs, Y. Zhang, R. Erni, J. Michler, Nano Lett. **16**, 812 (2016).
[18] L. Graham-Brady, Int. J. Solid Struc. **47**, 2398 (2010).
[19] S. Wang, Z. Shan, H. Huang, Adv. Sci. **4**, 1600332 (2017).
[20] S.-W. Lee, D. Mordehai, D. J. Srolovitz, W. D. Nix, E. Rabin, J. Mater. Res. **26**, 1653 (2011)
[21] H. Bei, S. Shim, E. P. George, M. K. Miller, E. G. Herbert, G. M. Pharr, Scripta Mater. **57**, 397 (2007).
[22] J. Wesler, J. L. Hoyt, J. F. Gibbons, IEEE Electron Device Lett. **15**, 100 (1994).
[23] Y. Kamihara, H. Hiramatsu, M. Hirano, R. Kawamura, H. Yanagi, T. Kamiya, H. Hosono, J. Am. Chem. Soc. **128**, 10012 (2006).
[24] J. Paglione, R. L. Greene, Nature Physics **6**, 645 (2010).
[25] M. Shatruk, J. Solid. State. Chem. **272**, 198 (2019).
[26] P. C. Canfield, S. L. Bud'ko, N. Ni, A. Kreyssig, A. I. Goldman, R. J. McQueeney, M. S. Torikachvili, D. N. Argyriou, G. Luke, W. Yu, Physica C: Superconductivity **469**, 404 (2009).

[27] J. T. Sypek, H. Yu, K. J. Dusoe, G. Drachuck, H. Petal, A. M. Giroux, A. I. Goldman, A. Kreyssig, P. C. Canfield, S. L. Bud'ko, C. R. Weinberger, S.-W. Lee, Nature Comm. **8**, 1083 (2017).
[28] J. T. Sypek, C. R. Weinberger, S. Vijayan, M. Aindow, P. C. Canfield, S.-W. Lee, Scripta Materialia **141**, 10 (2017).
[29] U. S. Kaluarachchi, V. Taufour, A. Sapkota, V. Borisov, T. Kong, W. R. Meier, K. Kothapalli, B. G. Ueland, A. Kreyssig, R. Valentí, R. J. McQueeney, A. I. Goldman, S. L. Bud'ko, P. C. Canfield, Phys. Rev. B. **96**, 140501(R) (2017).
[30] R. Peierls, Proc. Phys. Soc. London, **52**, 34, (1940).
[31] F. R. N. Nabarro, Proc. Phys. Soc. London **59**, 256 (1947).
[32] N. Ni, S. Nandi, A. Kreyssig, A. I. Goldman, E. D. Mun, S. L. Bud'ko, P. C. Canfield, Phys. Rev. B **78**, 014523 (2008).
[33] W. R. Meier, T. Kong, S. L. Bud'ko, P. C. Canfield, Phys. Rev. Mater. **1**, 013401 (2017).
[34] W. C. Oliver, G. M. Pharr, J. Mater. Res. **7**, 1564 (1992).
[35] I. N. Bakst, K. J. Dusoe, G. Drachuk, J. R. Neilson, P. C. Canfield, S.-W. Lee, C. R. Weinberger, Acta Mater. **160**, 224 (2018).
[36] P. Blöchl, Phys. Rev. B **50**, 17953 (1994).
[37] G. Kresse, J. Furthmüller, Phys. Rev. B **54**, 11169 (1996).
[38] J. P. Perdew, K. Burke, M. Ernzerhof, Phys. Rev. Lett. **77**, 3865 (1996).
[39] V. Borisov, P. C. Canfield, R. Valentí. Phys. Rev. B **98**, 064104 (2018).
[40] K. Koepernik, H. Eschrig, Phys. Rev. B **59**, 1743 (1999).
[41] F. Lekien, J. Marsden, International Journal for Numerical Methods in Engineering **63**, 455 (2005).
[42] https://github.com/danielguterding/fplowannierdensity
[43] Iyo, K. Kawashima, T. Kinjo, T. Nishio, S. Ishida, H. Fujihisa, Y. Gotoh, K. Kihou, H. Eisaki, Y. Yoshida, J. Am. Chem. Soc. **138**, 3410 (2016).
[44] Lai, Z. Du, C. L. Gan, C. A. Schuh, Science **27**, 1505 (2013).
[45] C. P. Frick, B. G. Clark, A. S. Schneider, R. Maaß, S. Van Petegem, H. Van Swygenhoven, Scripta Mater. **62**, 492 (2010).
[46] R. Hoffmann, C. Zheng, J. Phys. Chem. **89**, 4175 (1985).
[47] I. N. Bakst, J. T. Sypek, S.-W. Lee, J. R. Neilson, C. R. Weinberger, Comp. Mat. Sci. **150**, 86 (2018).
[48] M. Tomić, R. Valentí, H. O. Jeschke, Phys. Rev. B **85**, 094105 (2012).
[49] A. I. Goldman, A. Kreyssig, K. Prokeš, D. K. Pratt, D. N. Argyriou, J. W. Lynn, S. Nandi, S. A. J. Kimber, Y. Chen, Y. B. Lee, G. Samolyuk, J. B. Leão, S. J. Poulton, S. L. Bud'ko, N. Ni, P. C. Canfield, B. N. Harmon, R. J. McQueeney, Phys. Rev. B **79**, 024513 (2009).
[50] W. R. Meier, Q.-P. Ding, A. Kreyssig, S. L. Bud'ko, A. Sapkota, K. Kothapalli, V. Borisov, R. Valentí, C. D. Batista, P. P. Orth, R. M. Fernandes, A. I. Goldman, Y, Furukawa, A. E. Böhmer, P. C. Canfield, npj Quantum Mater. **3**, 5 (2018).
[51] T. Omori, R. Kainuma, Nature **502**, 42 (2013)
[52] J. Ye, R. K. Mishra, A. R. Pelton, A. M. Minor, Acta Mater. **58**, 490 (2010).
[53] C. J. Lee, J. C. Huang, T. G. Nieh, Appl. Phys. Lett. **91**, 161913 (2007).
[54] L. R. Meza, S. Das, J. R. Greer, Science **345**, 1322 (2014).
[55] J. Bauer, A. Schroer, R. Schwaiger, O. Kraft, Nature Mater. **15**, 438 (2016).
[56] J. J. Kruzic, Adv. Eng. Mater. **18**, 1308 (2016).

[57] M. F. Ashby, Material Property Charts. In Materials Selection in Mechanical Design, 4th ed. Oxford, UK (2011).
[58] E. Böhmer, A. Sapkota, A. Kreyssig, S. L. Bud'ko, G. Drachuck, S. M. Saunders, A. I. Goldman, P. C. Canfield, Phys. Rev. Lett. **118**, 107002 (2017).
[59] Fente, A. Correa-Orellana, A. E. Böhmer, A. Kreyssig, S. Ran, S. L. Bud'ko, P. C. Canfield, F. J. Mompean, M. García-Hernández, C. Munuera, I. Guillamón, H. Suderow, Phys. Rev. B **97**, 014505 (2018).
[60] T. Yildrim, Phys. Rev. Lett. **102**, 037003 (2009)
[61] W. R. Meier, T. Kong, U. S. Kaluarachchi, V. Taufour, N. H. Jo, G. Drachuck, A. E. Böhmer, S. M. Saunders, A. Sapkota, A. Kreyssig, M. A. Tanatar, R. Prozorov, A. I. Goldman, F. F. Balakirev, A. Gurevich, S. L. Bud'ko, P. C. Canfield, Phys. Rev. B **94**, 064501 (2016).
[62] S. O. Diallo, D. K. Pratt, R. M. Fernandes, W. Tian, J. L. Zarestky, M. Lumsden, T. G. Perring, C. L. Broholm, N. Ni, S. L. Bud'ko, P. C. Canfield, H.-F. Li, D. Vaknin, A. Kreyssig, A. I. Goldman, R. J. McQueeney, Phys. Rev. B **81** 214407 (2010).
[63] S. L. Bud'ko, S. Ran, P. C. Canfield, Phys. Rev. B **88**, 064513 (2013).
[64] W. B. Pearson, J. Solid State Chem. **56**, 278 (1985).
[65] S. Ran, S. L. Bud'ko, D. K. Pratt, A. Kreyssig, M. G. Kim, M. J. Kramer, D. H. Ryan, W. N. Rowan-Weetaluktuk, Y. Furukawa, B. Roy, A. I. Goldman, P. C. Canfield, Phys. Rev. B **83**, 144517 (2011).
[66] P. De Luna, J. Wei, Y. Bengio, A. Aspuru-Guzik, E. Sargent, Nature **552**, 23 (2017).
[67] Y. Liu, T. Zhao, W. Ju, S. Shi, J. Materiomics **3**, 159 (2017).

# Chapter 5. Summary and future work

## 5.1. Summary of this dissertation

Thermal environment has been considered as one of the most important extreme conditions that affect mechanical properties of materials. Particularly, the mechanical properties at a low temperature has been extensively studied due to their importance in space exploration or marine engineering. This dissertation has focused on the mechanical properties of micron-sized materials at as low temperature as 37 K.

In Chapter 2, Ductile-to-brittle transition (DBT) of body-centered-cubic (bcc) metals was reported. DBT usually occurs due to the low mobility of screw dislocation at a low temperature. The DBT behavior of micron-sized bcc metals could be different from that of their bulk counterparts because of the different plasticity mechanism, the intermittent operation of dislocation sources at the micrometer scale. My results showed the DBT of micron-sized niobium. Fractography showed perfect plasticity failure at 298K but brittle fracture at 100 and 56K. Post-mortem transmission electron microscopy suggested that the DBT at the micrometer-scale would occur via the dynamic annihilation and nucleation of dislocation sources instead of the reduction of screw dislocation mobility.

In Chapter 3, the temperature dependence of dislocation self-multiplication in single crystalline bcc metal nanopillars was reported. Recent works in computations and experiments revealed that dislocations in bcc are more easily multiplied in bcc structure than face-centered-cubic (fcc) structure. My results revealed the distinctive change in critical stress of multiplication with temperature, implying that surface controlled multiplication is dependent of dislocation mobility as well as dynamic cross-slips.

In Chapter 4, the superelasticity of $CaKFe_4As_4$ was reported. Many intermetallic compounds often exhibit superior physical and chemical properties due to their unique atomic arrangements and crystal structures, but their practical applications have been significantly limited because most intermetallic compounds are extremely brittle and are not able to absorb strain energy high enough to sustain its structure. Here, $ThCr_2Si_2$-system has potential usage of high temperature superconductivity. I reported the experimental result of giant compressible strain, 13~17% under uni-axial compression along c-axis in single crystalline $CaKFe_4As_4$. The density functional theory from a collaboration showed that this unusually large elastic axial compressibility results from the half-collapsed tetragonal phase transition, which is induced by As-As atomic bond formation and magnetic moment collapse, and significant local compliance. All these processes are manifested to be fully reversible upon unloading in cyclic tests. Furthermore, this study showed the possibility of strain engineering, for instance, superconductivity switching even under uni-axial mechanical loading.

## 5.2. Future work

Firstly, it will be valuable to hone in the temperature control towards liquid Helium temperature, which is 4 K. Even though environmental effects on materials properties are getting enormous interests, there are a few groups that are investigates the effects of cryogenic temperature. It is mainly because of the difficulties in the cryogenic set-up, compared to that of high temperature. In our group, the custom-built cryogenic testing system has enabled a lot of interesting researches but can be improved further. Despite the temperature of the cold finger reaching to 4 K with liquid Helium, the current minimum temperature of the sample stage that we can obtain is around 40 K. The connection between the cold finger and the sample stage is a

shielded copper braid. The sources of heat can be electron beam radiation, the diffusion pump, and etc. It will be worthwhile to check each component separately. Some elements can show superconductivity at ambient pressure at liquid Helium temperature. For example, Niobium`s superconducting transition temperature is around 10 K. Silicon`s is around 8 K. Lanthanum`s 6K. Vanadium`s is around 5 K [1]. Additionally, as discussed in Chapter 5, there are nearly 2,500 $ThCr_2Si_2$-structured intermetallic compounds that can be studied [2], whose transition temperatures are higher than 4 K as well. Thus, having the capability to cool down the system close to 4 K will unlock the enormous opportunities to explore the coupling between mechanical properties and superconductivity.

Secondly, it will be useful to study the effect of dislocation density on DBT at small scales. As discussed in the Chapter 2, the evolution of dislocations can be affected by various factors, including sample size and temperature. If the density of dislocation is high, it is expected that the interaction between dislocations will significantly influence the mobility, nucleation of dislocations, and consequent DBT process. By applying a wide range of pre-strains to the sample, the density of dislocations can be controlled and studied to understand the DBT at small scale better.

Thirdly, as discussed in Chapter 5, the change in c-axis of $ThCr_2Si_2$-structured intermetallic compounds can trigger their unique behaviors. If the point defects (e.g. vacancies, interstitial/substitutional impurities) are incorporated or microstructures are modified to induce residual strain, they can affect the lattice structure locally and/or globally. Thus, it will be interesting to change the condition of synthesis of the compounds so as to strategically engineer their c-axes and, consequently, superelasticity.

Lastly, a diamond tip with a smart design that allows uni-axial compression and tension tests can be made. Currently, tip-changing is trained to new members of the group by their peers. Generally, spending more time in the lab increases the level of the confidence and/-or proficiency of tip-changing. However, it is still possible to make mistakes and damage the machine (currently NanoFlip$^{TM}$). For example, one can forget to pin the tip before removing the head, drop the head while transporting it, or over-tighten the tip. Any one of the examples can seriously damage the machine, which will cost money and time. Thus, to minimize the chance of damaging the machine, it is the best to decrease the number of events that require hands-on-the-machine. A smartly designed tip that can perform uni-axial compression and tension tests will increase the efficiency of the work as well as decrease the risk of damaging the machine.

## 5.3. References

[1] Hamlin, J. J. "Superconductivity in the metallic elements at high pressures." *Physica C: Superconductivity and its Applications* 514 (2015): 59-76.
[2] Hoffmann, Roald, and Chong Zheng. "Making and breaking bonds in the solid state: the ThCr2Si2 structure." *The Journal of Physical Chemistry* 89.20 (2002): 4175-4181.

## APPENDIX I: PUBLICATIONS

1. Song, G., Aragon, N. K, Ryu, I.,& Lee, S. W. “Low Temperature Failure Mechanism of [001 ] Niobium Micropillars under Uniaxial Tension”. – Invited in Focus Issue on *Advanced Nano mechanical Testing - Journal of Materials Research* (2020)
2. Maita, J. M., Song, G., Colby, M., & Lee, S. W. “Atomic arrangement and mechanical prope rties of chemical-vapor-deposited amorphous boron”. Materials & Design, 108856. (2020)
3. Song, G., & Lee, S. W. “Effects of Temperature on Surface-Controlled Dislocation Multiplic ation in Body-Centered-Cubic Metal Nanowires”. *Computational Materials Science* (2019)
4. Song, G., Borisov, V., Meier, W., Xu, M., Dusoe, K., Sypek, J., Valentí, R., Canfield, P., & Lee, S. W. “Ultrahigh Elastically Compressible and Strain-Engineerable Intermetallic Compo unds Under Uniaxial Mechanical Loading”. *APL Materials* (2019)
5. Manthina, V., Song, G., Singh, P., & Mahapatra, M. K. “Silica-free sealing glass for sodium-beta alumina battery”. *International Journal of Applied Ceramic Technology* (2019)
6. Song, G., Kong, T., Dusoe, K. J., Canfield, P. C., & Lee, S. W. “Shear localization and size-d ependent strength of $YCd_6$ quasicrystal approximant at the micrometer length scale”. *Journal of Materials Science* (2018)
7. Song, G. “Study of Seal Glass for Sodium Sulfur Batteries”. – UConn M.S. dissertation (201 6)

## APPENDIX II: COPYRIGHT

Chapter 2. Submitted to Journal of Materials Research as an invited paper at the focused issue "Advanced Nanomechanical Testing" (**Cambridge University Press)**.

- For authors and others, Green OA and social sharing policy for journals
- That **preprints can be archived anywhere at any time**, in the same way as submitted manuscripts, and that **theses or dissertations can also be considered to be preprints**.

Chapter 3. **Elsevier**

For Personal use, Authors can use their articles, in full or in part, for a wide range of scholarly, non-commercial purposes as outlined below:

- Inclusion in a thesis or dissertation (provided that this is not to be published commercially)

These rights apply for all Elsevier authors who publish their article as either a subscription article or an open access article. In all cases we require that all Elsevier authors always include a full acknowledgement and, if appropriate, a link to the final published version hosted on Science Direct.

Chapter 4. **AIP Publishing**

Authors do **not** need permission from AIP Publishing to:

- Reuse your own AIP Publishing article in your thesis or dissertation (please format your credit line: "Reproduced from [FULL CITATION], with the permission of AIP Publishing")

## APPENDIX III: Supplementary materials for Chapter 4

**(**Reproduced from "Song, G, et al., *APL Materials* 7.6 (2019): 061104", with the permission of AIP Publishing)

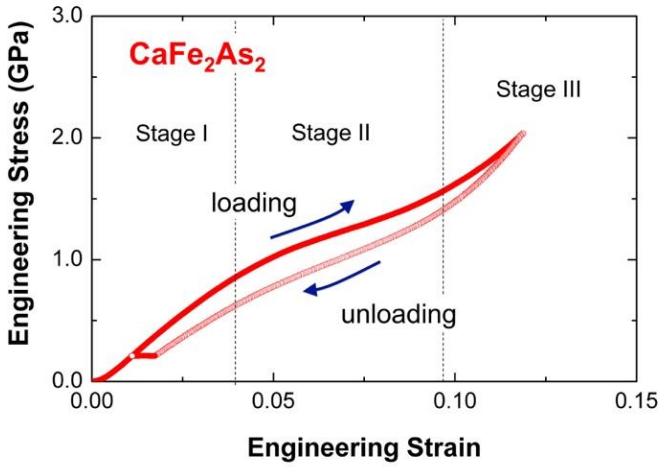


**Figure S. 1 Experimental loading-unloading data of $CaFe_2As_2$.** Loading-unloading data of $CaKFe_4As_4$ are also available in Fig. 4(b). Note that both materials exhibit exceptionally large recoverable strains.

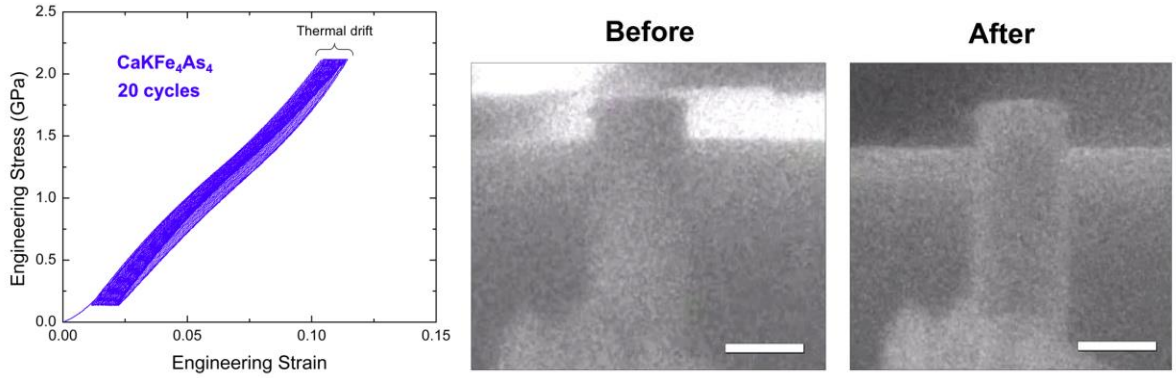


**Figure S. 2 Experimental loading-unloading cyclic stress-strain curve.** 20 cycles of loading-unloading were applied to $CaKFe_4As_4$. The slight shift of stress-strain data over time results from thermal drift, which is one of the common issues associated with long-time nanomechanical testing and is not associated with plastic deformation. Two SEM images below confirm no difference in geometry after 20 loading-unloading cycles (the scale bar, 1.5μm). *In-situ* video of this cyclic deformation is also available as the Supplementary Movie 2.

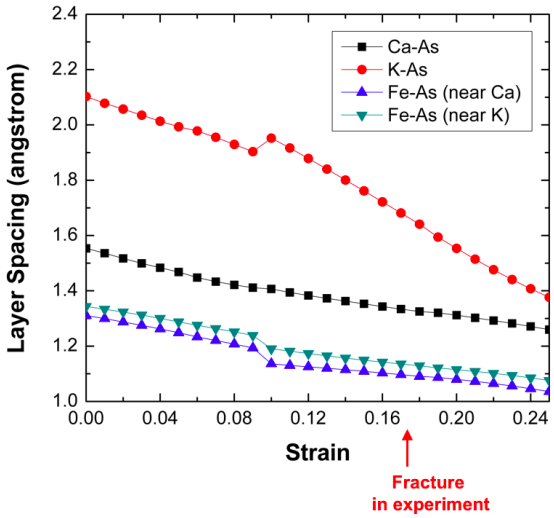


**Figure S. 3 DFT data of change in layer spacing of $CaKFe_4As_4$ under uniaxial compression.** The layer spacing between K and As layers is decreased the most significantly under uniaxial compression, implying that the region between these two layers are elastically compliant. Based on our calculation, the elastic deformation between As layers around the K atom is responsible for 36% of the total elastic strain. The interlayer distance of As-As layer around a K atom (twice of K-As layer spacing above) is 3.2816Å near the elastic limit. By considering that it is 4.205Å before compression, its change contributes to (4.205Å -3.2816Å )/(12.6206 Å , initial c-length) ≈ 0.073 of strain (~41% of the total elastic limit), which is remarkably high.

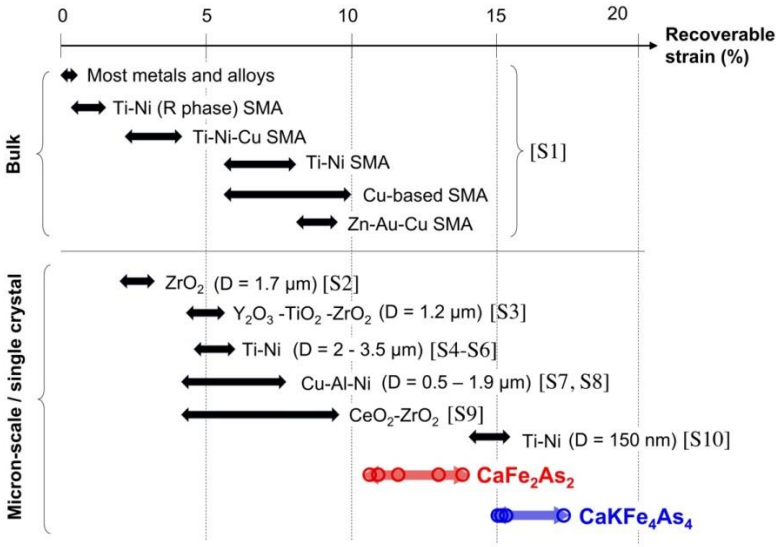


**Figure S. 4 Elastic limit of superelastic materials at different length scales with reference numbers (Figure 4.3(a))**. The references are available in Supplementary Note 1.

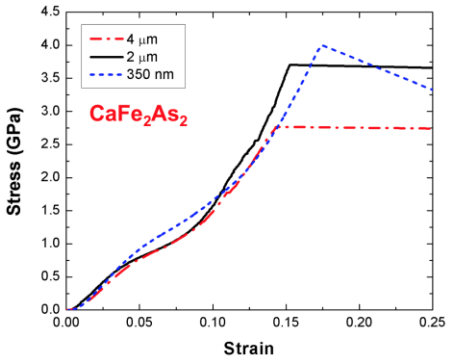


**Figure S. 5 Size effect on stress-strain data of $CaFe_2As_2$ micropillars with different diameters.** Smaller micropillars exhibit higher yield strength as well as a larger elastic limit. The origin of size effect could be related to the weakest-link mechanism that is related to the statistics of defect distribution; the larger the sample dimension is, the more easily the fracture occurs. FIB damage could also strengthen the surface, leading to larger elastic strain.

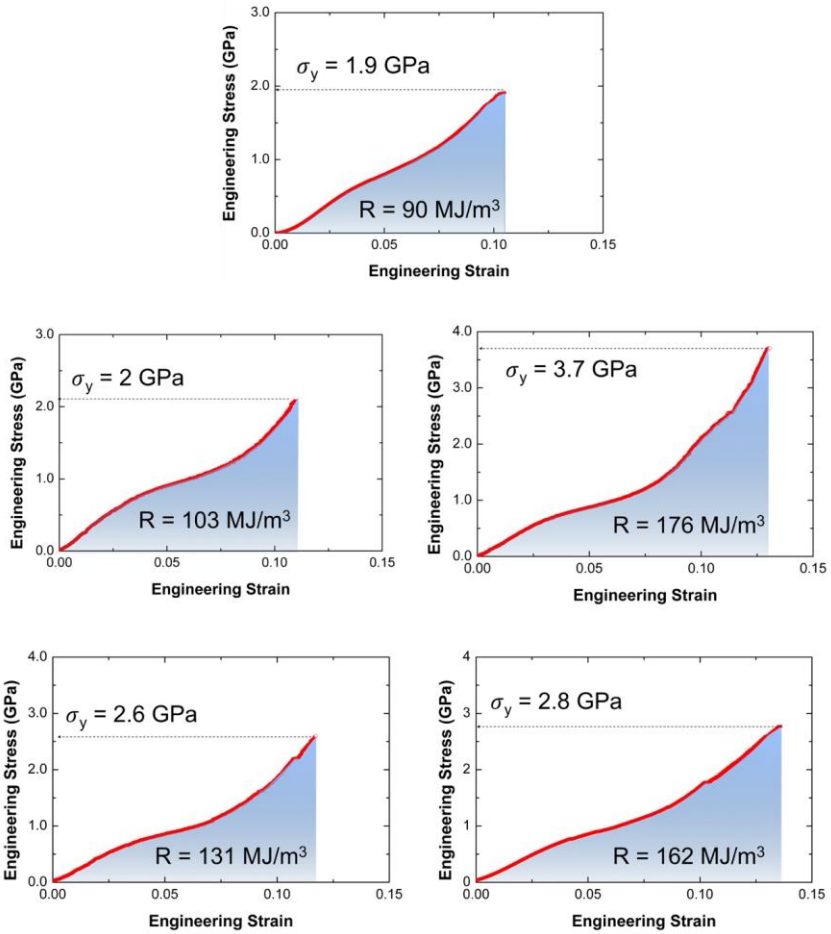


**Figure S. 6 Stress-strain data of $CaFe_2As_2$ with the modulus of resilience and yield strength.** Modulus of resilience is obtained by numerical integration of the stress-strain curve between 0 and the elastic limit in strain.

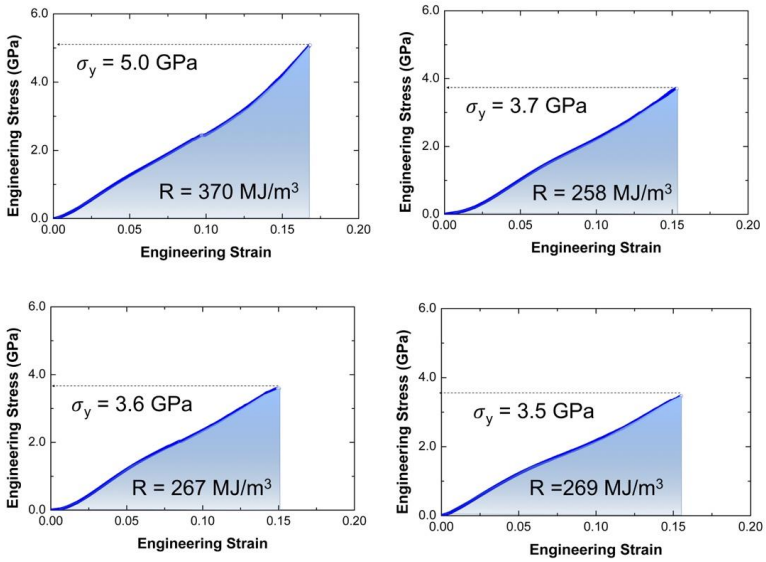


**Figure S. 7 Stress-strain data of CaKFe4As4 with the modulus of resilience and yield strength.** Modulus of resilience is obtained by numerical integration of the stress-strain curve between 0 and the elastic limit in strain.

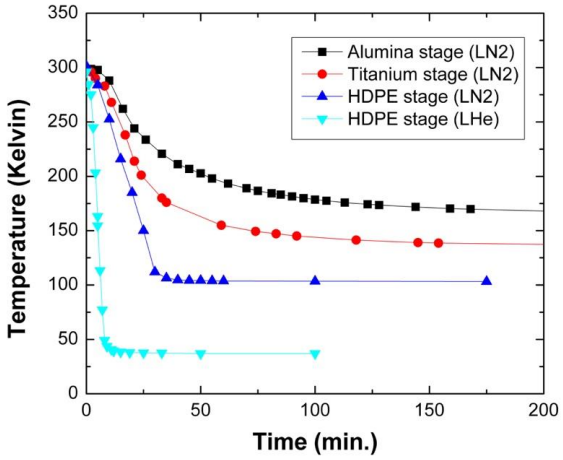


**Figure S. 8 The temperature profile of sample stage with different stage materials.** Density-Poly-Ethylene (HDPE) shows the best cooling performance due to its lower thermal conductivity (~0.49 $Wm^{-1}K^{-1}$) than alumina (~30 $Wm^{-1}K^{-1}$) and titanium (~20 $Wm^{-1}K^{-1}$).

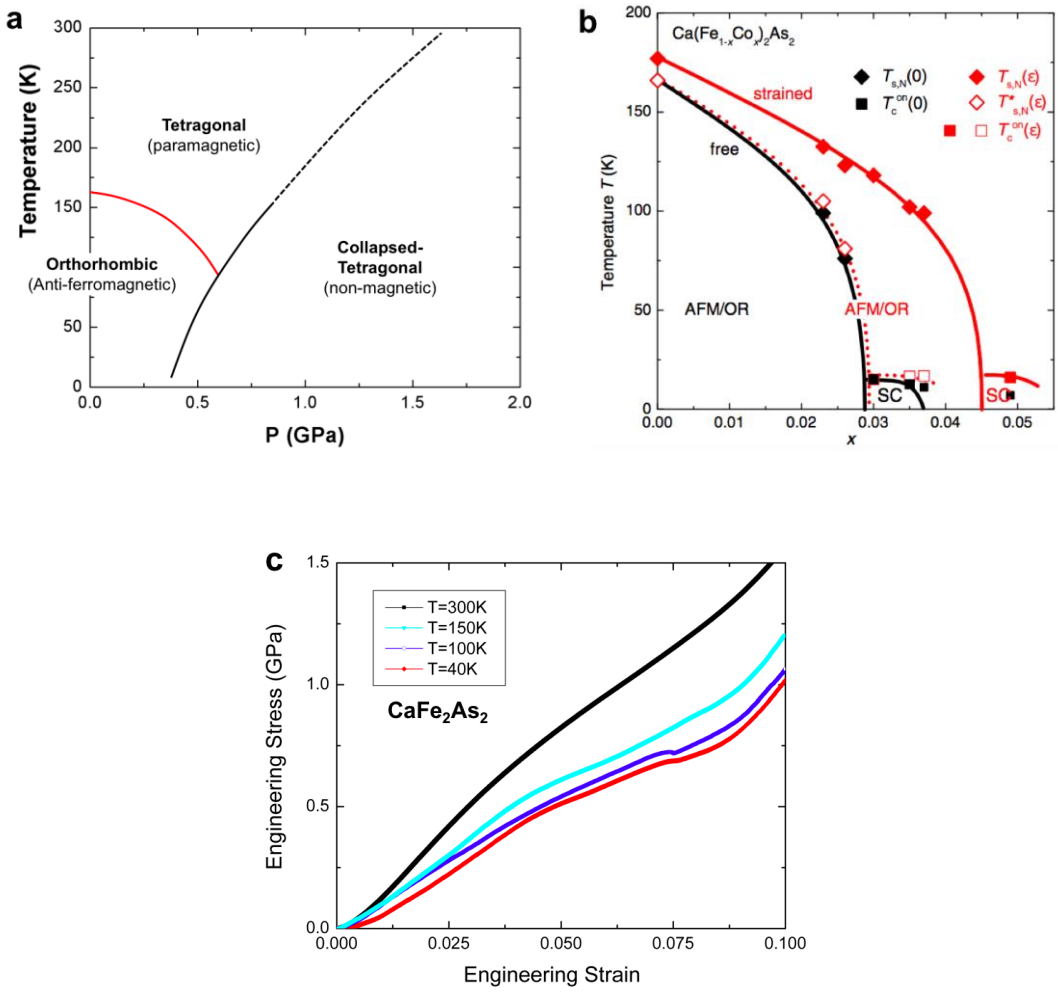


**Figure S. 9 The temperature sensitivity of $CaFe_2As_2$ and $Ca(Fe_{1-x}Co_x)As_2$.** (a) Temperature-pressure phase diagram of $CaFe_2As_2$ under hydrostatic pressure (Reprinted with the permission of J.T. Sypek *et al*. [19], copyright 2017, Springer Nature); (b) Temperature-composition phase diagram of $Ca(Fe_{1-x}Co_x)As_2$ (Reprinted with the permission of A.E. Böhmer *et al*. [36], copyright 2017, American Physics Society); (c) (This study) temperature-dependent engineering stress-strain curve of $CaFe_2As_2$ under uniaxial compression. In contrast to the temperature insensitivity of stress-strain data of $CaKFe_4As_4$ (Figure 4.4(a)), stress-strain data of $CaFe_2As_2$ is strongly dependent on temperature. As the temperature decreases, the cT transition occurs at a lower stress. This result is consistent with the result of the hydrostatic pressure experiment in Ref. 19 and 26.

**Supplementary Note 1: References of Figure 3 in the main text**

The following is the references of materials in Fig. 3 in the main text. Reference number is included in Fig. S4.


[S1]T. Omori, R. Kainuma, Nature 502, 42 (2013).
[S2]Z. Du, X. M. Zeng, Q. Liu, A. Lai, S. Amini, A. Miserez, C. A. Schuh, C. L. Gan, Scripta Mater. **101**, 40 (2015).
[S3]X. M. Zeng, A. Lai, C. L. Gan, C. A. Schuh, Acta Mater. **116**, 124 (2016).
[S4]C. P. Frick, B. G. Clark, A. S. Schneider, R. Maaß, S. Van Petegem, H. Van Swygenhoven, Scripta Mater. **62**, 492 (2010).
[S5]C. P. Frick, S. Orso, E. Arzt. Acta Mater. **55**, 3845 (2007).
[S6]J. Pfetzing-Micklich, R. Ghisleni, T. Simon, C. Somsen, J. Michler, G. Eggeler, Mater Sci Eng: A **538**, 265 (2012).
[S7]J. San Juan, M. L. Nó, C. A. Schuh, Acta Mater. **60**, 4093 (2012).
[S8]J. San Juan, M. L. Nó, C. A. Schuh, Adv Mater. **20**, 272 (2008).
[S9]Lai, Z. Du, C. L. Gan, C. A. Schuh, Science **341**,1505 (2013).
[S10]J. Ye, R. K. Mishra, A. R. Pelton, A. M. Minor, Acta Mater. **58**, 490 (2010).

**Supplementary Note 2: Modulus of Resilience of various nano-sized materials**

| Material | | | σ (GPa) | E (GPa) | R ($MJ/m^3$) | Reference |
|---|---|---|---|---|---|---|
| Metallic Nanopillar | BCC | V | 2.45 | 128 | 23.5 | [S11] |
| | | Nb | 0.76 | 105 | 2.7 | [S12] |
| | | Mo | 3.96 | 329 | 23.8 | [S13] |
| | | Nb | 1.15 | 105 | 6.3 | [S13] |
| | | Ta | 2.77 | 186 | 20.6 | [S13] |
| | | W | 2.85 | 411 | 9.9 | [S13] |
| | | Ta | 1.49 | 186 | 6.0 | [S11] |
| | HCP | Ti | 3.27 | 116 | 46.0 | [S14] |
| | | Ti | 3.28 | 116 | 46.3 | [S14] |
| | | Mg | 0.58 | 45 | 3.7 | [S15] |
| | | Mg | 0.36 | 45 | 1.4 | [S16] |
| | FCC | Cu | 2.77 | 120 | 32.0 | [S17] |
| | | Cu | 2.82 | 120 | 33.2 | [S18] |
| | | Au | 1.06 | 79 | 7.1 | [S19] |
| | | Au | 1.36 | 79 | 11.7 | [S20] |
| Nanowire | | Si | 18.5 | 161 | 1064 | [S21] |
| | | Si | 20 | 125 | 1600 | [S22] |
| | | Si | 12.2 | 188 | 397 | [S23] |
| | | Ge | 18 | 106 | 1530 | [S24] |
| | | Ge | 15 | 200 | 563 | [S25] |
| | | ZnO | 9.5 | 153 | 295 | [S26] |
| | | ZnO | 12.1 | 173 | 424 | [S27] |
| | | ZnS | 0.37 | 5 | 15 | [S28] |
| | | GaAs | 5.4 | 77 | 189 | [S29] |
| | | InAs | 5 | 50 | 250 | [S30] |

| | | | | | |
|---|---|---|---|---|---|
| | GaN | 3.1 | 124 | 39 | [S31] |
| | $WS_2$ | 16 | 114 | 1120 | [S32] |
| | $VO_2$ | 5.2 | 137 | 99 | [S33] |
| | $\alpha$-$Al_2O_3$ | 48.8 | 460 | 2586 | [S34] |
| | SiC | 35 | 500 | 1225 | [S35] |
| | SiC | 53.4 | 534 | 2670 | [S36] |
| | Au | 8 | 80 | 400 | [S37] |
| | Au | 9.8 | 50 | 960 | [S38] |
| | Cu | 5.8 | 81 | 209 | [S39] |
| | Cu nanotwin | 2.12 | 42 | 53 | [S40] |
| | Ni | 5 | 14 | 865 | [S41] |
| | Nb | 1.8 | 45 | 36 | [S42] |
| | Ag | 4.8 | 120 | 96 | [S43] |
| | Co | 2.04 | 95 | 22 | [S44] |

**Table III.1 Modulus of Resilience of various nano-sized materials**


[S11]S. M. Han, T. Bozorg-Grayeli, J. R. Groves, W. D. Nix, Scripta Mater. **63**, 1153 (2010).
[S12]J.-Y. Kim, D. Jang, J. R. Greer, Scripta Mater. **61**, 300 (2009).
[S13]S. Schneider, D. Kaufmann, B. G. Clark, P. A. Gruber, R. Mönig, O. Kraft, E Arzt, Phys. Review. Lett. **103**, 105501 (2009).
[S14]Q. Sun, Q. Guo, X. Yao, L. Xiao, J. R. Greer, J. Sun, Scripta Mater. **65**, 473 (2011).
[S15]E. Lilleodden, Scripta Mater. **62**, 532 (2010).
[S16]C. M. Byer, B. Li, B. Cao, K. T. Ramesh, Scripta Mater. **62**, 536 (2010).
[S17]T. Jennings, J. R. Greer, Phil. Mag. **91**, 1108 (2010).
[S18]T. Jennings, M. J. Burek, J. R. Greer, Phys. Rev. Lett. **104**, 135503 (2010).
[S19]S.-W. Lee, S. M. Han, W. D. Nix, Acta Mater. **57**, 4404 (2009).
[S20]J.-Y. Kim, J. R. Greer, Acta Mater. **57**, 5245 (2009).
[S21]G. Stan, S. Krylyuk, A. V. Davydov, I. Levin, R. F. Cook, Nano Lett. **12**, 2599 (2012).
[S22]H. Zhang, J. Tersoff, S. Xu, H. Chen, Q. Zhang, K. Zhang, Y. Yang, C.-S. Lee, K.-N. Tu, J. Li, Y. Lu, Science Advances **2**, e1501382 (2016).
[S23]Y. Zhu, F. Xu, Q. Q. Qin, W. Y. Fung, W. Lu, Nano Lett. **9**, 3934 (2009).
[S24]D. A. Smith, V. C. Holmberg, B. A. Korgel, ACS Nano **4**, 2356 (2010).
[S25]L. T. Ngo, D. Almécija, J. E. Sader, B. Daly, N. Petkov, J. D. Holmes, D. Erts, J. J. Boland, Nano Lett. **6**, 2964 (2006).
[S26]R. Agrawal, B. Peng, H. D. Espinosa, Nano Lett. **9**, 4177 (2009).

[S27]C. Q. Chen, J. Zhu, Appl. Phys. Lett. **90**, 043105 (2007).
[S28]H. S. Jang, S. H. Nahm, H. J. Lee, J. H. Kim, K. H. Oh, J. Korean Phys. Soc. **61**, 402 (2012).
[S29]B. Chen, J. Wang, Q. Gao, Y. Chen, X. Liao, C. Lu, H. H. Tan, Y.-W. Mai, J. Zou, S. P. Ringer, H. Gao, C. Jagadish, Nano Lett. **13**, 4369 (2013).
[S30]X. Li, X. L. Wei, T. T. Xu, Z. Y. Ning, J. P. Shu, X. Y. Wang, D. Pan, J. H. Zhao, T. Yang, Q. Chen, Appl. Phys. Lett. **104**, 103110 (2014).
[S31]S. Dai, J. Zhao, M. R. He, X. G. Wang, J. C. Wan, Z. W. Shan, J. Zhu, Nano Lett. **15**, 8 (2015).
[S32]Kaplan-Ashiri, S. R. Cohen, K. Gartsman, V. Ivanovskaya, T. Heine, G. Seifert, I. Wiesel, H. D. Wagner, R. Tenne, Proc. Natl. Acad. Sci. USA **103**, 523 (2006).
[S33]H. Guo, K. Chen, Y. Oh, K. Wang, C. Dejoie, S. A. S. Asif, O. L. Warren., Z. W. Shan, J. Wu, A. M. Minor, Nano Lett. **11**, 3207 (2011).
[S34]S. Wang, Y. He, H. Huang, J. Zou, J. G. Auchterlonie, L. Hou, B. Huang, Nanotechnology **24**, 285703 (2013).
[S35]S. Wang, Y. Wu, L. Lin, Y. He, H. Huang, Small **11**, 1672 (2015).
[S36]E. W. Wong, P. E. Sheehan, C. M. Lieber, Science **277**, 1971 (1997).
[S37]B. Wu, A. Heidelberg, J. J. Boland, Nat. Mater. **4**, 525 (2005).
[S38]Y. Lu, J. Song, J. Y. Huang, J. Lou, Adv. Funct. Mater. **21**, 3982 (2011).
[S39]Y. Yue, P. Liu, Z. Zhang, X. Han, E. Ma, Nano Lett. **11**, 3151 (2011).
[S40]D. Jang, X. Li, H. Gao, J. R. Greer, Nat. Nanotechnol. **7**, 594 (2012).
[S41]L. Wang, P. Liu, P. Guan, M. Yang, J. Sun, Y. Cheng, A. Hirata, Z. Zhang, E. Ma, M. Chen, X. Han, Nat. Commun. **4**, 2413 (2013).
[S42]S. J. Hao, L. S. Cui., F. M. Guo, Y. N. Liu, X. B. Shi, D. Q. Jiang, D. E. Brown, Y. Ren, Sci. Rep. **5**, 8892 (2015).
[S43]S. Narayanan, G. Cheng, Z. Zeng, Y. Zhu, T. Zhu, Nano Lett. 15, 4037 (2015).
[S44]D. Zhang, J.-M. Breguet, R. Clavel, L. Philippe, I. Utke, J. Michler, Nanotechnology **20**, 365706 (2009).

**Supplementary Note 3: Development of *in-situ* nanomechanical testing system**

An *in-situ* cryogenic nanomechanical testing system has been developed to investigate the effects of temperature on superelasticity in $CaKFe_4As_4$. Temperatures ranging from room temperature down to 40 K were reached using liquid He (LHe) and a customized Janis cryogenic cold finger system (Janis Research Company, MA, USA) combined with the *in-situ* micropillar compression system. The cold finger itself reaches ~4 K, the minimum temperature of LHe, but there is always cold loss due to heat transfer from the sample stage and radiation from the chamber wall. In order to mitigate this and reach a minimum temperature of 40K, multiple iterations of the stage design and connections needed to be done. The overall cryogenic system design is similar to that of the alumina and titanium stage.[S45-S47] Note that the cooling capability of the sample stage is strongly dependent of the sample stage material. In this work, we developed a high-density polyethylene (HDPE) stage due to its thermal conductivity (~0.49 $Wm^{-1}K^{-1}$) being much lower than alumina (~30 $Wm^{-1}K^{-1}$) and titanium (~20 $Wm^{-1}K^{-1}$). In previous works, we confirmed that it takes more than 10 hours to achieve 130 K with alumina and titanium stages. With our new HDPE sample stage, however, we were able to achieve 40 K only within one hour because HDPE provided the least amount of thermal conduction for the system (Figure S9). Thus, the HDPE sample stage has a great cooling performance and is stiff enough for reliable mechanical testing.

Micropillar compression testing was performed at 40 K, 100 K, 150 K and room temperature. During the cryogenic test, we carefully managed the thermal drift by equilibrating the tip temperature with the sample temperature. This approach is the same with the technique suggested by the literatures of high temperature nanoindentation and compression testing of shape-memory alloys and ceramics.[S48,S49] It was demonstrated that the temperature equilibration

of the tip through mechanical contact could be used up to 500 $^{o}$C for the high temperature nanoindentation. For cryogenic testing, the maximum possible temperature difference from room temperature is only 300 K and is about 260 K (= 300 K – 40 K) in this study. Thus, it is expected that the tip contact cooling would work better in the case of cryogenic test. For our testing purposes, the flat punch tip holds contact with the cooled sample surface for at least, if not more than, 30 minutes to equilibrate the tip and sample temperatures. By monitoring the change in displacement under a constant load condition, we were able to confirm that the temperature profile reaches steady state. Then, the tip is immediately translated to a micropillar, and the compression test is conducted quickly. In using this method, post testing data shows that the most thermal drift measured is always below 1 nm/s, which is small enough to assume no significant change in temperature during mechanical testing.

**Reference of Supplementary Note 3**


[S45]S.-W. Lee, L. Meza, J. R. Greer. App. Phy. Lett. **103**, 101906 (2013).
[S46]S.-W. Lee, Y. Cheng, I. Ryu, J. R. Greer, Science China Technological Sciences **16**, 184 (2014).
[S47]S.-W. Lee, J.-Z. Mehdi, D. Chen, Y.-W. Zhang, J. R. Greer, Nano Lett. **15**, 5673 (2015).
[S48]C. A. Schuh, J. K. Mason, A. C. Lund, Nature Mater. **4**, 617 (2005).
[S49]J. C. Trenkle, C. E. Packard, C. A. Schuh, Rev. Sci. Instrum. **81**, 073901 (2010).

## APPENDIX IV: Response to comments from advisory boards

1. How much can FIB sample preparation affect the TEM sample (dislocation structure)?

FIB process can certainly affect the dislocation structure but it appears to be minor. There were four different deformation cases; the non-deformed, 5 % deformed, over 20 % deformed, cryogenic temperature testing and their TEM samples were made by the exactly same process. They exhibited clear difference. In other words, even though the damage to the sample caused by FIB process exists, it is not significant enough to change the dislocation structure.

2. Is DBTT of Nb size-dependent?

The DBTT of Nb at bulk scale is 148 K. Since the experiments were done only at 56 K, 100 K, and 298 K due to the time and resources, we were not able to pinpoint the DBTT at small scale. Largely, the size effect can be defined by whether there is a change in properties between bulk and small. The problem is, however, to decide the line, which size is the boundary. Aside from the problem, the result of the experiment appears that DBTT can change as the size is decreased. At bulk scale, the driving factor of DBT is the dislocation mobility whereas, at small scale, the driving factor of DBT is the dislocation cross-slip probability. The mobility changes drastically as the temperature drops but the samples at small scale can recover the mobility since they can have higher stress without failing first. Thus, at low temperature at small scale, the cross-slip probability decides whether the material can multiply its dislocations effectively or not, and consequently, whether the material will go through ductile or brittle fracture. However, once the material is at the small scale regime, meaning that the free surface is highly available, for example, from 10 μm to 1 μm, the DBTT is not expected to change much.

3. Why does the stress drop while the sample is under tensile loading and what kind of information can be extracted?

When the material is being deformed faster than the loading speed, the machine will decrease the force in order to slow down. It is the feedback loop response of the machine`s load-controlled system to maintain the loading speed. In the Nb case, when the dislocation sources operate easily and stably and the applied stress can activate the operation, the material can deform faster than the loading speed. It results into the strain burst, which appears to be a stress drop in the stress-strain curve. When there is a strain burst, the extent of the rapidly increased strain can exhibit useful information. The uni-axial strain (%) can be converted to the uni-axial displacement (nm) by multiplying strain by the gauge length. After that, the uni-axial displacement along the loading direction can be converted to the shear displacement along the dislocation slip direction by dividing it by the cosine value of the two directions. Then, the shear displacement can be divided by the burgers vector, which refers how much the material will displace once a dislocation sweeps it through. The number (the shear displacement divided by the burgers vector) means how many dislocations sweep through, or how many times the anchored single arm source operates in the given plane. In DBT of Nb study, this number is large at cryogenic temperatures and small at room temperature. In other words, the source operation is stable at cryogenic temperatures due to lack of cross-slip events, whereas it is hindered at room temperature.

4. Can dislocations be nucleated from the surface, instead of dislocation multiplication? If dislocations are nucleated from the free surface and it becomes difficult at low

temperature, can this be the explanation of DBT at low temperature, not the change of cross-slip probability?

The stress required to nucleate a dislocation is much higher than that of multiplication from the pre-existing sources. The free surface can work as heterogeneous dislocation nucleation site and the stress will be lower than that of homogenous dislocation nucleation. However, in the MD simulations, the stress that enabled dislocation self-multiplication via surface cross-slip cannot nucleate a new dislocation from the free surface.

5. What is surface cross-slip?

Cross-slip is that a dislocation changes the plane where it is gliding. Inside the material, cross-slip is thermally activated by the thermal vibration. However, surface cross-slip is athermal process. It is the result of the system to minimize the length of the dislocation. In other words, the surface cross-slip can occur at 0 K because minimization of the energy is the driving force, not thermal vibration. (a dislocation with a length of l will increase the energy of the system by $0.5\ Gb^2l$. Thermodynamically, minimizing the length of the dislocation line is favored.)

6. Regarding DBT and DBTT, will bonding affect them?

DBT is controlled by how dislocations can move or multiply. In case of metals, dislocations can move relatively freely. Thus, the change in ductility (DBT) is more gradual. However, for covalent bonding materials, (e.g. Si), the DBT can be more discrete since dislocations cannot move freely until at a specific temperature point. The curve will be more step-like, compared to those of metals.

7. What exactly do you mean by transition ‘onset’ and ‘offset’? How can they be defined?

The ‘onset’ refers to the beginning of the structural collapse via As-As bonding, whereas the ‘offset’ refers to the completion of the structural collapse. In uni-axial experiments, when the stress-strain curve begins to deviate from its linearity, it is considered as the ‘onset’ point. Once the material completes the structural collapse, the stress-strain curve begins to show linearity again. That is considered as the ‘offset’ point. $CaFe_2As_2$ undergoes structural collapse to ‘collapsed tetragonal’ from it ambient structure by making As-As bonds around Ca ions.

8. Define ‘first hcT transition’. What is the difference between a half-collapsed and collapsed structure?

$CaKFe_4As_4$ undergoes two steps of structural collapses sequentially via making As-As bonds around Ca ions first, and around K ions second. Therefore, the first collapse is only half of the entire possible structural collapse and the transition is from the ambient structure (tetragonal) to half-collapsed-tetragonal, hcT.

In the structure, all the As-As pairs can participate in bond making and breaking under loading and unloading of significant pressure. However, in $CaKFe_4As_4$, As-As bonds form first around Ca ions. The second structural collapse will require much high pressure but can occur eventually. Therefore, it is no longer ‘half-collapsed’ once all the As-As pairs form bonds.

9. Regarding Si-Si-type bonds in $ThCr_2Si_2$-type, why would forming and breaking Si-Si type bonds lead to a decrease in stiffness? More importantly, how does forming and

breaking kick in? Does Si-Si bond form at the transition? Or, is there some kind of continual process?

It is hypothesized that the gradual propagation of phase transition because the volume fraction of two phases changes gradually (so, the initial phase disappears gradually and the new phase forms gradually). This kind of situation often occurs in solidification (e.g. eutectic solidification of Al-Si) when the total Gibbs free energy of two phase mixture is lower than that of single phase. In this case, the abrupt change (the first order transition) occurs locally, but the macroscopic change looks smooth. After full compression, its magnetic state completely changes from paramagnetic to nonmagnetic.